12-2012

Growth and Characterization of Hexagonal Lu-Fe-O Multiferroic Thin Films

Wenbin Wang
wwang23@utk.edu

To the Graduate Council:

I am submitting herewith a dissertation written by Wenbin Wang entitled "Growth and Characterization of Hexagonal Lu-Fe-O Multiferroic Thin Films." I have examined the final electronic copy of this dissertation for form and content and recommend that it be accepted in partial fulfillment of the requirements for the degree of Doctor of Philosophy, with a major in Physics.

Pengcheng Dai, Major Professor

We have read this dissertation and recommend its acceptance:

David Mandrus, Jian Shen, Hanno Weitering

Accepted for the Council:
Carolyn R. Hodges

Vice Provost and Dean of the Graduate School

(Original signatures are on file with official student records.)

Growth and Characterization of Hexagonal Lu-Fe-O Multiferroic Thin Films

A Dissertation Presented for the

Doctor of Philosophy

Degree

The University of Tennessee, Knoxville

Wenbin Wang

December 2012

DEDICATION

To my grandparents, parents, and husband

ACKNOWLEDGEMENT

First, I must give my high, respectful gratitude to my supervisor, Prof Jian Shen, for his guidance and support throughout the years. His passions for research and great insight have been a great inspiration to me.

I would like to thank my committee: Pengcheng Dai, David Mandrus and Hanno Weitering for their continuous support and review of my work.

I have been incredibly fortunate to work with the most brilliant scientists in the Thin Films and Nanostructures group at Oak Ridge National Lab. I would like to express my sincere thanks to Xiaoshan Xu for his thought guidance and encouragement during my research. His unwavering dedication to research has been inspirational. I am also very grateful to all the stuff members in our group, Zac Ward, Paul Snijders, Hans M. Christen and Ho Nyung Lee for their guidance and support. I also have to thank Hangwen Guo, Zsolt Marton and Dali Sun for their help throughout my project. Work with them made my doctoral research become an enjoyable experience.

My project was a collaborative effort and I could not have done it without the help from all my collaborators. I send my thanks to all my collaborators Zheng Gai, Xuemei Chen, Miaofang Chi, Wei Tian and David J. Keavney for all their help.

I would like to express my deeply gratitude to all my friends (too many to list here but you know who you are!) at Knoxville for providing support and friendship that I needed. I like to thank Jack and Lorelei for all unconditional love, support to me and gave me the feeling of home in a foreign country. I also thank my best girlfriends Clarina, Lin, Nancy and Mengshu for being there for when I need you the most.

I would like to express my eternal appreciation towards my family who have always been there for me no matter where I am. All the support and love they have provided me over the years was the greatest gift anyone has ever given me.

The best outcome during my Ph.D life is meeting my soul mate and husband. Thank him for encouraging me when I lost confidence; thank him for always being my side even when I was irritable and depressed; thank him for giving me energy and unconditional love in every minute of my life. There are no words to express how much I love him.

ABSTRACT

In the quest for new types of information processing and storage, complex oxides stand out as one of the most promising material classes. The multiple functionalities of complex oxides naturally arise from the delicate energy balance between the various forms of order (structural, electronic, magnetic). In particular, multiferroic and magnetoelectric oxides which simultaneously exhibit more than one type of ferroic orders have many advantages over existing materials. Widespread practical applications will require a single-phase multiferroic material with a transition temperature that lies considerably above room temperature, large electric and magnetic polarizations, and strong coupling between ferroic orders.

Recently, multiferroic $LuFe_2O_4$ has attracted great interest because it has relatively high transition temperatures, large polarization, high magnetic coercivity, and the strong magnetoelectric coupling. Compared to the large amount of effort to study bulk $LuFe_2O_4$, there are only a couple of reported attempts to grow $LuFe_2O_4$ thin films, presumably due to difficulties in the sample preparation. In this thesis, a comprehensive growth diagram of Lu-Fe-O compounds on MgO (111) substrates using pulsed laser deposition is constructed based on extensive growth experiments. The $LuFe_2O_4$ phase can only be grown in a small range of temperature and O_2 pressure conditions. An understanding of the growth mechanism of Lu-Fe-O compound films is offered in terms of the thermochemistry at the surface. Superparamagnetism is observed in the $LuFe_2O_4$ film and is explained in terms of the effect of the impurity hexagonal $LuFeO_3$ (h-$LuFeO_3$) phase and structural defects.

In addition to $LuFe_2O_4$, we also succeeded in growing hexagonal-$LuFeO_3$ (h-$LuFeO_3$) epitaxial films in single crystalline form on either insulating or metallic substrates using pulsed laser deposition (PLD). H-$LuFeO_3$ thin films exhibit hysteresis in piezoresponse force microscopy

(PFM) measurements indicative of ferroelectricity, and simultaneously show antiferromagnetic order, with both properties coexisting at room temperature.

TABLE OF CONTENTS

LIST OF TABLES

LIST OF FIGURES

Chapter 1:
Introduction and Background

1.1 Introduction of multiferroics

In recent years, Multiferroics have attracted great interest in the condensed matter physics community due to their scientific and technological importance. Multiferroics are materials that exhibit more than one ferroic orders simultaneously, such as ferroelectricity, ferromagnetism (antiferromagnetism) and ferroelasticity, and also exhibit coupling between these ferroic order parameters (Fig. 1.1). In particular, magnetoelectric multiferroics have ferroelectricity and ferromagnetism (antiferromagnetism) in the same phase and coupling between each other. In these materials, polarization or spin orientations can be switched by applying a magnetic field or an electric field which leads to potential applications for multifunction device. For example, a multiple state memory can store data in both the electric and magnetic polarizations; and data can be written electrically and read magnetically in a novel memory media. This will resolve the energy dissipation problems associated with FRAMS (ferromagnetic random access memory) and FeRAMs(ferroelectric random access memory). Instead of applying a current to generate the field for writing, applying an electric field to write the data can avoid the dissipation effects; also, instead of discharging and recharging the capacitor during the read to reset the memory back to the initial value, applying an electric field and reading the data magnetically will also save energy.

1.2 History of multiferroics

In the nineteenth century, James Clerk Maxwell proposed four famous equations governing the dynamic of the electric field, magnetic field and electric charge. In these equations, the accelerated electric charge can produce magnetic field and the changed magnetic field can induce a voltage. However, electric and magnetic ordering in solids are often treated separately, because the former arises from the charges of electrons or ions while the latter are associated with the spins of unpaired electrons. Around 1950s, Pierre Curie suggested the presence of materials that can be electrically polarized by magnetic field and magnetized by electric field.[1] And later Landau and Lifshitz pointed out [2] that piezomagnetism, which consists of linear coupling between a magnetic field in a solid and a deformation (analogous to piezoelectricity) ,and magnetoelectricity, which consists of linear coupling between magnetic and electric field could exist in solid state system.

These effects were first discovered by Dzyaloshinsky theoretically and Astrov experimentally. They confirmed the existence of the electric field induced magnetization and magnetic field induced polarization in the Cr_2O_3. This discovery generated tremendous interest in 1970s.[3] However, these materials have small magnitude of the induced polarization and magnetization, low magnetic ordering temperature and relatively weak magnetoelectrical (ME) coupling, which are mainly because the single phase materials with both properties could not be widely produced. More than 20 years later, major progresses were obtained both theoretically and experimentally in this field. The new technique which can produce high-quality single crystal samples provides new types of multiferroics with new mechanisms for ferroic orders. In addition, more theoretical studies using the first-principles computation techniques give a comprehensive understanding of

this ME effect. The advances in oxide thin film growth techniques also provide a way to tune the structure and properties of materials through strain.

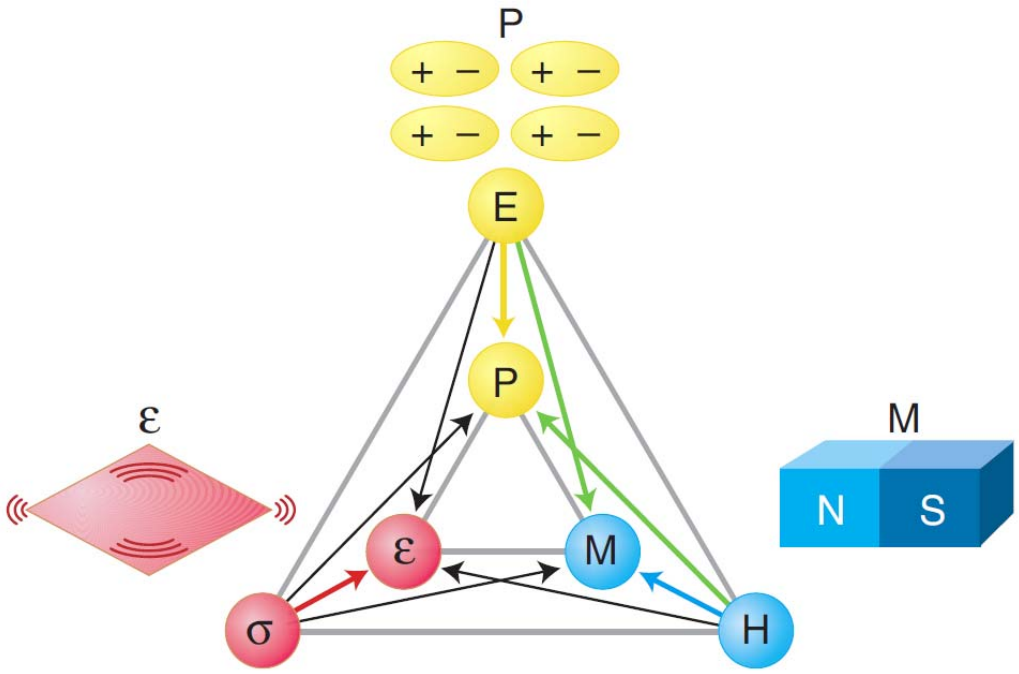

Figure 1.1 P, M, ε are spontaneously formed to produce ferromagnetism, ferroelectricity and ferroeleasticity, respectively. In multiferroics, the coexistence of at least two ferroic forms of ordering leads to additional interactions. In a magnetoelectric multiferroic, a magnetic field may control P or an electric field may control M (green arrows).[4]

1.3 Magnetoelectric coupling

The magnetoelectric effect can be explained by the expansion of the free energy of a material:[5,6]

$$F(\vec{E},\vec{H}) = F_0 + P_i^w E_i - M_i^s H_i - \frac{1}{2}\varepsilon_0\varepsilon_{ij}E_iE_j - \frac{1}{2}\mu_0\mu_{ij}H_iH_j - \alpha_{ij}E_iH_j$$
$$-\frac{1}{2}\beta_{ijk}E_iH_jH_k - \frac{1}{2}\gamma_{ijk}H_iE_jE_k - \cdots \qquad (1)$$

where E and H as the electric field and magnetic field; ε and μ are the electric and magnetic susceptibilities; the tensor α is a tensor describing linear magnetoelectric coupling; β and γ

represent higher-order magnetoelectric coefficients. Here the magnetoelectric effects can be established as the differentiation of the free energy:

$$P_i = -\frac{\partial F}{\partial E_i} = P_i^s + \varepsilon_0 \varepsilon_{ij} E_j + \alpha_{ij} H_j + \frac{1}{2}\beta_{ijk} H_j H_k + \cdots \qquad (2)$$

$$M_i = -\frac{\partial F}{\partial H_i} = M_i^s + \mu_0 \mu_{ij} H_j + \alpha_{ij} E_j + \frac{1}{2}\gamma_{ijk} E_j E_k + \cdots \qquad (3)$$

where P_i and M_i are the spontaneous polarization and magnetization, respectively. If we only focus on the linear ME effect, the tensor α_{ij} is a critical factor. By forcing the sum of the first three high order terms to be larger than zero, and ignoring the higher order coupling terms in equation (1), we can get the equation

$$\alpha^2_{ij} \le \varepsilon_0 \mu_0 \varepsilon_{ii} \mu_{jj} \quad (4)$$

which shows the α_{ij} is bounded by the tensors of electric and magnetic susceptibilities. It is evident that multiferroics can achieve strong ME effects because ferromagnetic and ferroelectric materials often possess a large ε_{ii} and μ_{jj} respectively.

1.4 The classification of multiferroic compounds

Multiferroic materials are rare in nature because ferromagnetic (antiferromagnetic) or ferroelectric orders are associated with different degree of freedom of electron and lattice. In ferromagnetic (antiferromagnetic) materials, magnetic order arises from the exchange interactions of partially filled d or f shells of transition metal or rare earth compounds. When the magnetic order develops, time-reversal symmetry is spontaneously broken. This means the

magnetic moment changes the sign under the symmetry operation M(-t)=-M(t) whereas the polarization remains invariant P(-t)=P(t). However, in the conventional ferroelectricitic materials, the positively charged transition metal ions will loss the d orbital electrons and form the covalent bond with the neighboring negative ions, As a result, the space-inversion symmetry is spontaneously broken P(-x)=-P(x) whereas the magnetization remains invariant M(-x)=M(x) as shown in Fig. 1.2. The collective shift of cations and anions inside the periodic crystal will induce a spontaneous electric polarization. In this respect, one needs partially filled d orbital and the other one needs the empty d orbital; and the two mechanisms are mutually exclusive. In practice, the microscopic origin of magnetism is basically the same in all magnets. In order to achieve the coexistence of ferroelectricity and magnetism in single phase, it is important to search for alternative mechanism for ferroelectricity. Here we classify the multiferroic compounds by different origins of ferroelectricity. The first type of multiferroic materials (such as BiFeO3) always show large spontaneous polarization P (10-100 $\mu C/cm^2$) and high transition temperature. However, because the ferroelectricity and ferromagnetism have different origins and are formed by different subsystems (different ions), the coupling between different orders is very weak. For the type II materials (such as $LuFe_2O_4$), the ferroelectricity and magnetic order still have different origins, but are formed by the same subsystem, so these materials show stronger couplings between ferroic orders. In the type III multiferroics (such as $TbMnO_3$), ferroelectricity is caused by the ferromagnetism (antiferromagnetism) and therefore, the coupling between ferroic orders are very strong. However, the transition temperatures are always very low and the polarizations are very small (10-2 μC/cm2) in these materials. As shown in the Table 1.2, from type I materials to type III materials (left to right), both the transition temperatures and the polarizations decrease while the couplings increase.

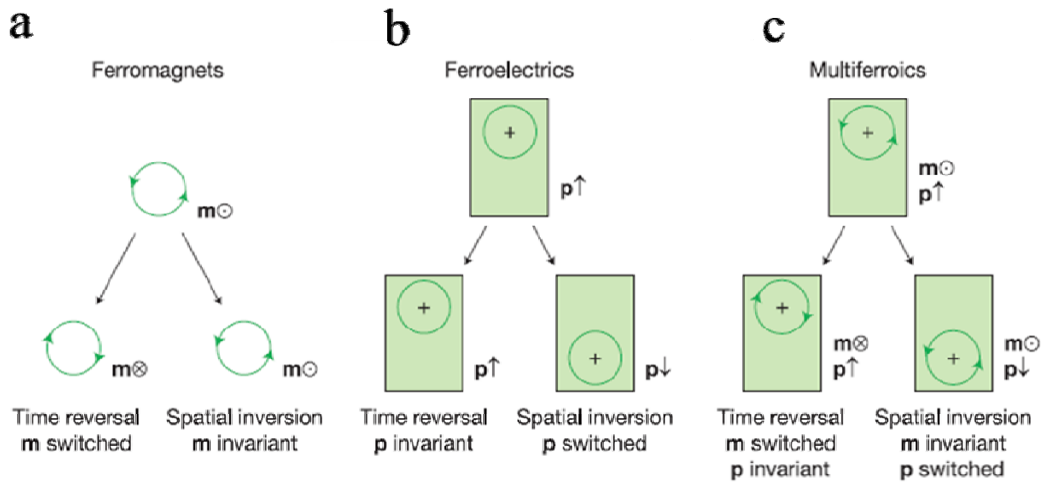

Figure 1.2 Time-reversal and spatial-inversion symmetry in multiferroics. (a) Ferromagnets (antiferromagnets). The local magnetic moment m can be seen as a current carrying loop with i=dq/dt, a spatial inversion produces no change, but time reversal switches the direction of the current and thus m. (b) Ferroelectrics. The local dipole moment p will be reversed by spatial inversion, no net time dependence. (c) Multiferroics break both ferromagnetic and ferroelectric symmetry.[7]

Table 1.2 Categories of multiferroics

E, M in different subsystem	**E, M in the same subsystem, different origin**	**E caused by M**
Lone pair FE $BiFeO_3$ T_C=1100 K, T_N=640 K, 100 μC/cm²	Charge (valence) order of magnetic ions $LuFe_2O_4$ T_C=320 K, T_N=240 K 25 μC/cm²	Spiral Magnets $TbMnO_3$ T_C=30 K, T_N=40 K, 6e-2 μC/cm²
Geometric FE $YMnO_3$ T_C=900 K, T_N=80 K, 5 μC/cm²		Frustrated collinear M Ca3CoMnO6 T_C,T_N=15 K 9e-2 μC/cm²

T_{order}↘, polarization ↘, coupling ↗

1.4.1 Type I multiferroics

In this group, ferroelectricity and ferromagnetism (antiferromagnetism) have different origins and from different subsystem. As mentioned above, this kind of multiferroics has high transition temperatures for both ferroic orders, but the coupling between magnetism and ferroelectricity is usually rather week. We classify this group of multiferroics by the mechanism of ferroelectricity.

I. Ferrelectricity due to lone pair.

There are hundreds of the perovskites with magnetic order or ferroelectric order. However, there is almost no overlap between the two classes of materials. In the case of ferroelectric materials, ferroelectricity arises from the 'empty d shell'. When d electrons move from the transition ions to the neighboring oxygen, the transition metal ions will shift from the center of the octahedral, which causes the ferroelectricity. As for magnetism, one needs partially filled d shell of the transition metal. One way to achieve the magnetic order in these materials is to put both magnetic ion and the empty d shell transition metal ions together but on different sites, such as $BiFeO_3$, $BiMnO_3$ and $PbVO_3$. $BiFeO_3$ has been widely studied in recent years because of the high transition temperature (T_{Fe}=1100K, T_M=643K) and large polarization 100μC/cm^2. The formally trivalent Bi contains a lone pair of 6s electrons in $BiFeO_3$ (the valence electron configuration of Bi is $6s^26p^3$). Such $6s^2$ lone pairs are often very active from a structural viewpoint. The lone pairs will move away from the centrosymmetric position with its oxygen surrounding and create local dipoles, resulting in a distorted monoclinic structure as shown in Fig. 1.3. In terms of magnetism, $BiFeO_3$ displays a G-type antiferromagnetic ordering of Fe^{3+} ions below T = 643 K.

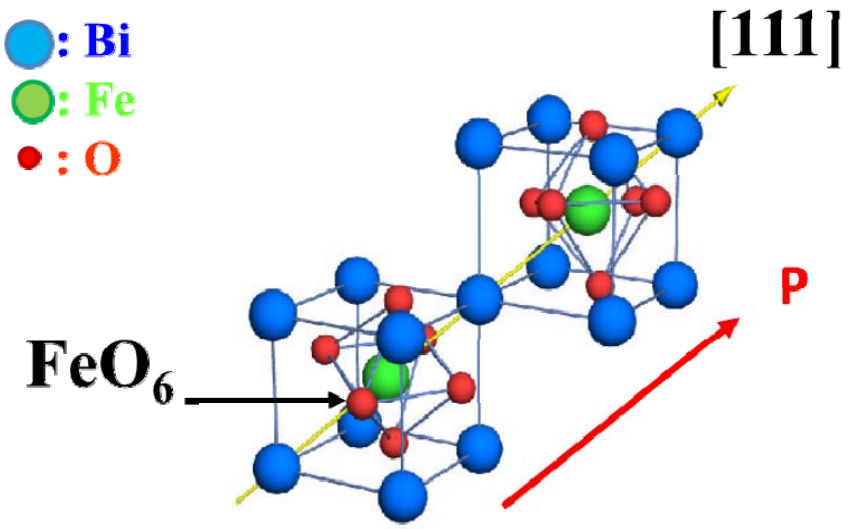

Figure 1.3 Ferroelectricity (T_C=1100 K) from displacement of Bi^{3+} from the centrosymmetric position in its oxygen surrounding. The structure changed from a cubic to a distorted monoclinic.

II. Ferroelectricity due to geometric distortion

Haxagonal-$RMnO_3$ is one of the most intensively studied materials to integrate into heterostructures for their high polarization, high ferroelectric transition temperature (900-1000K). The ferroelectricity in this class of compound originates from the coordinated movement of atoms at the rare earth site and a simultaneous rotation of the MnO_5 trigonal-bipyramids. In the h-RMnO3 system, the formation of the ferroelectricity from the high temperature phase to low temperature phase can be decomposed into two steps[8]. As shown in the Fig. 1.4, the tilting of the MnO_5 bipyramids and corrugating of the R layers generating two inequivalent sites of R atoms: 1/3 of R atoms are above the other 2/3 of them, corresponding to a $\sqrt{3}\times\sqrt{3}$ reconstruction in the a-b plane. High temperature (HT) symmetry $P6_3/mmc$ changes to the low temperature (LT) symmetry $P6_3cm$. Then the O_{ap}-Mn-O_{ap} axis in MnO5 bipyramid moves along z axis and generates a spontaneous polarization. Besides the high transition temperature and strong

polarization, it was also discovered that the magneto-elastic coupling is strong in the h-$RMnO_3$. [9] Since the ferroelectricity in h-$RMnO_3$ is induced by the distortion of the atoms, the giant magneto-elastic coupling will produce the desired coupling between the ferroelectric moment and the antiferromagnetic moment. However, the magnetic ordering temperature (<100 K) of $RMnO_3$ is relatively low. Interestingly, the magnetic ordering temperature in isostructural h-$RFeO_3$ is expected to be muchhigher than that of $RMnO_3$ due to the much stronger exchange interaction between Fe^{3+} ions. Recently, h-$RFeO_3$ phase was successfully stabilized as thin film (on what substrate).[10] The polar structure of the h-$RFeO_3$ films suggests that ferroelectricity may also exist in this system.

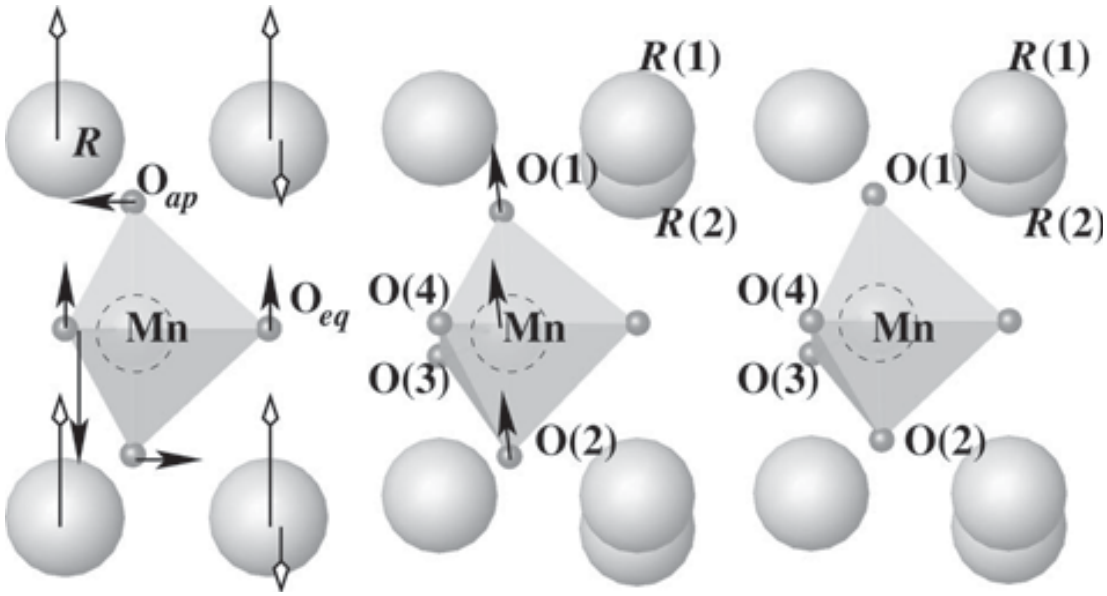

Figure 1.4 Haxagonal manganites order in two steps. (a) Tilting of the MnO_5 trigonal-bipyramids and corrugates of the R layer. (b) O_{ap}-Mn-O_{ap} axis is displaced (c) Spontaneous electric polarization is generated. [8]

1.4.2 Type II multiferroics : Ferroelectricity due to charge ordering

In this class of multiferroics, the ferroelectricity is driven by the charge ordering in the magnetic materials, and both ferroelectricity (charge ordering) and magnetic orders originate from the same subsystem (same ion sites). Before discussing the details of charge ordering multiferroic materials, let's use a simple one dimensional chain model to explain the essential mechanism of the appearance of ferroelectricity by charge ordering.[11] Inferroelectric materials, the space inversion symmetry is spontaneously broken below the ferroelectric transition temperature. Imaging there is a one dimensional chain, all the atoms on this chain are equally charged on each site, and the distances between atoms are the same. So the system is uniform and keeps spatial inversion symmetry. Then, instead of have the same charge, one atom is charged with +e and the neighboring two atoms are charged with –e; we call it site-centered charge ordering. The chain still has the spatial inversion symmetry and there is no net dipole moment in the system. If all atoms still have the same charge on each site, but with different distances between atoms, we call it bond-centered charge ordering with centrosymmetry. As shown in the Fig. 1.5, when we combine both site-centered and bond-centered charge ordering in one system, clearly, the space inversion symmetry is broken and system becomes ferroelectric.

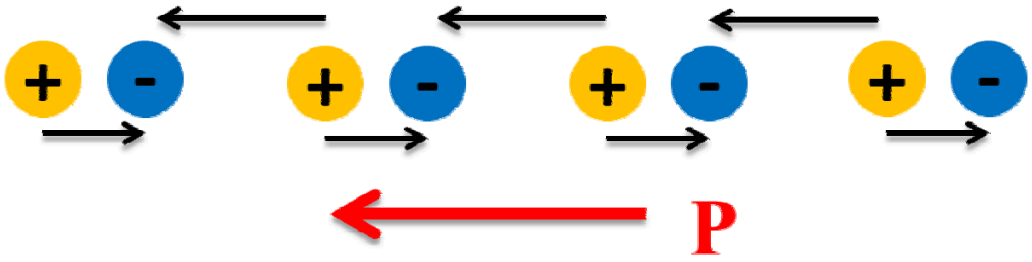

Figure 1.5 One dimensional charge arrays. The combination of site-centered and bond-centered charge ordering break the spatial inversion symmetry and induce ferroelectricity.

In the case of 3D materials, such as $LuFe_2O_4$, the situation is more complicated. $LuFe_2O_4$ contains double layers of Fe_2O_2 with a triangular lattice that are sandwiched by LuO_2 layers. An equal amount of Fe^{2+} and Fe^{3+} coexist at the same site of the hexagonal lattice. Because of the average Fe valence is 2.5+, the Fe^{2+} and Fe^{3+} ions can be regarded as an excess and a deficiency of half an electron, respectively. At high temperature, Fe^{2+} and Fe^{3+} are randomly distributed in the triangular lattice. With decreasing temperature, the interaction between Fe ions prefers Fe^{2+} and Fe^{3+} as nearest neighbors in the triangular lattice in order to minimize the coulomb energy, which is similar to the case of spin frustration. As shown in the Fig. 1.6, in each bilayer, the lower layer has 2:1 ratio of Fe^{2+} and Fe^{3+} and the upper layer has the inverse 1:2 ratio. The double layer displays net polarization from the upper layer to the lower layer. The coexistence of the geometric frustration and the stacking of the triangular nets leading to forming a 3D charge ordering state at T_{CO}=320 K.[12] In the meanwhile, the strong magnetic interaction between Fe moments develop as a ferrimagnetic ordering with Neel temperature T_N=240K.

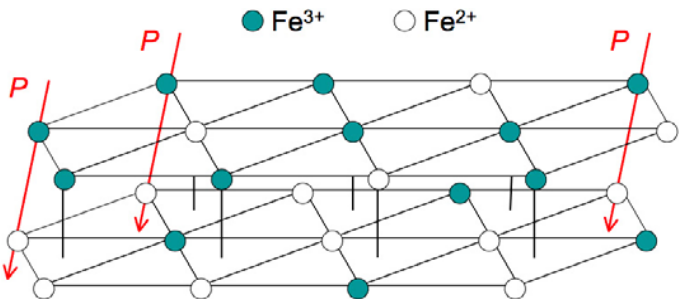

Figure 1.6 Double layer structure shows an upper layer to lower layer direction of net polarization.

Because both ferroic orders are from the same Fe ions in $LuFe_2O_4$, coupling between two ferroic orders is expected. In the Fig. 1.7, dielectric constant of $LuFe_2O_4$ is frequency dependent and it shows a large dielectric dispersion around the Neel temperature.[13] At low temperature, when the

fluctuation on the dipoles is frozen, the whole system lost the polarizability and the dielectric constant decreases. Interestingly, this decrease happens at the Neel temperature, indicating that the magnetic ordering is coupled with the electric ordering. In addition, significant changes of dielectric properties have been observed upon applying a small magnetic field at room temperature (inset). It was suggested that the charge fluctuations on the Fe sites were the main contributor to polarizability at high temperature. The Fe^{3+} is more strongly influenced by the magnetic field than Fe^{2+}, so the fluctuation in the system is weaker and the polarizability and dielectric constant will decrease under a magnetic field. The relatively high transition temperatures for the ferroic ordering and strong coupling of spins and electric dipoles at room temperature make $LuFe_2O_4$ a unique multiferroic material.

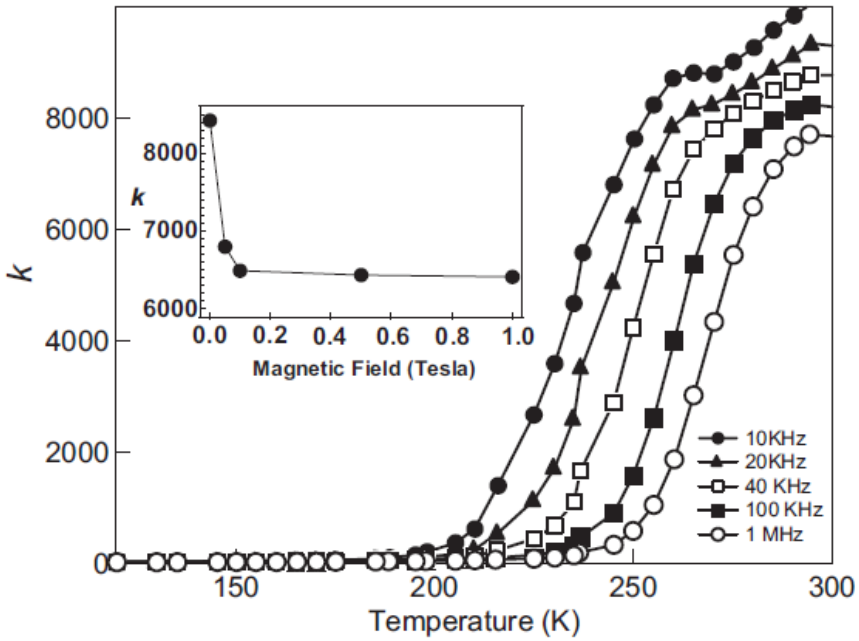

Figure 1.7 Dielectric constant (real part) versus temperature measured at various frequencies for $LuFe_2O_4$ under no magnetic field. The inset shows the variation of *k* with magnetic field at room temperature at 20 kHz.[14]

1.4.3 Type III multiferroics

In type III multiferroics, ferroelectricity occurs only in the magnetically ordered state. The ferroelectricity sets in at the same temperature as a certain type of magnetic ordering and is driven by it. Because the ferroelectricity is induced by the magnetic order, this type of materials always has strong coupling between the different ferroic orders. However, the transition temperature is always very low in this system.

I. Spiral magnets

In some of the materials such as Tb(Dy)MnO_3 and Tb(Dy)Mn_2O_5, the onset of ferroelectricity is correlated to the appearance of spiral magnetic ordering. This spiral magnetic ordering induced polarization can be understood microscopically by spin current model developed by Katsura[15] or by a phenomenological theory presented by Mostovoy[16]. They suggested that when the magnetic phase has sinusoidally modulated collinear magnetic order, the space inversion symmetry remains and the system doesn't have net electric moment. But the noncollinear incommensurate magnetic order breaks inversion symmetry and thus gives rise to electric polarization. This mechanism is theoretically shown as following function. The magnetic coupling has the form[16]

$$\phi_{em}(\vec{P},\vec{M}) = \gamma\vec{P}\cdot[\vec{M}(\nabla\cdot\vec{M}) - (\vec{M}\cdot\nabla)\vec{M}) + \cdots] \qquad (5)$$

If we only consider the "electric part" $\phi_e(\vec{P}) = -\frac{p^2}{2\chi_e}$, χ_e is the dielectric susceptibility

In absence of magnetism, then the variation of $\phi_e + \phi_{em}$ with respect to $\vec{P}$ can be written as

$$\vec{P} = \gamma\chi_e[(\vec{M}\cdot\nabla)\vec{M}) - \vec{M}(\nabla\cdot\vec{M})] \qquad (6)$$

Consider a spiral-spin-density-wave state with the wave vector $\vec{Q}$,

$$\vec{M} = M_1\vec{e}_1 \cos \vec{Q}\cdot\vec{x} + M_2\vec{e}_2 \sin \vec{Q}\cdot\vec{x} + M_3\vec{e}_3 \qquad (7)$$

So the average polarization is

$$\overline{P} = \frac{1}{V}\int d^3x\vec{P} = \gamma\chi_e M_1 M_2[\vec{e}_3 \times \vec{Q}] \qquad (8)$$

From this equation, we can see that if only M1 or M2 is nonzero, equation (7) describes a sinusoidal wave and the average polarization is zero. If both M1 and M2 are nonzero, then this equation describes a helix with the spin rotation axis $\vec{e}_3$. The system shows spontaneous polarization. In the case of $TbMnO_3$ (T_N=41 K) the Mn^{3+} shows a collinear sinusoidal order and no electric order between 41K and 28K in the system. Below 28K, the sinusoidal order is replaced by a spiral order with $\vec{Q}$//b, Mn^{3+} rotate in the b-c plane with the rotation axis $\vec{e}_3$ //a, then, the system shows electric polarization with $\overline{P}$ //c (Fig. 1.8).

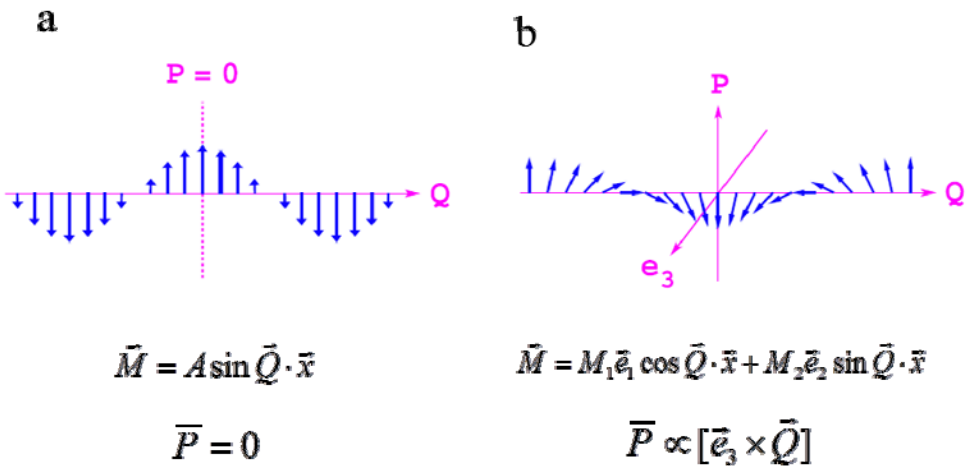

Figure 1.8 (a) The sinusoidal magnetic structure does not induce electric polarization. (b) Spiral magnetic structure inducing a net polarization.[16]

Since the ferroelectricity appears only in the spiral magnetic structure, it is not surprising the coupling between magnetic and ferroelectric order is especially strong. As shown in Fig. 1.9, $TbMnO_3$ shows a spin-flop transition under an external magnetic field.[17] The polarization vector rotates by 90 degree from c axis to a axis due to the flop of spin spiral from the a-b plane to the b-c plane. Because the intimately link between the polarization and the dielectric constant, the dielectric constant also changes significantly.

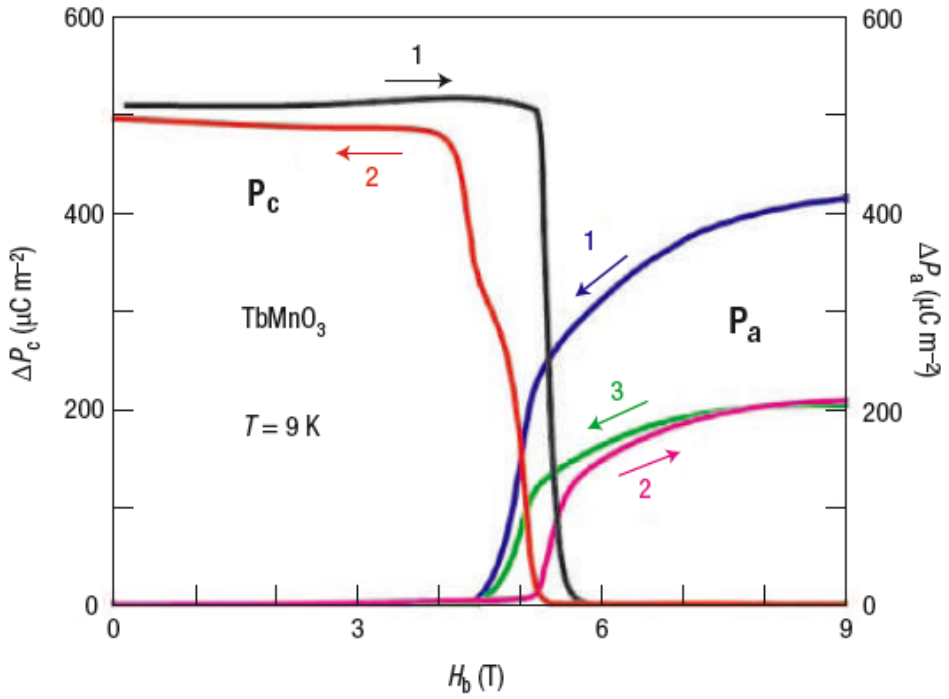

Figure 1.9 5T magnetic field changes the electric polarization direction in $TbMnO_3$ from the c axis to a axis.[17]

II. Frustrated collinear magnetic multiferroics

In addition to the spiral magnetic order, collinear frustrated magnetic order can also lead to ferroelectricity. In such a system, the magnetic moment aligns along one axis which can be

described using an Ising spin chain model. Polarization appears as a consequence of exchange striction because the magnetic order is coupled with the atomic positions. For example, in the case of Ca_3CoMnO_6,[18] Co^{2+} and Mn^{4+} ions alternating along the Ising chains exhibit an up-up-down-down (↑↑↓↓) magnetic order as shown in Fig. 1.10. Because the competition between the nearest-neighbor ferromagnetic and next-nearest-neighbor antiferromagnetic interaction, the superexchange shortens the bonds between the parallel, and stretches the antiparallel spin. Therefore, the magnetic order breaks the space-inversion symmetry and induces electric polarization via exchange striction.

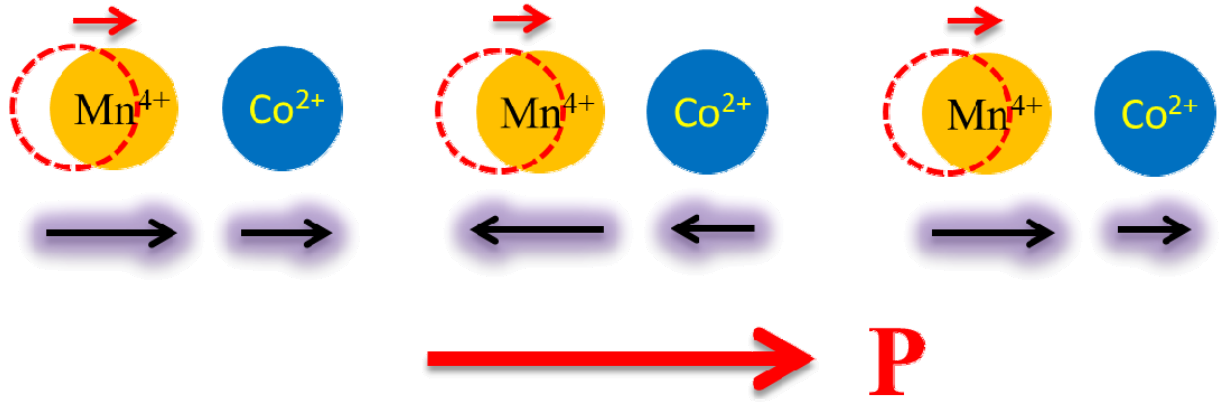

Figure 1.10 Ising chains with the up-up-down-down spin order and alternating ionic order. The possible magnetic configurations leading to the polarization is shown. The original atomic positions are shown with dashed circles.

1.5 From Bulk to thin film

Most multiferroic materials were studied as bulk form. In recent years, more attention was paid to the thin film form because thin films have lots of advantages. In the view of the practical

application, to obtain the materials in the form of thin film is necessary. At the same time, by using different substrates, one can tune the properties and phases of the materials; the doping process will be much easier in the thin film form than the bulk. Also, thin film growth techniques can provide routes to structures and phases that are inaccessible by traditional chemical methods. The most studied thin films are Bi-based perovskites and hexagonal manganites. By using different substrates and different substrates' surface orientations, one can get $BiFeO_3$ films of different symmetries. For example, monoclinic phase is stabilized on the (001) and (101) $SrTiO_3$ substrate, while the rhombohedra phase is crystallized on (111) $SrTiO_3$. [19,20] The ferroelectric transition temperature for bulk $BiFeO_3$ is 830C, which decreases to 650C under a strong epitaxial strain or 750C under a weak strain. Early bulk $BiFeO_3$ samples show a small polarization of 6.1$\mu C/cm^2$, which can reach 50-90$\mu C/cm^2$ in the thin film form.[21] The large polarization of the thin film is not only because of the epitaxial strain effects but also because of less defects in the thin films which can avoid the leakage effect. The magnetic properties of $BiFeO_3$ thin film can also be markedly different from bulk form. From the first principle calculation[22], it shows that spin canting is permitted in $BiFeO_3$ which can give a weak ferromagnetic moment. However, because the long wavelength period of the spiral spin structure in this material, as shown in Fig. 1.11, all the possible macroscopic magnetization are inhibited, Because this spiral spin structure can be suppressed through the strain in the thin film, a significant magnetization and a strong magnetoelectric coupling have been observed.[23]

In addition, thin films are also easy to change the properties through doping. If we substitute Tb at Bi sites in $BiFeO_3$, the sample displays good ferroelectric and magnetic properties and a coupling between them.[23]

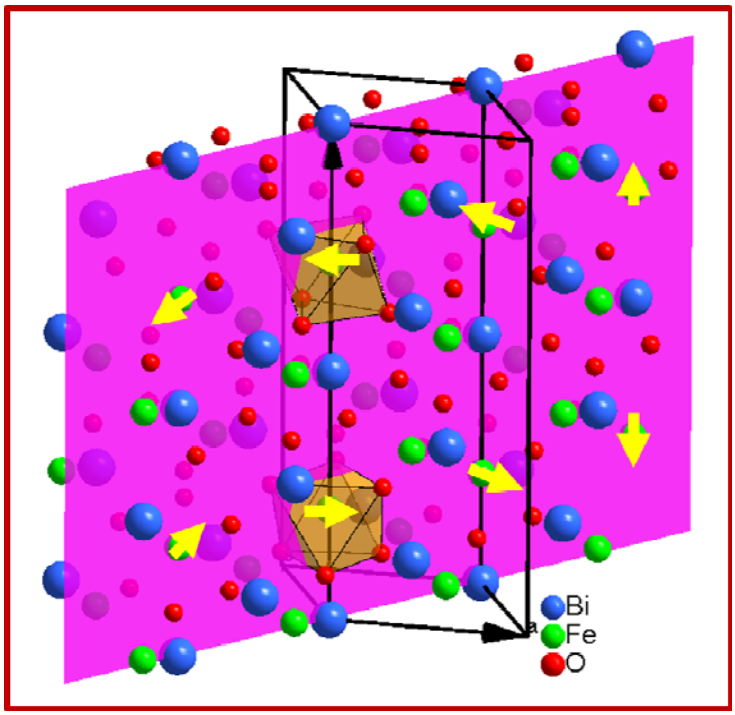

Figure 1.11 Magnetic structure of the $BiFeO_3$ with the spin spiral plane $(1\text{-}10)_{hex}$

The thin film technology can also provide routes to obtain structures that are inaccessible by traditional chemical methods. As introduced before, hexagonal structured $RMnO_3$ is one of the most intensively studied materials to integrate into heterostructures for their high polarization and high ferroelectric transition temperature. The low magnetic ordering temperature (<100 K) of $RMnO_3$ makes it hard to be used as multifunctional devices. Ferrites $RFeO_3$ normally crystallize as orthorhombic phase (o-$RFeO_3$), o-$RFeO_3$ is a non-polar antiferromagnet due to its central symmetric structure. Inspired by the h-$RMnO_3$, people realized that spin frustration on the hexagonal lattice will lead to a more interesting magnetic behavior in h-$RFeO_3$. Besides, replace Mn by Fe may increase the magnetic ordering temperature due to the much stronger bonding energy between Fe^{3+} ions. However, h-$RFeO_3$ is only stable at high temperature and metastable at room temperature. In previous work, few reports can be traced where h-RFeO3 were synthesized through quenching high temperature melt rapidly to get some h-$RFeO_3$ phase

nanoparticles as an impurity in o-$RFeO_3$ bulk.[24] Recently, it was discovered that room temperature h-$RFeO_3$ can be stabilized as thin film by using epitaxial strain. [10] This high quality single crystalline thin film is very important for the properties' study and potential application.

To summarize, the enhancement of magnetic and ferroelectric properties by changing the microscopic structure; easily doping different elements to tuning the physical properties; possibility of stabilizing new structure through the epitaxial strain; controlling the surface orientation by changing substrate's orientation make the thin film multiferroics represent new degrees of freedom for steering the ME properties toward an improved suitability for device applications. There is no doubt that in the forthcoming years, multiferroic thin films will be a topic of great interest, both in science and technology.

Chapter 2:

Growth Diagram and magnetic properties of $LuFe_2O_4$ thin films

2.1 Introduction and motivation

Multiferroics like $BiFeO_3$ where the magnetic and electric orders originate from different parts of the structure have high ordering temperatures but weak coupling between different orders.[25] Other materials, like $TbMn_2O_5$, exhibiting ferroelectricity due to the broken symmetry caused by the spiral magnetic moment have strong magnetoelectric coupling.[26] However, here the ordering temperature is very low and the electric polarization is small. $LuFe_2O_4$ contains layers of Fe_2O_2 with a triangular lattice that are sandwiched by LuO_2 layers. Combined with the mixed valance of Fe, the Fe_2O_2 layers with triangular lattice form a charge ordered state at T_{CO}=320 K, followed by a ferrimagnetic order at T_N=240 K.[27] Significant changes in dielectric properties have been observed upon application of a small magnetic field at room temperature.[14] The relatively high transition temperature, large polarization, high magnetic coercivity and the strong magneto-electric coupling make $LuFe_2O_4$ a unique multiferroic material. Recently, the possibility of fast switching and high tunability of $LuFe_2O_4$ due to the electronic origin of its charge order was demonstrated.[28] Compared to the large amount of effort to study bulk $LuFe_2O_4$, little work has been reported on $LuFe_2O_4$ at low dimensions, presumably due to difficulties in the sample preparation. Here we study the growth of $LuFe_2O_4$ thin films on MgO(111) substrate using pulsed laser deposition (PLD). We have constructed a growth diagram based on our results. The parameter space for growing epitaxial $LuFe_2O_4$ thin films turns out to be a narrow window of temperature and oxygen pressure, which creates significant experimental difficulties. While the

observed Neel temperature of the film is very close to the bulk value, the hysteresis is surprisingly weaker, resulting in superparamagnetism in the films. The demonstration of epitaxial growth of $LuFe_2O_4$ thin films and the distinct magnetic properties open up new possibilities for studying multiferroicity of low dimensional $LuFe_2O_4$, tuning of its properties, and eventual functionalization.

Compared to the large amount of effort to study bulk $LuFe_2O_4$, there are only a couple of reported attempts to grow $LuFe_2O_4$ thin films on α-Al_2O_3 (0001) and on Si substrates using pulsed laser deposition (PLD).[29,30] Liu et al found that the growth of $LuFe_2O_4$ on α-Al_2O_3 (0001) needs substrate temperatures as high as 850 °C.[29] In addition, significant deviation of the Lu:Fe stoichiometry from 1:2 was observed which was attributed to different ablation efficiencies of Lu and Fe in the target. This problem was circumvented by enriching the Fe concentration of the target material. However, as a result, Fe_3O_4 and Fe_2O_3 impurities were introduced as intermediate layers between the $LuFe_2O_4$ film and the α-Al_2O_3 substrate.

In this thesis, I did a comprehensive study on the growth of Lu-Fe-O compound thin films on MgO(111) substrate using pulsed laser deposition (PLD). The experimentally constructed growth diagram shows that the parameter space for growing epitaxial $LuFe_2O_4$ thin films turns out to be a narrow window of temperature and oxygen pressure, which creates significant experimental difficulty. Based on these results we have gained fundamental understanding of the growth of Lu-Fe-O compound films: the growth temperature needs to be high enough to stabilize the metastable phase $LuFe_2O_4$. On the other hand the loss of Fe at high temperature also changes the resulting phase from $LuFe_2O_4$. These two effects cause the narrow window of the growth condition. Typical $LuFe_2O_4$ films exhibit superparamagnetism, which is consistent with the fact that the $LuFe_2O_4$ in the film are epitaxially sandwiched by the impurity phase hexagonal-$LuFeO_3$

(h-$LuFeO_3$). The demonstration of epitaxial growth of $LuFe_2O_4$ thin films and the distinct magnetic properties open up new possibilities for studying multiferroicity of low dimensional $LuFe_2O_4$, tuning of its properties, and eventual functionalization.

This chapter is organized as the following: Section 2.2 describes the experimental conditions; In section 2.3, the growth mechanism learned from the experiments is explained; Section 2.4 shows the detailed structure analysis of the grown phases; Section 2.5 discusses the magnetic properties of typical $LuFe_2O_4$ thin films with epitaxial inclusion of impurity h-$LuFeO_3$ phase.

2.2 Experimental details

Lu-Fe-O compound thin films were grown using PLD with a KrF (λ=248 nm) laser. In principle, all the parameters will have to be scanned and optimized in order to realize the growth of high quality $LuFe_2O_4$ thin films. We are more focused on elucidating the mechanism of the growth. Therefore, fine scan of the substrate temperature and the oxygen pressure were carried out to map out the growth diagram involving the growth of more than one hundred samples, while all the other parameters were kept constant. The laser density is 2.5 J cm^{-2} with a repetition rate of 1 Hz. The thickness of the films is about 100 nm. The substrate is MgO(111) single crystal annealed in O_2 for 24 hours at 1100 °C. The target material used is polycrystalline $LuFe_2O_4$, whose properties are verified using powder x-ray diffraction (XRD) and a superconducting quantum interference device (SQUID). After growth, the sample heating is turned off so that the sample cools down to room temperature within 5 minutes. The substrates were clamped on a Pt heating plate with temperatures measured by a pyrometer using emissivity of 0.3. The growth was monitored using reflection high energy electron diffraction (RHEED) for the entire process

from heating up the substrates to cooling down after growth. Transmission Electron Microscopy (TEM) work was carried out on a Cs-corrected FEI Titan 80/300-kV TEM/STEM. TEM specimen was prepared with traditional mechanical polishing followed by ion milling. High resolution Z-contrast images were acquired using 300KV and a beam size of 0.7Å. The magnetic properties were measured using SQUID. The subtraction of background is done by assuming that the magnetization saturates in large field at 300 K. In principle, all the parameters described above will have to be scanned and optimized in order to realize the growth of high quality $LuFe_2O_4$ thin films. In this thesis, we are more focused on elucidating the mechanism of the growth. Therefore, fine scans of the substrate temperature and the O_2 pressure were carried out to map out the growth diagram involving the growth of more than one hundred samples, while all the other parameters were kept constant.

2.3 Growth diagram, structural characterizations and magnetism

In this thesis, we start from the ternary phase diagram of the bulk Lu-Fe-O system, a section of which is shown in Fig. 2.1(a) at 1200 °C.[31,32] This system belongs to the D-type of lanthanoid-Fe-O compounds for which there are four stable three-element phases: $LuFe_2O_4$ (A) and $Lu_2Fe_3O_7$ (B), $LuFeO_3$ (perovskite or P), $Lu_3Fe_5O_{12}$ (garnet or G).[33] In principle, one way to form a single $LuFe_2O_4$ phase is to keep atomic ratio Lu:Fe=1:2 and vary the oxygen pressure, shown as a thick dashed line in Fig. 2.1(a).

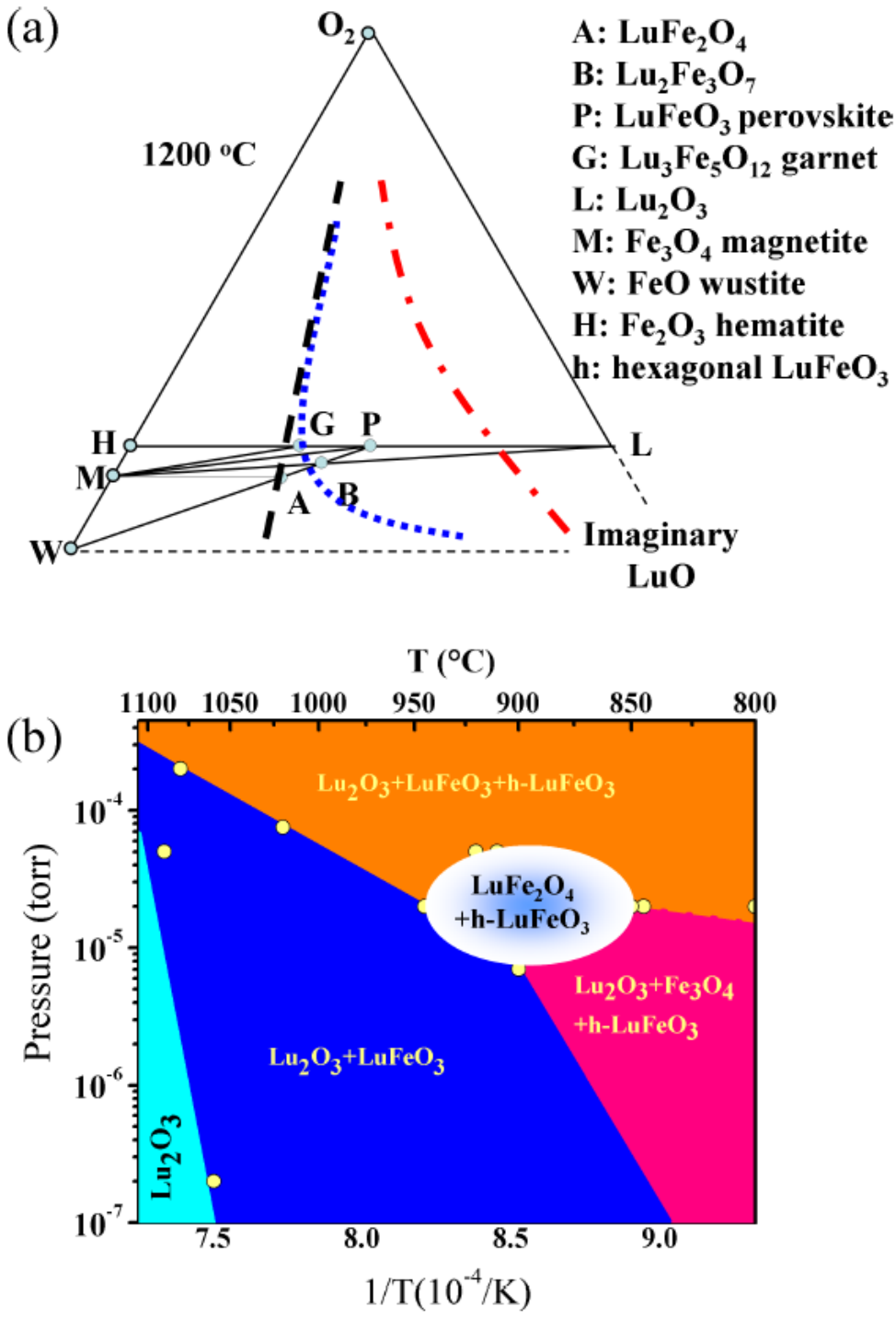

Figure 2.1 (a) The phase diagram of the bulk Lu-Fe-O ternary system at 1200 °C. (b) The experimental growth diagram of the Lu-Fe-O thin films on MgO(111) substrates.

Figure 2.2(a) presents the X-ray diffraction (XRD) data of films grown at 1050 °C in various O_2 pressures. The $LuFe_2O_4$ phase is not observed. In addition, the Lu:Fe stoichiometry of the films is very different from that of the target. The dominant phase is always Lu_2O_3 (L). The concentration of $LuFeO_3$ rises with O_2 pressure. At high enough O_2 pressure, hexagonal (h)-$LuFeO_3$ compound starts to appear.[34]

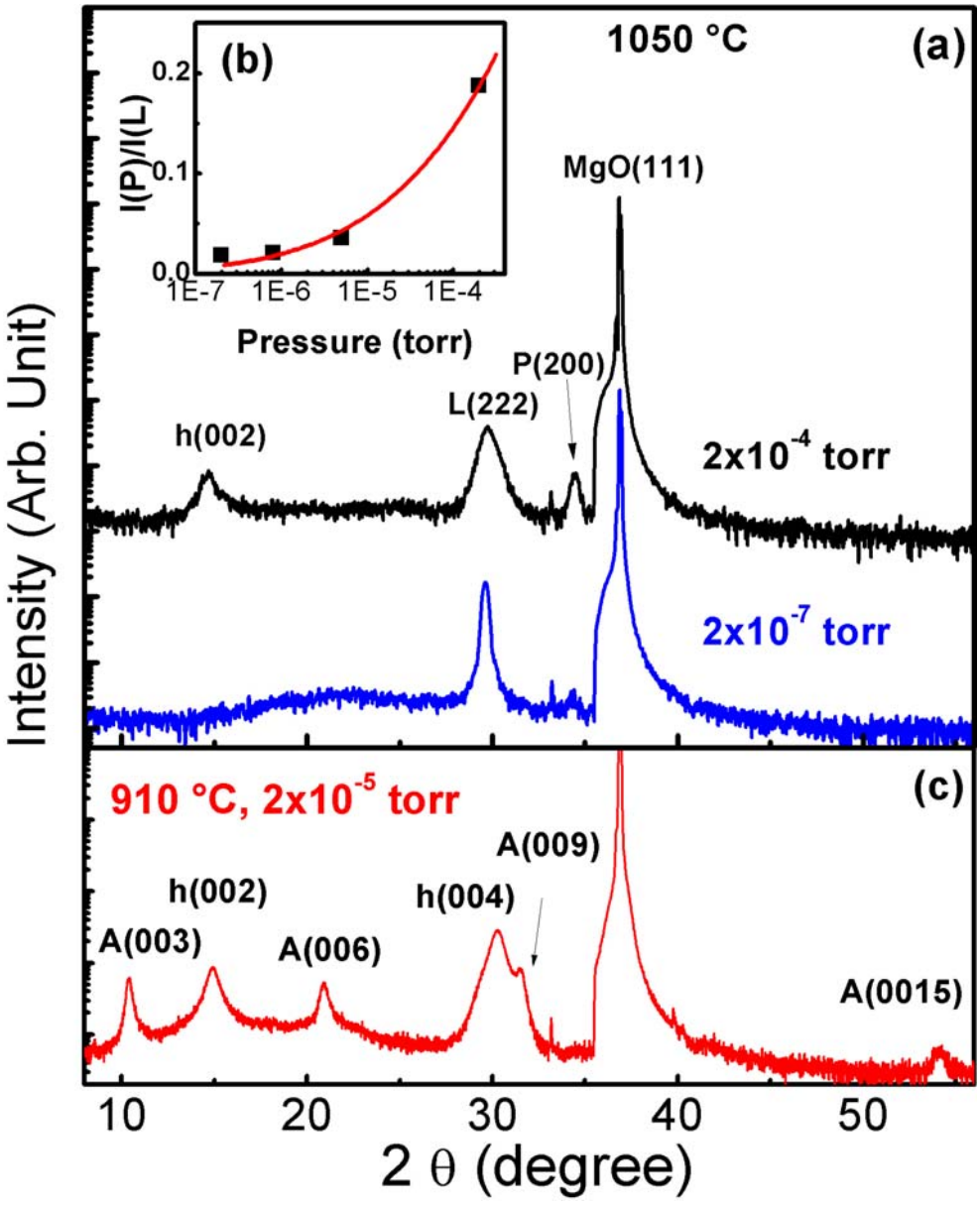

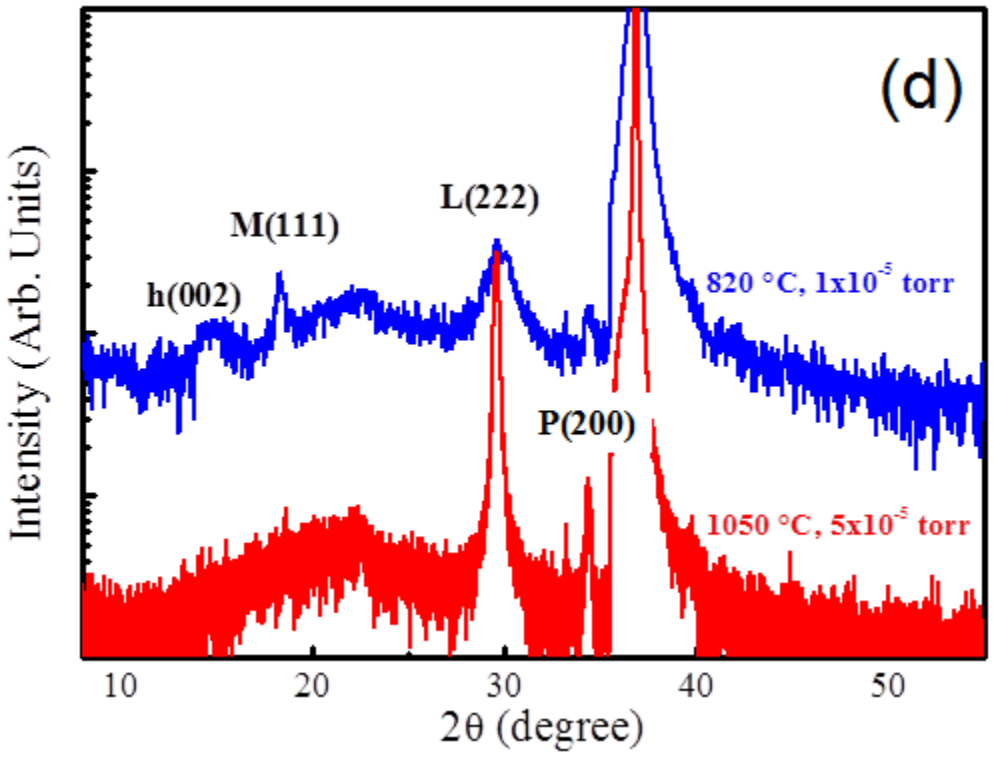

Figure 2.2. XRD data of the films grown at (a) T=1050 °C and at two different O_2 pressures, (region 1 and 3). (b) The ratio between the intensity of the P phase ($LuFeO_3$) I(P) and L phase (Lu_2O_3) I(L) as a function of the temperature. The line is a fit with the thermochemistry model (see text). (c) Typical XRD data of a $LuFe_2O_4$ film that shows the $LuFe_2O_4$ c-axis to be perpendicular to the substrate surface as expected. Also present is a significant amount of h-$LuFeO_3$ (region 4). (d) XRD data of region 2 and 5. The lower curve corresponds to the growth region 2. The upper curve corresponds to the growth region 5

To elucidate the mechanism of the growth of Lu-Fe-O coumpound films, we carried out fine scan of the substrate temperature and the oxygen pressure to map out the growth diagram. Figure 2.1(b) is the resulting experimental growth diagram. The important observations can be summarized as follows. (1) In the low temperature region the growth follows more or less the behavior predicted by the bulk phase diagram Fig. 2.1(a): at high pressure, the existing phases are $LuFeO_3$, Lu_2O_3 and h-$LuFeO_3$; when the pressure is decreased, the Fe_3O_4 phase starts to appear. This is consistent with the fact that $LuFe_2O_4$ and $Lu_2Fe_3O_7$ phases are not stable at low

temperature.[34] (2) In the high temperature region, the growth deviates strongly from the thick dashed line in the bulk phase diagram Fig. 2.1(a) in that the Lu:Fe stoichiometry differs dramatically from that of the polycrystalline $LuFe_2O_4$ target. As shown in Fig. 2.2 (a), the $LuFe_2O_4$ phase is not observed in the films grown at 1050 ℃. The dominant phase is always Lu_2O_3 (L).[35] The concentration of $LuFeO_3$ rises with increasing O_2 pressure. At high enough O_2 pressure, h-$LuFeO_3$ compounds start to form.[34] The formation of Lu-Fe-O compounds in the films qualitatively follows the dash-dotted line in Fig. 2.1(a). (3) Only in the small range of pressure and temperature indicated by the elliptical area in Fig. 2.1(b) is the growth of $LuFe_2O_4$ the most effective. In this case, the growth follows qualitatively the dotted line in Fig. 2.1(a). Typical XRD data are displayed in Fig. 2.2(c) showing both $LuFe_2O_4$ and h-$LuFeO_3$, indicating deviation of Lu:Fe stoichiometry from that of the target even in this narrow window. [36]

From the experiment growth phase diagram, it shows 5 growth regions:

1. Lu_2O_3 (cyan);
2. Lu_2O_3+$LuFeO_3$ (blue)
3. Lu_2O_3+$LuFeO_3$+h-$LuFeO_3$ (orange)
4. $LuFe_2O_4$+h-$LuFeO_3$ (white)
5. Lu_2O_3+Fe_3O_4+h-$LuFeO_3$ (pink)

The representative XRD of the following regions are given in Fig. 2.2: Fig. 2.2(a) lower curve corresponds to the region 1). Fig. 2.2(a) upper curve corresponds to the region 3). Fig. 2.2(c) corresponds to the region 4). The representative XRD of the region 2) and 5) is given in Fig. 2d. Note that, at low temperature, the crystallization of the films is poor.

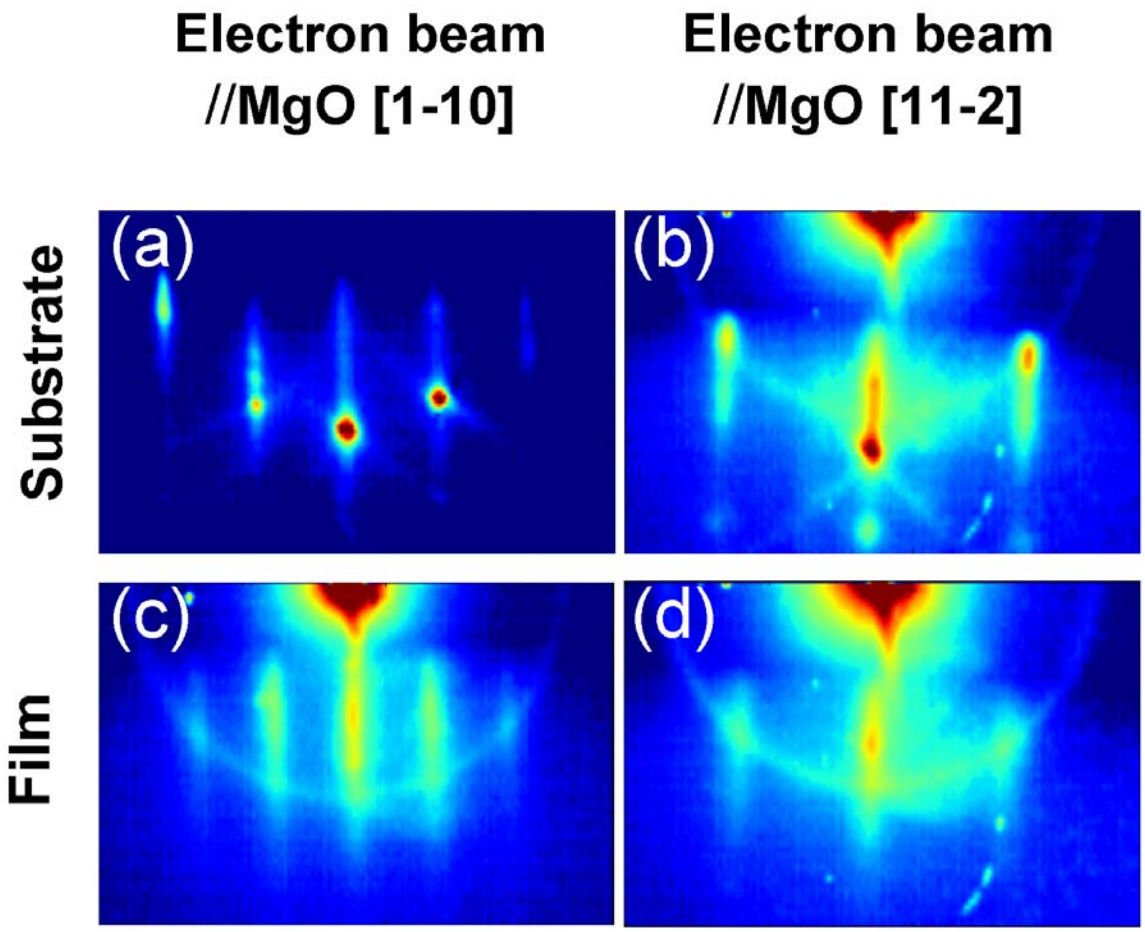

Figure 2.3. RHEED data corresponding to the pattern of the MgO(111) substrate taken with the electron beam along [1-10] (a) and [11-2] (b) directions, respectively, and to the pattern of $LuFe_2O_4$ film taken with the electron beam along MgO[1-10] (c) and MgO[11-2] (d) directions. All panels have the same scale.

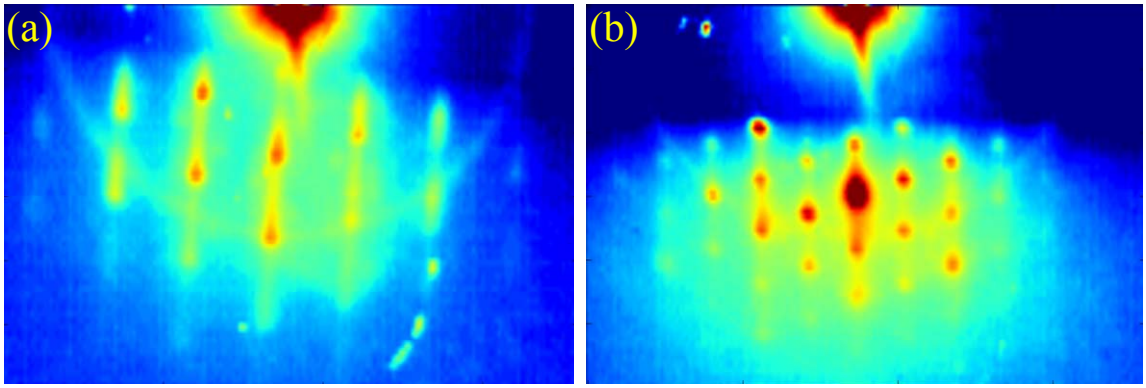

Figure 2.4. RHEED images corresponding to the patterns of the Lu_2O_3 (a), Fe_3O_4 (b) islands taken with the electron beam along MgO[1-10] direction. All panels have the same scale.

Table 2.1. Morphology and epitaxial relation of compound grown on MgO (111) substrates.

Compound	Morphology	Epitaxial relation
$LuFe_2O_4$	Quasi 2D	[001]//MgO[111], [100]//MgO[1-10]
Lu_2O_3	Quasi 3D	[111]//MgO[111], [1-10]//MgO[1-10]
$LuFeO_3$	3D	[100]//MgO[111], [001]//MgO[1-10]
Fe_3O_4	3D	[111]//MgO[111], [1-10]//MgO[1-10]
h-$LuFeO_3$	Quasi 2D	[001]//MgO[111], [1-10]//MgO[1-10]

The combination of in-situ structure characterization using RHEED and ex-situ characterization by XRD allows assignment of the epitaxial relation between the existing phases and the substrates. The results are given in Table 2.1. The XRD data in Fig. 2.2 indicate that all the grown compounds have one unique plane parallel to the substrate surface, which simplifies the analysis. From the RHEED pattern, one can measure the two dimensional (2D) lattice constant for the grown film. If three dimensional (3D) island growths occur, the RHEED pattern corresponds to the diffraction pattern of the transmitted electron beam which contains more structural information. Figure 2.3 shows the RHEED patterns of the MgO (111) substrates and the $LuFe_2O_4$ film with the direction of the electron beam along MgO [1-10] and MgO [11-2], respectively. The strong $LuFe_2O_4$ (003), (006) and (009) peaks observed in Fig. 2.2(b) indicate that the epitaxial relation is $LuFe_2O_4$ [001]//MgO[111], which is expected because both faces have 3-fold rotational symmetry. The streaky RHEED patterns in Fig. 2.3(c) and (d) suggests quasi-2D growth of $LuFe_2O_4$. The 2D lattice constant of the film can be calculated from the

separation of the streaks calibrated by the RHEED pattern of the MgO substrates. It is consistent with the $LuFe_2O_4$ lattice constant 3.44 Å within the experimental uncertainty of 2%. Hence, the in-plane epitaxial relation is $LuFe_2O_4$ [100]//MgO[1-10] (Fig. 2.5(a)). This is unexpected from the point of view of lattice matching, which predicts $LuFe_2O_4$ [100]//MgO[11-2] because a $\sqrt{3} \times \sqrt{3}$ supercell of $LuFe_2O_4$ with 30 degree rotation along the [001] direction has less than 0.1% mismatch with a 2×2 supercell of MgO (111) surface as shown in Fig. 2.5(b) . Contrasting with the apparent quasi-2D growth of $LuFe_2O_4$, Lu_2O_3 forms quasi-3D structures on the substrate as shown in Fig. 2.4(a). However, the RHEED pattern suggests a face centered cubic structure with a lattice constant half of that of bulk Lu_2O_3. The detailed structure is not clear at present. At low pressure and low temperature, the RHEED signal is dominated by the diffraction pattern of 3D Fe_3O_4 islands along the [11-2] direction (Fig. 2.4(b)), with the [111] direction perpendicular to the substrate surface. This is consistent with the XRD data. The lattice constant is the same as that of bulk Fe_3O_4 within the experimental uncertainty (of 2%).

To give a general idea about the lattice match relations between the thin films and the substrates, Table 2.2 lists the lattice constants of each compound. The structure parameters of the planes (the in-plane) that are observed to be parallel to the MgO(111) are also given.

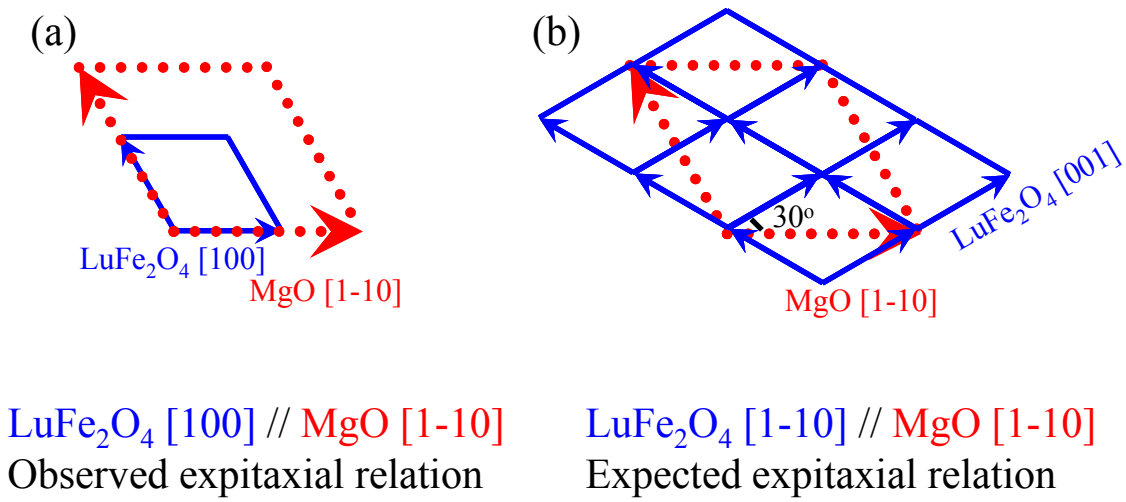

Figure 2.5. Epitaxial relation between $LuFe_2O_4$ films and MgO(111) substrates. (a) Observed expitaxial relation. (b) Expected epitaxial relation from geometry

Table 2.2. Structure parameters of each compound

Compound	**Space group**	**Lattice constants**	**In-plane lattice constants**
MgO	Fm-3m	a=b=c=4.211Å; α=β=γ=90° [37]	(111): a'=b'=5.955Å
$LuFe_2O_4$	R-3mH	a=b=3.441Å, c=25.28Å; α=β=90°, γ=120° [38]	(001): a'=b'=3.441Å
h-$LuFeO_3$	$P6_3cm$	a=b=5.965Å, c=11.702 Å; α=β=90°, γ=120° [39]	(001): a'=b'=5.965Å
$LuFeO_3$	Pbnm	a=5.213Å, b=5.547Å, c=7.565 Å; α=β=γ= 90° [40]	(100): a'=5.213Å, b'=5.547Å
Fe_3O_4	Fd-3m	a=b=c=8.396Å; α=β=γ= 90° [41]	(111): a'=b'=11.87Å
Lu_2O_3	Ia-3	a=b=c=10.355Å; α=β=γ= 90° [42]	(111): a'=b'=14.6Å

High resolution transmission electron microscopy (HRTEM) reveals the detailed structure of the $LuFe_2O_4$ films. As shown in Fig. 2.6(a), a layered structure of the film is obvious with some variation for different locations. The fast Fourier transforms (FFT) of the HRTEM image at different locations confirms the epitaxial relation observed from RHEED images: the FFT of the substrate (Fig. 2.6(d)) indicates the reciprocal lattice of MgO viewed from [11-2] direction. The FFT of the majority of the film (Fig. 2.6(c)) is consistent with the reciprocal lattice of $LuFe_2O_4$ viewed from the [1-10] direction while at some locations (Fig. 2.6(b)) suggests h-$LuFeO_3$ viewed from the [1-10] direction. These two phases $LuFe_2O_4$ and h-$LuFeO_3$ were further confirmed by direct observation using atomic-resolution Z-contrast imaging, which is shown in Fig. 2.6(e) and (f). The LuO_2-FeO-FeO-LuO_2 ordering in the $LuFe_2O_4$ phase and the LuO_2-FeO-LuO_2 ordering in the h-$LuFeO_3$ phase are clearly observed.

Although the intensity of the XRD peaks originating from the h-$LuFeO_3$ phase seems comparable to that of $LuFe_2O_4$ phase, the actual dominant phase is still $LuFe_2O_4$ due to the lower X-ray scattering cross section of the $LuFe_2O_4$ as compared with that of the h-$LuFeO_3$ phase. This is consistent with the low population of the h-$LuFeO_3$ phase in the HRTEM image. In addition, the RHEED patterns of h-$LuFeO_3$ and $LuFe_2O_4$ are supposed to be different according to their structures.[43] The fact that the observed RHEED patterns do not show any indication of h-$LuFeO_3$ within the detection limit also suggests a low concentration of the h-$LuFeO_3$ phase in the films.

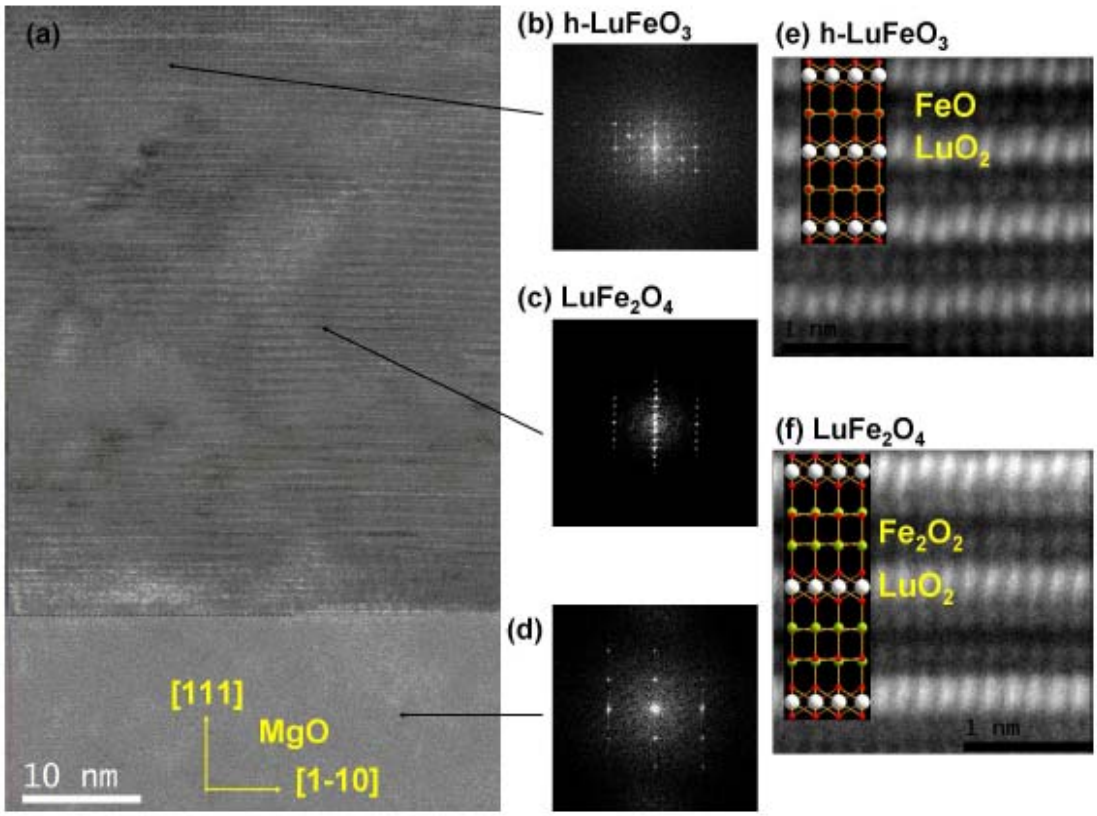

Figure 2.6. (a) Typical HRTEM image around the interface, where the interface is marked as a dashed line. (b-d) The Fourier transforms of various positions of (a), where (d) is from MgO substrate and (c) is from the majority of the film, and (b) is from the small top left part of the image. (e) and (f) are the atomic-resolution Z-contrast images corresponding to (b) and (c) respectively.

Ferrimagnetism, large magnetization and giant coercivity are of the key properties of $LuFe_2O_4$. This makes the study of the magnetic properties of $LuFe_2O_4$ films critical. As shown in Fig. 2.7(a), little hysteresis is observed for these $LuFe_2O_4$ films.[44] When magnetization is plotted against magnetic field over temperature (H/T), the data of 12, 50, 100 and 150 K fall on top of each other (Fig. 2.7(b)), which can be fitted by the Langevin function: $L(x)=\coth(x)-1/x$, where $x=\mu B/k_B T$, μ is the magnetic moment, B is the magnetic field, k_B is the Boltzmann constant and T is the temperature, indicating the superparamagnetic behaviour.[45,46] Figure 2.5 (d) shows an

example fit for 12 K data.

One can calculate the magnetic moment from the slope of the low field magnetization data with

$$\frac{dM}{dH} = \frac{N\mu^2}{3kT}\mu_0 \ , \quad (1)$$

where μ, N, μ_0 and k are the moment of the superparamagnetic domains, number of the domains per unit volume, the vacuum permeability and the Boltzmann constant, respectively.[47] The magnetic moments normalized to their maximum value as a function of temperature are plotted in Fig. 2.7(c), which follows the temperature dependence of the bulk saturation magnetization closely, suggesting that the Neel temperature of the films is not very different from the bulk value of 240 K.

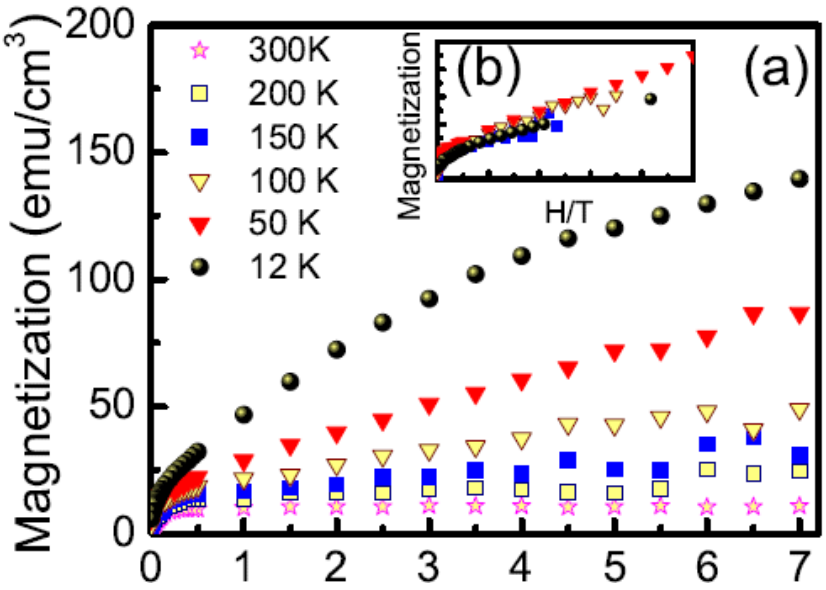

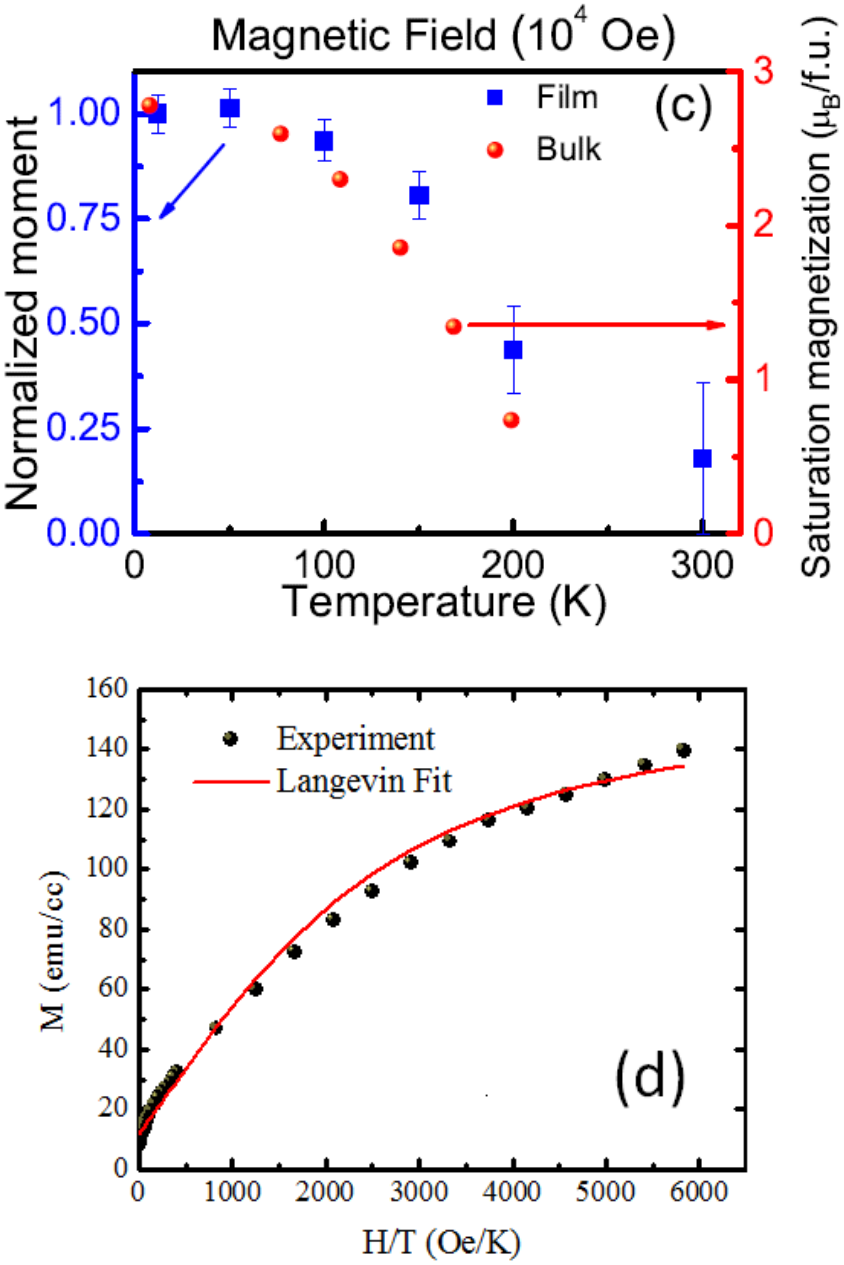

Figure 2.7. Magnetic properties of typical $LuFe_2O_4$ films. (a) The field dependence of the magnetization at various temperatures. (b) Magnetization plotted again magnetic field over temperature (*H/T*). (c) The temperature dependence of the magnetic moment of the superparamagnetic phase normalized to the maximum value and the bulk saturation magnetization from Reference [44]. The magnetic field is perpendicular to the plane of the film. (d) Magnetization data fitted with Langevin function at 12 K.

2.4 Discussion

The most surprising observation of the growth diagram is that the Lu-Fe-O compound formation at high temperature deviates strongly from the Lu:Fe stoichiometry of the target. Here we propose an explanation in terms of competition between nucleation and desorption of adatoms and its dependence on temperature and supersaturation. The residence time τ_{ad} of an adsorbed atom is given by:

$$\tau_{ad} = \frac{1}{\nu}\exp(\frac{E_{des}}{kT}) \ , \ (2)$$

where υ is the vibrational frequency and E_{des} is the desorption energy. Clearly, the residence time of an adatom is shorter at high temperature due to the higher desorption rate. The observed loss of Fe atoms suggests a smaller desorption energy (higher desorption rate) for Fe atoms. At low temperature, because $\exp(\frac{E_{des}}{kT})$ is large for both Lu and Fe adatoms, the Lu:Fe stoichiometry can be close to that of the target. The nucleation speed of deposited adatoms is:

$$J_{nuc} \propto (\frac{\Delta\mu^*}{T})^{-1/2}\exp(-\frac{\kappa}{\Delta\mu^* kT}), \quad (3)$$

where $\Delta\mu^*$ is the effective supersaturation (molar bulk Gibbs free energy change with surface energy consideration), while κ is proportional to the square of the edge energy of the nuclei per unit length.[48] Therefore, at the high temperature limit, the nucleation speed decreases with temperature and a high supersaturation favors a high nucleation speed. Consider the reaction

$$Fe + \frac{1}{2}Lu_2O_3 + \frac{3}{4}O_2 \rightarrow LuFeO_3 \ , \ (4)$$

which takes place under thermodynamic equilibrium during the annealing time in between the laser pulses, the supersaturation of oxygen is related to the O_2 pressure as:

$$\Delta\mu^*_{O(ad)} = \Delta\mu^*_0(T) + \frac{3}{4}RT\ln(P_{O_2}) \ , \ (5)$$

where N_A is the Avogadro constant. Eq. (5) suggests that higher O_2 pressure always corresponds to larger supersaturation, resulting in faster nucleation and better Lu:Fe stoichiometry. Combining Eqs. (5) and (3), one has the analytical relation between the nucleation speed and the O2 pressure:

$$J_{nuc} = [\frac{\Delta\mu^*_0(T) + \frac{3}{4}N_A kT\ln(P_{O_2})}{T}]^{1/2} * \exp[-\frac{\kappa}{\Delta\mu^*_0(T)kT + \frac{3}{4}N_A\ln(P_{O_2})(kT)^2}] \ , \ (6)$$

Figure 2.2 (b) inset shows XRD intensity (peak area) of the LuFeO3 phase relative to Lu_2O_3 (I(*P*)/I(*L*)) as a function of the O_2 pressure at 1050 °C. Assuming that the nucleation speed is proportional to the XRD intensity, one can fit experimental data with Eq. (6). The result shows $\Delta\mu^*(T)$=269 kJ mol^{-1}, similar to the bulk value found as $\Delta\mu_0=\Delta H^0-T\Delta S^0$=258.2 J/mol, taking the ΔH^0=-41.8 kJ mol^{-1} and ΔS^0=-121.4 J mol^{-1} K^{-1} and T=1050 °C.[31]

The chemical reactions related to the boundaries in the growth diagram and the corresponding standard entropy and enthalpy changes are listed in the Table 2.3.

Table 2.3 Standard enthalpy and entropy changes of the chemical reactions of Lu-Fe-O compounds

Reaction	$\Delta H^0(kJ/mol)$	$\Delta S^0(J/mol/K)$
$Fe+\frac{1}{2}Lu_2O_3+\frac{3}{4}O_2 \rightarrow LuFeO_3$	-41.8.8 [49]	-121.4 [49]
$2Fe+\frac{3}{2}O_2 \rightarrow Fe_2O_3$	-827.2 [50]	-274.7 [50]
$3Fe+2O_2 \rightarrow Fe_3O_4$	-1120.9 [50]	-322.2 [50]
$2Fe_3O_4+\frac{1}{2}O_2 \rightarrow 3Fe_2O_3$	-239.8 [50]	-179.7 [50]
$LuFe_2O_4+\frac{1}{4}O_2 \rightarrow LuFeO_3+\frac{1}{2}Fe_2O_3$	-179.6 [49]	-100.35 [49]
$5Fe+Lu_2O_3+LuFeO_3+3O_2 \rightarrow 3LuFe_2O_4$	-1538 [49]	-353.8 [49]

In the above analysis, the assumptions we made are: 1) the nucleation speed is proportional to the XRD intensity; 2) at high temperature the thermodynamic equilibrium gained during the annealing between the laser pulses determines the growth. These assumptions appear to be valid because the thermo-chemical parameters extracted from the model quantitatively agree with those from the literature. In other words, the growth of Lu-Fe-O at 1050 °C can be described using equilibrium thermodynamics, presumably due to the thermodynamic equilibration that occurs in between the laser pulses. Here the competition between the desorption and nucleation determines the Lu:Fe stoichiometry. When the temperature is high enough, the time scales of the nucleation and desorption are comparable. In this case, change of nucleation speed (due to the

change of supersaturation which is a function of O_2 pressure) affects the Lu:Fe stochiometry dramatically.

Based on this analysis, we expect the optimal growth conditions for $LuFe_2O_4$ films to be a narrow temperature and pressure window considering the necessary high temperature for the stability of $LuFe_2O_4$ phase that sets a lower limit, and the different desorption speed of Lu and Fe adatoms which sets an upper limit to the temperature. As we will describe below, this is indeed what has been observed in our experiments.

The observation of superparamagnetism in the $LuFe_2O_4$ films is unusual considering the bulk magnetic properties of $LuFe_2O_4$: an easy axis along the [001] direction with anisotropy energy as large as 100 K/spin and gigantic coercivity (9 T at 4 K). [44,51,52,53–55] These unique bulk properties were attributed to arise from the significant contribution of orbital magnetic moments (0.8 μ_B/f.u.) plus the collective freezing of magnetic domains with the size of approximately 100 nm in the Fe_2O_2 layer and 30 nm along the [001] direction.[47,44] The following scenario may explain the reduction of coercivity qualitatively: the structure of $LuFe_2O_4$ and h-$LuFeO_3$ both consist of layers of triangular lattices with a similar lattice constant. For $LuFe_2O_4$, the stacking is Fe_2O_2/LuO_2 while for h-$LuFeO_3$, FeO layers replace Fe_2O_2.[56,57] From XRD data, one can see the co-existence of both $LuFe_2O_4$ and h-$LuFeO_3$ phases. HRTEM indicates that the $LuFe_2O_4$ layers are divided into clusters by the h-$LuFeO_3$ layers and defects. According to a recent study, h-$LuFeO_3$ is weakly ferromagnetic, i.e. much less magnetic than $LuFe_2O_4$.[58] Therefore, when these clusters are much smaller than the magnetic domain dimensions in the bulk, one expects to see a reduction in coercivity. On the other hand, given the large anisotropy energy 100 K/spin, the observed hysteresis is too small even for clusters having a size as small as a few nanometers.

Further study on the microscopic magnetic structure is needed to understand the difference between the bulk and films.

2.5 Conclusion

In conclusion, we studied the growth dynamics of $LuFe_2O_4$ films on MgO (111) substrates and constructed the growth diagram. According to our understanding, application of the correct thermochemistry is the key to preferential formation of the $LuFe_2O_4$ phase: 1) at low temperature, $LuFe_2O$= is not a thermodynamically stable phase; 2) at high temperature, the Lu:Fe stoichiometry is off by so much due to the faster desorption of Fe adatoms that $LuFe_2O$= can not be formed; 3) in a narrow range of substrate temperature and O_2 pressure, $LuFe_2O_4$ dominates the grown phases with some h-$LuFeO_3$ phase epitaxially sandwiched in between due to the loss of Fe atoms. Superparamagnetism is observed in the film of $LuFe_2O_4$ containing h-$LuFeO_3$ impurities. The extracted Neel transition temperature is similar to that of bulk.

This work reveals the growth mechanism of Lu-Fe-O compound thin films, paving the way to the growth of high quality $LuFe_2O_4$ thin films and offers an approach to tuning their properties. This will be critical for future applications using $LuFe_2O_4$, a unique multiferroic material with large polarizations, high ordering temperatures, and strong magnetoelectric coupling.

Chapter 3:

Room-temperature coexistence of magnetic order and ferroelectricity in single crystal hexagonal $LuFeO_3$ films

3.1 Introduction and motivation

According to Khomskii, the multiferroics can be divided into two types: Type I (e.g. $BiFeO_3$ and $YMnO_3$) represents materials with robust ferroelectric and magnetic order. But the magnetoelectric coupling is relatively weak; Type II represents materials (e.g. $TbMnO_3$ and Ca_3CoMnO_6) whose ferroelectric order is caused by certain spacial-symmetry breaking magnetic ordering.[59] These materials normally have low ordering temperatures and small polarizations, although the magnetoelectric coupling is way higher than type I. Currently, $BiFeO_3$ and $RMnO_3$ (R=Ho, … Lu, Y or Sc) are the most intensive studied material to integrate into heterostructures for their high polarization and high transition temperature. [60] For the $BiFeO_3$, it known as the only one material which exhibit ferroelectricity and magnetic order above room temperature. Moreover, integrating the advantages offered by these materials into existing technologies will require them to be interfaced with other materials without compromising their properties. [61] For the $RMnO_3$, the low magnetic ordering temperature (around 70K to 100 K) makes most of the effort focused on the ferroelectricity part. In order to increase the magnetic ordering temperature, one possible way is to replace Mn with Fe. Due to the much stronger interaction between Fe^{3+} ions in the lattice structure, the magnetic ordering temperature is expected to be dramatically higher.

$RMnO_3$ compounds crystalize in either hexagonal structure with C_{6V}^3 symmetry for small R ionic radius (R=Ho, … Lu, Y or Sc), or an orthorhombic structure with D_{2h}^{16} symmetry for large R ionic radius (R= La,…Dy, Bi). For orthoferrites $RFeO_3$, for all the R, the stable and most known structure is the orthorhombic phase (o-$LuFeO_3$) as shown in table 3.1. O-$RFeO_3$ is a non-polar antiferromagnet below TN=620K due to its central symmetric structure. The a-axis is its magnetic easy axis. The canting in the a-c plane results in weak ferromagnetism.[62] In contrast, spin frustration on the hexagonal lattice will lead to a more interesting magnetic behavior in h-$RFeO_3$. H-$RFeO_3$ is only stable at high temperature and metastable at room temperature. In previous work, few reports can be traced where h-$RFeO_3$ were synthesized through quenching high temperature melt rapidly to get some h-$RFeO_3$ phase nanoparticles as an impurity in o-$RFeO_3$ bulk. Recently, people show the room temperature h-$RFeO_3$ can be stabilized by using epitaxial strain. Amongst the ABO_3 compounds that crystallize in a hexagonal structure, a non-polar $P6_3/mmc$ ($YAlO_3$) phase forms at large tolerance factor, but a polar $P6_3cm$ ($LuMnO_3$) phase is found for $t <\approx 0.88$.[63] This polar structure, which lies as the origin of the ferroelectricity of $YMnO_3$ [64,65] and results in a polarization perpendicular to the hexagonal plane, is in fact found in metastable bulk h-$LuFeO_3$ [39] and inferred from second harmonic generation in epitaxial films [63,66]. Thus, there is a possibility of a robust room-temperature ferroelectric polarization with structural origin exist in h-$LuFeO_3$. [39,63,66,67] In our recently study on the single crystal h-$LuFeO_3$ film, beside the previously reported weak ferromagnetic at 130K, we first observe the room-temperature antiferromagnetic order from the elastic neutron scattering measurement and derived the possible magnetic structure. We also see the ferroelectric switching in h-$LuFeO_3$ through the Piezo Forced Microscopic measurement. Coexistence of antiferromagnetism and ferroelectricity at room temperature make h-$LuFeO_3$ a material not only promising for technological applications

but more importantly, extremely intriguing for fundamental research. Based on this, detailed study of the structure and ferroelectric behavior changes should be very critical to have a comprehensive understand of this new h-$RFeO_3$ multiferroic material.

Table 3.1 Neel temperatures of $RMnO_3$ and $RFeO_3$ compounds. $RMnO_3$ compounds crystalize in either hexagonal structure for small R ionic radius or an orthorhombic structure for large R ionic radius (h means hexagonal structure). In $RFeO_3$ compounds, the stable phase has orthorhombic structure.

T (K)	RVO_3	$RCrO_3$	$RMnO_3$	$RFeO_3$
Y	116	140	h	640
R=La	143	282	141	690 (740?)
Ce	124			>600 K
Pr			95	707
Nd		219	75 (82)	687 (760)
Pm				
Sm				673
Eu	131		49	662
Gd		170		678
Tb			41	692
Dy	110	142	39	645
Ho	113		h	700
Er	112	133	h	620
Tm			h	
Yb	94		h	650
Lu	116	111	h	623

3.2 Experimental details

In this thesis, epitaxial hexagonal $LuFeO_3$ thin films were grown using pulsed laser deposition (PLD) with a KrF (λ=248 nm) laser on Al_2O_3 (0001) substrates (CrysTec) and onto sputtered epitaxial Pt films (30 nm) on Al_2O_3 (0001) at 750 ^oC in 5 mTorr oxygen pressure. Sapphire substrate was degreased in acetone, methanol and then annealed in O_2 for 3 hours at 1000 °C. After growth, the films were annealed at 950 ^oC in the growth chamber at the same oxygen pressure to improve the crystallinity before cooling to room temperature. The energy density of the laser was 1-2 J cm^{-2} with a repetition rate of 3-10 Hz. The target was a sintered mixture of Lu_2O_3 and Fe_2O_3 (Alpha Aesar 99.99%) with 1:1 molar ratio. The target-substrate distance was 3.5 cm. The substrates were clamped on a Pt foil covered heater. No adhesive is involved. The sample temperature was measured by a pyrometer (Omega).

The film structure was determined from *in-situ* reflection high energy electron diffraction (RHEED) and *ex-situ* by X-ray diffraction (XRD) and transmission electron microscopy (TEM) data. Piezoresponse force microscopy (PFM) was carried out on a film deposited on an epitaxial 30 nm Pt film on Al_2O_3 substrates. The neutron scattering experiments were carried out on the HB1A thermal triple axis spectrometer at the High Flux Isotope Reactor, Oak Ridge National Laboratory. We used pyrolytic graphite (PG) as a monochromator and analyzer with the incident and final neutron energies fixed at E_f = 14.7 meV. Two PG filters were used to eliminate higher order neutron contamination. The background and any high temperature nuclear contributions to the intensities have been subtracted. The temperature and field dependence of the magnetization were measured using a superconducting quantum inference device (SQUID) magnetometer. The background subtraction of the magnetization is done by assuming the magnetization is saturated

at high magnetic field at 300 K. Notice that the choice of background subtraction will not affect the ZFC-FC splitting. The temperature dependence of X-ray magnetic linear dichroism (XMLD) was studied using polarized synchrotron x-rays at beam line 4-ID-C at the Advanced Photon Source. Transmission electron microscopy (TEM) work was carried out on a Cs-corrected FEI Titan 80/300-kV TEM/STEM at the Oak Ridge National Laboratory. TEM specimen was prepared with traditional mechanical polishing followed by ion milling.

3.3 Growth, epitaxial relation and lattice constant

Figure. 3.1(a) shows a unit cell of the bulk h-$LuFeO_3$ viewed from the [1 0 0] direction. [39] This polar structure is isomorphic with that of hexagonal $YMnO_3$. As shown in Fig. 3.1(b**)**, the XRD pattern displays sharp and intense (00L) (L=2n) peaks of the h-$LuFeO_3$ film and the (00L') (L'=2n+1) peaks of the Al_2O_3 substrate, suggesting that the films are grown along the (001) direction without detectable impurity phases. The interference fringes around the h-$LuFeO_3$ peaks, as exemplified in the inset, indicate high film quality. The full width at half maximum of h-$LuFeO_3$ (002) is about 219 arcsec (Fig. 3.2(a)), which is also an indication of high film quality. Pole-figure scans of the h-$LuFeO_3$ {1̄22} peaks as shown in Fig. 3.2(b) exhibiting the expected six-fold symmetry. The radial direction is the tilt angle ψ between the normal direction of the film and the diffraction plane (0° to 90°); and the angular direction is the rotation angle ϕ (0° to 360°). The sharp spots without satellites or broadening indicate that the as-grown film has a highly crystalline structure. Atomic force microscopy (AFM) images of an $\alpha-Al_2O_3$ (0001) substrate and a 20 nm h-$LuFeO_3$ film showing atomic terraces, indicate the flatness of the films (Fig. 3.3 (a,b)).

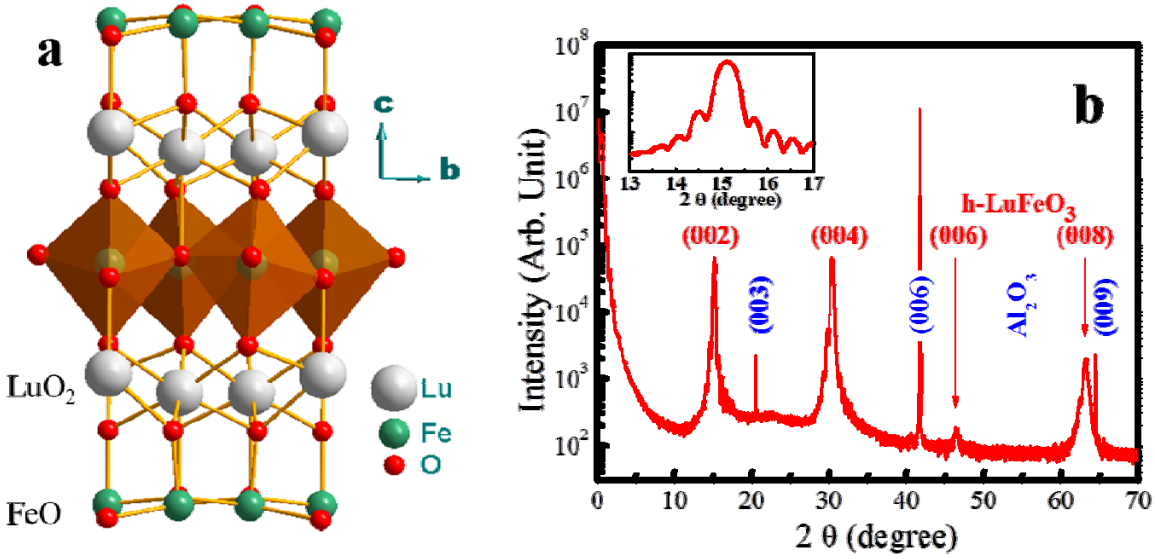

Figure 3.1 (a) The structure of bulk h-$LuFeO_3$ viewed from the [1 0 0] direction. The trigonal-bipyramid local environment of Fe atoms in the middle layer is displayed. (b) The typical θ-2θ scan of an h-$LuFeO_3$ film.

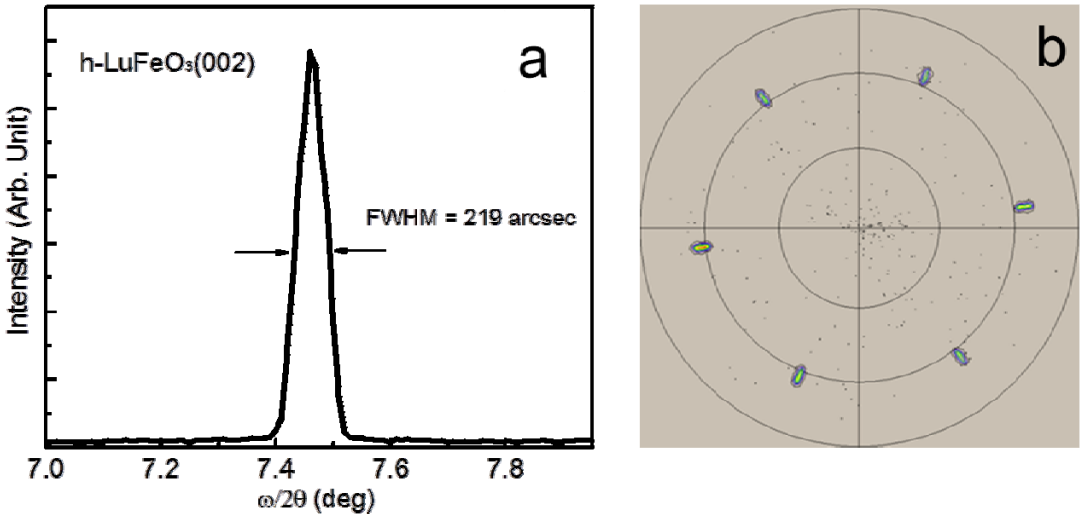

Figure 3.2 (a) Typical ω/2θ rocking curve of the h-$LuFeO_3$ (002) peak. (b) Pole-figure scans of the h-$LuFeO_3$ {ī22} peaks exhibiting the expected six-fold symmetry. The radial direction is the tilt angle ψ between the normal direction of the film and the diffraction plane (0° to 90°); and the angular direction is the rotation angle ϕ (0° to 360°).

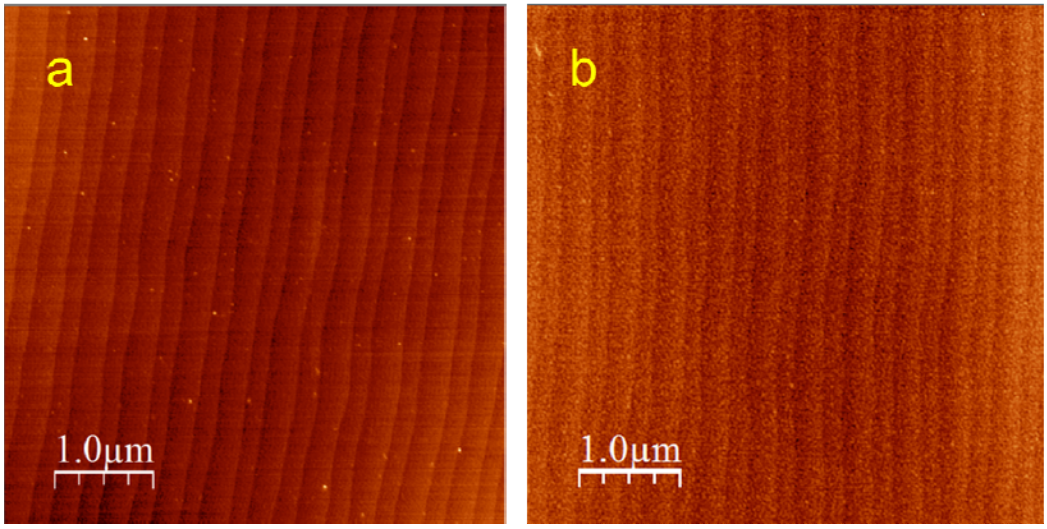

Figure 3.3 Atomic force microscopy (AFM) images of an α−Al_2O_3 (001) substrate (a) and a 20 nm h-$LuFeO_3$ film (b) showing atomic terraces. The terrace structure of the h-$LuFeO_3$ film is similar to that of the substrate, confirming a high film quality.

The combination of in-situ structure characterization using RHEED and ex-situ characterization by XRD allows assignment of the epitaxial relation between the h-$LuFeO_3$ film and the Al_2O_3 substrates. The strong h-$LuFeO_3$ (002), (004), (006) and (008) peaks observed in x-ray diffraction θ-2θ scan in Fig. 3.1(b) indicate that the epitaxial relation is h-$LuFeO_3$ [001]//α-Al2O3[0001]. Fig. 3.5 (a), (b), (c), (d) show the RHEED patterns of the Al_2O_3 substrates and the h-$LuFeO_3$ film with the direction of the electron beam along Al_2O_3 [100] and Al_2O_3 [1-10], respectively. This result indicates that the in-plane epitaxial relation is h-$LuFeO_3$ [100]//Al_2O_3[100], which was further confirmed by the x-ray ϕ-scan measurement(Fig. 3.4(a)).The ϕ-scan measurement on both the substrate and film show that the Al_2O_3 {ī23} planes are well aligned with h-$LuFeO_3$ {ī24} planes in terms of the angle ϕ, which also approves the in-plane epitaxial relation is Al_2O_3 [100]//h-$LuFeO_3$ [100].

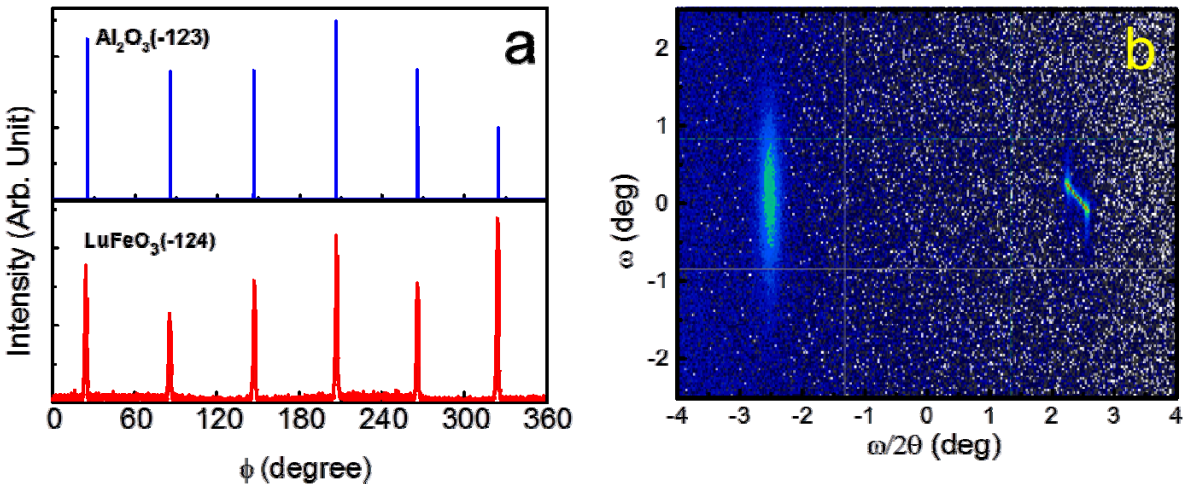

Figure 3.4 (a) The ϕ-scan of an h-$LuFeO_3$ films indicating epitaxial relation h-$LuFeO_3$ [0 0 1]// Al_2O_3 [0 0 1]. (b) Typical XRD ω-2θ scan with the peaks of Al_2O_3(-123) and h-$LuFeO_3$ films (-122).

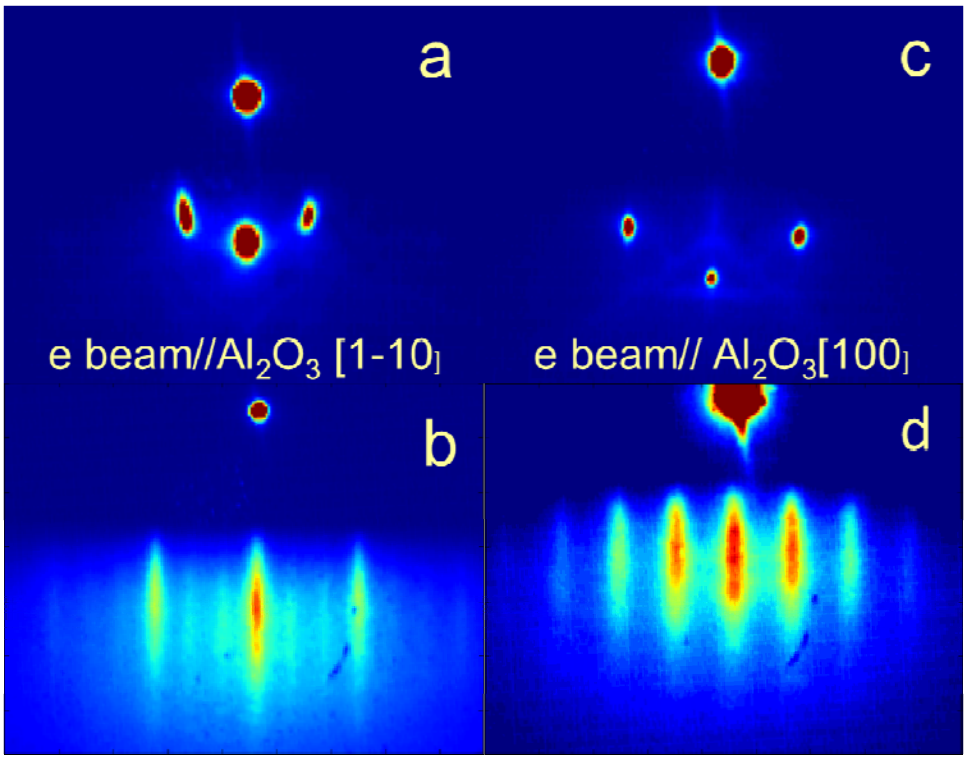

Figure 3.5 RHEED patterns of Al_2O_3 substrates (a,b) and h-$LuFeO_3$ (c,d)films with the electron beam // Al_2O_3 [100] direction and Al_2O_3 [1-10] direction respectively at 300 K.

Since the epitaxial strain will change the lattice constant of the film and further influence the electronic as well as magnetic properties of material, it is very important to accurately measure lattice constant values of the epitaxial thin film. In our experiment, we use X-ray diffraction to measure the lattice parameters of the h-LuFeO3 films. Typical XRD ω-2θ scan is shown in Fig. 3.4(b). The right and left peaks originated from the Al_2O_3 (-123) and h-LuFeO3 films (-122). The result shows that the two planes have almost the same offsite angle, which also confirmed that the in plane epitaxial relation is Al2O3 [100]//h-LuFeO3 [100]. From both the c direction θ-2θ scan and h-LuFeO3 (-122)'s ω-2θ scan, the lattice constants of h-$LuFeO_3$ thin film are a=b=5.789Å, c= 12.000Å, indicating an expansion at a and b axis while a contraction at c-axis as compared to the reported bulk values a=b=5.965Å and c=11.702Å.

In this thesis, most of the measurements were done on the h-$LuFeO_3$ film grown on Al_2O_3 (0001) substrate, but we also grown high quality single crystal thin film on top of sputtered epitaxial Pt (111) films on Al_2O_3 (0001), yttrium stabilized zirconium oxides (YSZ) (111) and $MgAl_2O_4$(111) substrates. The crystal structure and observed epitaxial relationship between substrate and h-$LuFeO_3$ films are shown in Fig. 3.6. The lattice mismatch between the film and the substrate on Pt, YSZ and $MgAl_2O_4$ are -6.3%, 5.6% and -4.3% respectively.

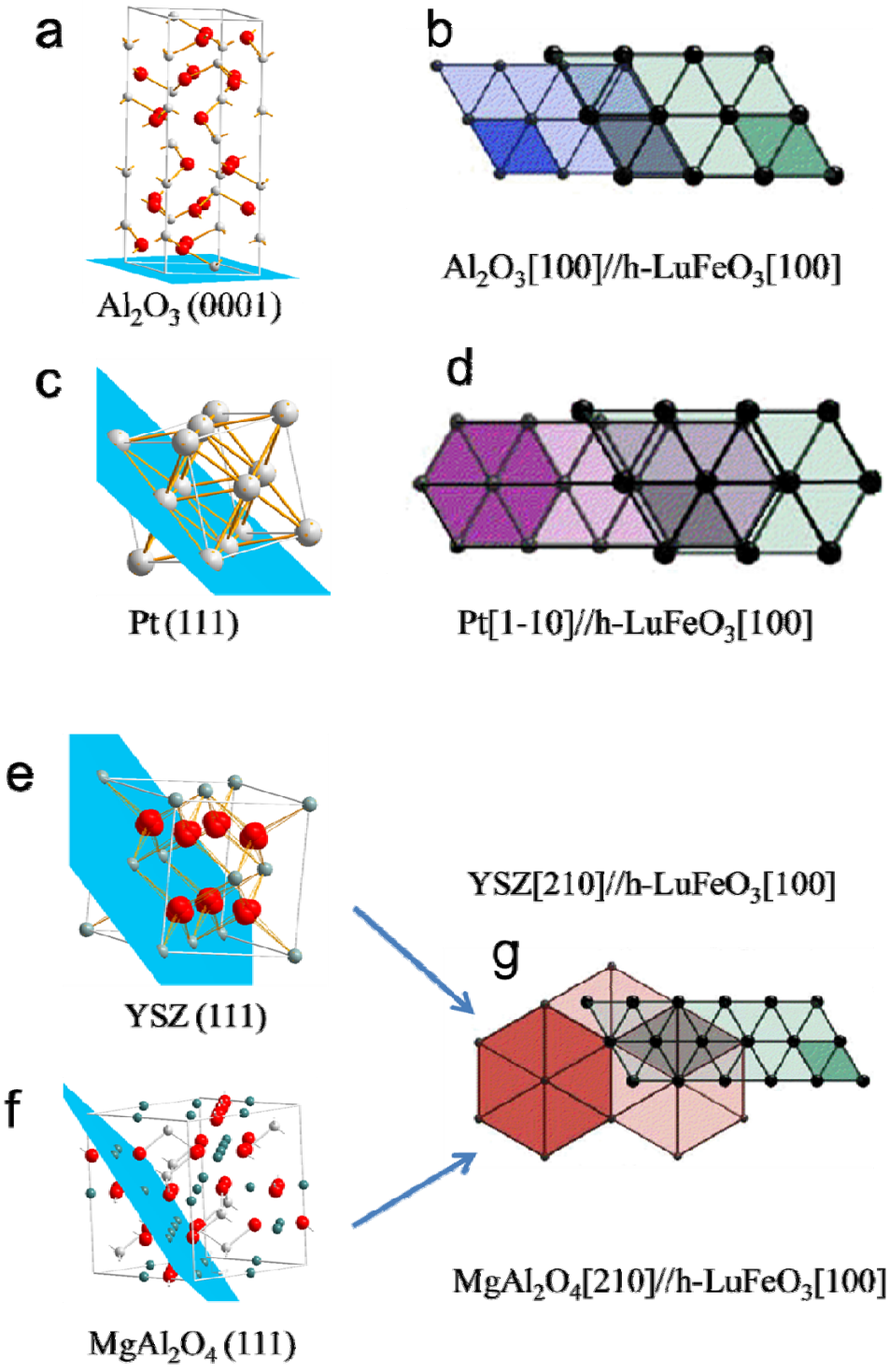

Figure 3.6 Crystal structure of substrate Al_2O_3 with the (0001) growth plane highlighted (a); Pt with the (111) growth plane highlighted(c); YSZ with the (111) growth plane highlighted (e); $MgAl_2O_4$ with (111) plane highlighted (f). The epitaxial orientation relationship of a $LuFeO_3$ lattice on (0001) Al_2O_3(b); (111) Pt(d); (111)YSZ and (111)$MgAl_2O_4$(g).

3.4 Crystal field splitting and optical band gap

We investigate the electronic properties of h-$LuFeO_3$ films using x-ray absorption and optical spectroscopy. The analysis of the x-ray absorption spectra (XAS) using crystal field theory reveal a splitting of the Fe 3d levels significantly higher than that of Fe^{3+} in $LuFe_2O_4$, indicating stronger Fe-O interactions. The extracted optical band gap from optical absorption spectra is 2.0 ± 0.1eV, somewhat smaller than perovskite ferrites[68]. The experimental findings have been confirmed by our electronic structure calculations.

The x-ray absorption spectroscopy was carried out on 50 nm h-$LuFeO_3$ films grown on Al_2O_3 substrates using PLD with 30 nm Pt buffer layer (Fig. 3.7(a)) to avoid charging effect. The XAS was taken at beam line 4-ID-C at the Advanced Photon Source using polarized synchrotron x-rays. A 20 nm thick h-LuFeO3 film was grown on YSZ(111) substrates using PLD (Fig. 3.7(b)) for optical spectroscopy measurements. Part of the substrate was covered by a mask during growth so it can be used as a reference in the optical transmittance measurement. Optical spectra were collected in transmittance mode using a Varian Cary 5000 spectrometer.

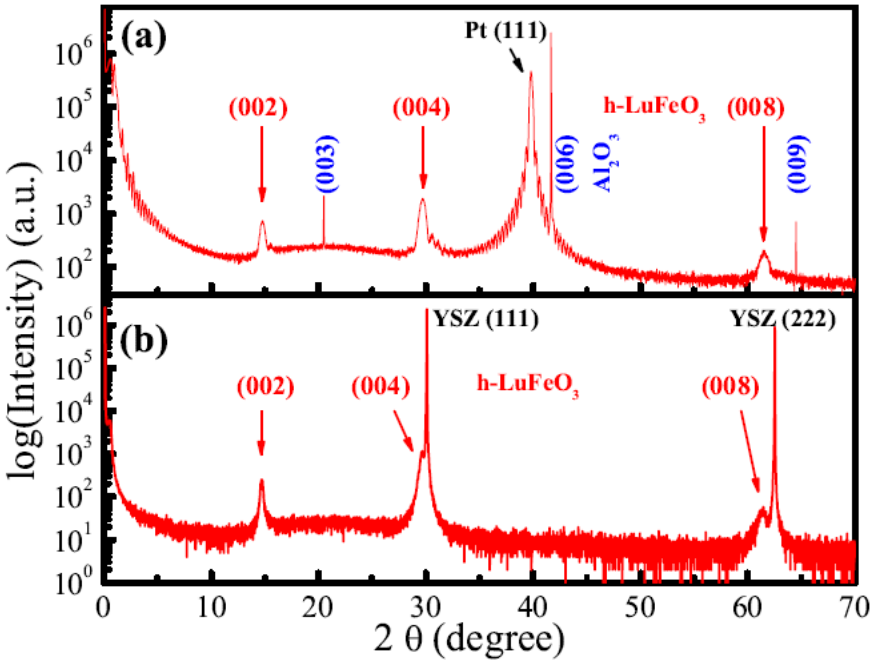

Figure 3.7 The x-ray diffraction spectra of h-LuFeO3 films grown on (a) Al2O3 substrates with Pt buffer layer and (b) YSZ substrates.

Figure 3.8 (a) shows the XAS corresponding to transitions from a Fe $2p^6 3d^5$ to a Fe $2p^5 3d^6$ multiplet. In the spectra, two groups of peaks separated by approximately 12eV can be distinguished. For each group, fine structures depending on the polarization can be recognized: two well-separated peaks (709.1 and 710.7eV) are observed for the s polarization, while additional intensity is observed for p polarization as a peak at 709.8 eV.

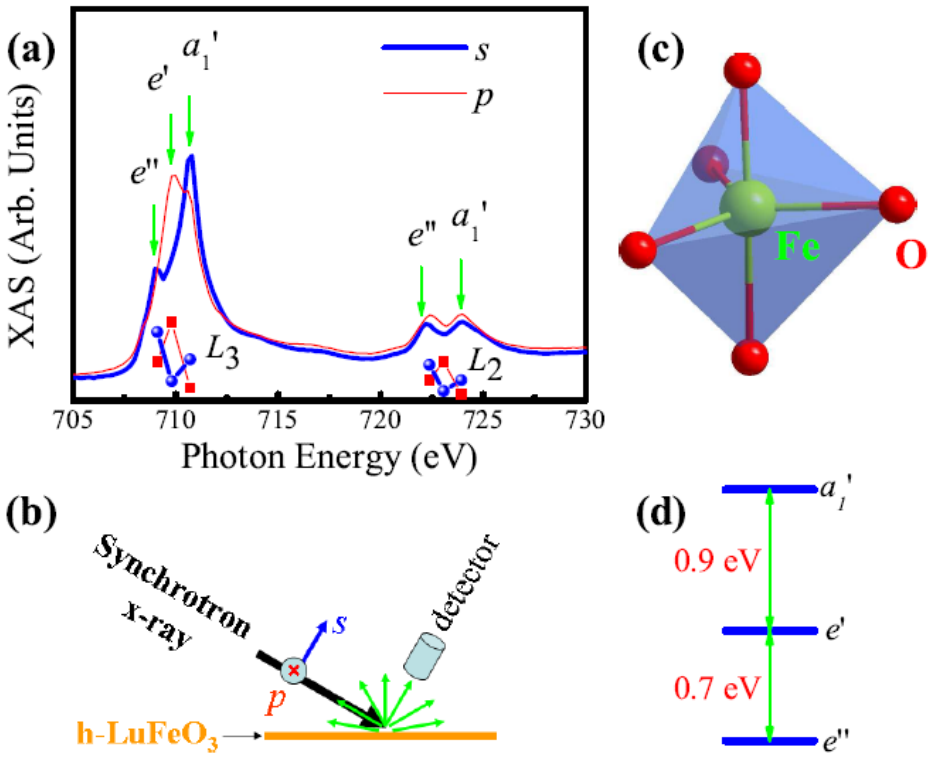

Figure 3.8 Crystal field splitting of Fe site (300 K). (a) The x-ray absorption spectra corresponding to Fe 2p to Fe 3d excitation. The symbols are the calculated matrix elements from the initial to the final on-electron states (see text). (b) Schematics of the experimental setup. (c) Schematics of the local environment of Fe sites. (d) The crystal splitting extracted from the XAS spectra.

These spectra details are determined by dipole and spin selection rules and a combination of effects from crystal-field, spin-orbit coupling, d-p and d-d interactions and Fe3d O2p hybridization[69,70]. In terms of one-electron energy, the Fe 2p states are split into $2p_{1/2}$ and $2p_{3/2}$ by the spin-orbit coupling, which has the energy scale of 15eV, resulting in the two groups of excitations L_2 ($2p_{1/2}\rightarrow 3d$) and L_3 ($2p_{3/2}\rightarrow 3d$) in Fig. 3.8(a)[69,71]. For the Fe 3d states, the one-electron states are mainly split by crystal fields, which is on the order of one eV[69,71]. Here the trigonal-bipyramid local environment of Fe gives rise to a symmetry that can be represented by the D_{3h} point group as a good approximation, as shown in Fig. 3.8 (c). In this case, Fe 2p orbitals

can be reduced to states corresponding to irreducible representations (IR) e′(x, y) and a″$_2$ (z) states while Fe 3d states split into IR e″(xz, yz), e′(xx−yy, xy) and a′$_1$ (zz)[72].A recent work on $LuFe_2O_4$ in which Fe^{3+} also sit in a trigonal-bipyramid local environment, has shown that the energies of these crystal field states follow Ea′$_1$ > Ee′ > Ee″ [52] . Similar results are also found for Mn^{3+} in a D_{3h} symmetry[73].

According to Hund's rule, the ground states of Fe^{3+} are a multiplet 6A′$_1$ for an $2p_{3/2}^4 2p_{1/2}^2 3d_{e''}^2 3d_{e'}^2 3d_{a'_1}^1$ electronic configuration. In the ionic model that ignores hybridization between Fe3d and O2p state, the spin-allowed excited state multiplets and the corresponding one-electron state populations can be listed as shown in Table 3.2[70]. These multiplets are divided into groups due to the p-d interactions, which have an energy scale of 5 eV [69]. Since the ground states multiplet have a symmetry of A′$_1$, the dipole-allowed excited states need to contain E′ or A″$_2$ to satisfy the dipole selection rules for a D_{3h} symmetry[72]. The resulting dipole-allowed transitions are listed in Table 3.2. It is clear that the photon with z polarization cannot excite an electron from Fe 2p to Fe 3d$_{e'}$ state. These selection rules are verified in the L_3 part of the XAS: for s polarization, the peak in the middle is much weaker, which suggests that the three peaks at 709.1, 709.8 and 710.7 eV are coming from the effect of crystal field.

The transition probability in the XAS depends on the matrix $\left|< \psi_i \left| \hat{E} \cdot \vec{r} \right| \psi_f > \right|^2$, where the ψ_i and ψ_f are the initial and final one-electron states, $\hat{E}$ is the direction vector of the electric field, and $\vec{r}$ is the position vector. As shown in Fig. 3.8 (a) as symbols, the calculated matrix elements qualitatively agree with the dichroism for L_3 excitation. The less obvious agreement for L_2 excitations is presumably due to a mixed energy splitting from crystal field and p-d interactions[69]. The peak positions allow for a rough determination of the crystal field splitting assuming similar

d-d interactions for different Fe 3d states: Ee′ − Ee″=0.7 eV and Ea′$_1$ − Ee′=0.9 eV, as also shown in Fig. 3.8(d). These splitting are significantly larger than those in $LuFe_2O_4$ (Ee′ − Ee″=0.4 eV and Ea′$_1$ −Ee′=0.8 eV for Fe^{3+} sites)[52]. The differences indicate a stronger Fe-O interactions, as also suggested by the different Fe-O bond length in h-$LuFeO_3$ and those in $LuFe_2O_4$.[38]

Table 3.2: The spin-allowed excited states and the dipole selection rules from the 6A′$_1$ ($2p^4_{3/2}2p^2_{1/2}3d^2_{e''}3d^2_{e'}3d^1_{a'_1}$) ground state with a linearly polarized photon.

$2p$	$3d$	IR	Allowed
$2p^4_{3/2}2p^1_{1/2}$	$3d^3_{e''}3d^2_{e'}3d^1_{a'_1}$	$A''_1+A''_2+E'+E''$	x,y,z
	$3d^2_{e''}3d^3_{e'}3d^1_{a'_1}$	$A''_1+A'_2+E'+E''$	x,y
	$3d^2_{e''}3d^2_{e'}3d^2_{a'_1}$	$E'+A''_2$	x,y,z
$2p^3_{3/2}2p^2_{1/2}$	$3d^3_{e''}2d^2_{e'}3d^1_{a'_1}$	$A''_1+A''_2+E'+E''$	x,y,z
	$3d^2_{e''}2d^3_{e'}3d^1_{a'_1}$	$A''_1+A'_2+E'+E''$	x,y
	$3d^2_{e''}2d^2_{e'}3d^2_{a'_1}$	$E'+A''_2$	x,y,z

In order to further elucidate the electronic structure of the h-$LuFeO_3$, we measured optical absorption of the h-$LuFeO_3$ films. The observed spectra (Fig. 3.9) shows three peak-like features at approximately 2.3, 2.9 and 3.9 eV, consistent with the recently reported optical properties of h-$HoFeO_3$ and h-$ErFeO_3$ films[74]. Based upon the overall intensity ~ 10^7 cm^{-1}, these peaks correlate to dipole-allowed excitations. Since the Fe^{3+} has a $3d^5$ configuration, all the on-site excitations are spin forbidden. Therefore, the peak at 2.3 eV is coming from charge transfer

excitations[68]. A 2.0 ± 0.1 eV optical band gap was extracted using plots of α^2 versus energy (Fig. 3.9 in-set), assuming a direct gap.

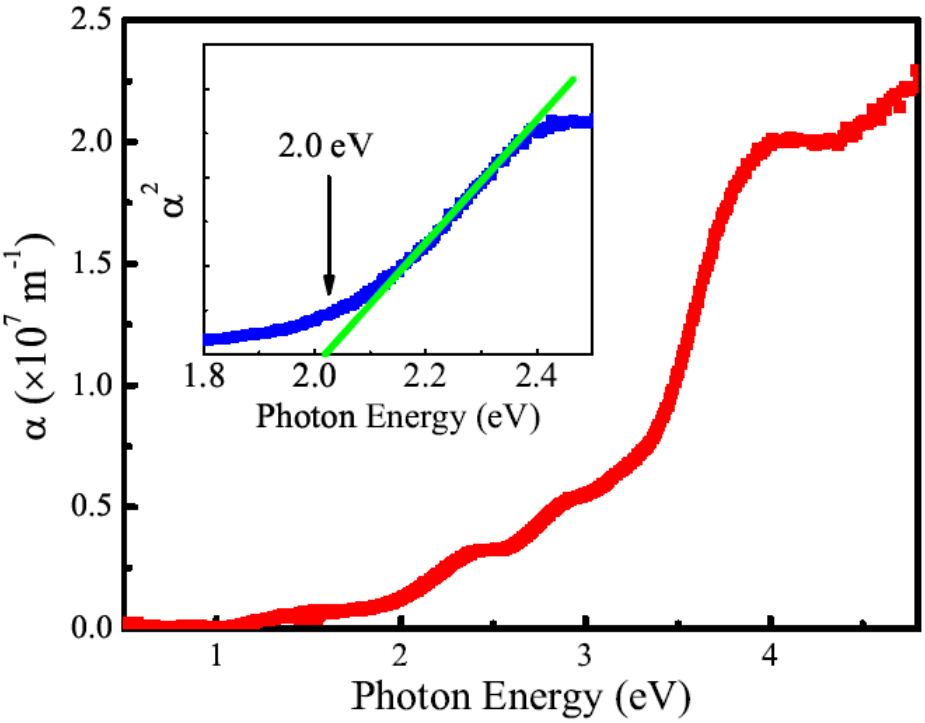

Figure 3.9 Optical absorption coefficient α as a function of photon energy. Inset: α^2 as a function of photon energy which indicates an optical band gap of 2.0 eV.

First-principles electronic structure calculations can provide insightful picture of crystal field splitting. We determined our projected density of states (PDOS) by the density functional theory (DFT) implemented in the Vienna ab initio simulations package (VASP)[75,76]. We adopted the Perdew-Burke-Ernzerhof functional revised for solids (PBEsol)[77] in which the spin-polarized generalized gradient approximation (GGA) is made in treating the exchange correlation effect of electrons. The resulting PDOS is presented in Fig. 3.10. One can clearly see that our theoretical results are consistent with the experimental data where the crystal field states follow $Ea'_1 > Ee' > Ee''$. An unambiguous assignment of the crystal field states and energies can be further obtained

by generating Maximally Localized Wannier Functions (MLWFs)[78] based on the ground state electronic structure in the selected energy window spanning all the crystal field states under consideration. The resulting MLWFs for each crystal field state are shown in Fig. 3.10 and the resulting energies are Ee′ − Ee″ = 0.41 eV and Ea'_1 −Ee′ = 0.81 eV, which are close to the experimental values of 0.7 and 0.9 eV respectively. This qualitative agreement between experiment and theory is expected within the frame work of DFT. However we should be aware that a more proper treatment of electron-hole excitations by GW based Bethe-Salpeter method[79,80] can further improve the theoretical prediction. To overcome the severely underestimated band gap due to the delocalization error arising from the incomplete cancellation of the spurious self-interaction, we used the GGA+U with the effective U value (Ueff=U-J) of 4.61eV[81]. This gives a band gap of Eg = 1.35 eV which still underestimates our experimental value. Again, amore proper treatment of self-energy by GW method will further bring the theoretical predictions closer to the experimental value.

We have studied h-$LuFeO_3$ films using x-ray and optical spectroscopy. Clear dichroism observed in XAS is attributed to the effect of crystal field splitting which is found significantly larger than that of Fe^{3+} in $LuFe_2O_4$, suggesting stronger Fe-O interaction. A 2.0 eV optical band gap originated from charge transfer excitations is determined from the optical spectra. This important information of electron structure, confirmed by DFT calculations will definitely benefit further studies of h-$LuFeO_3$.

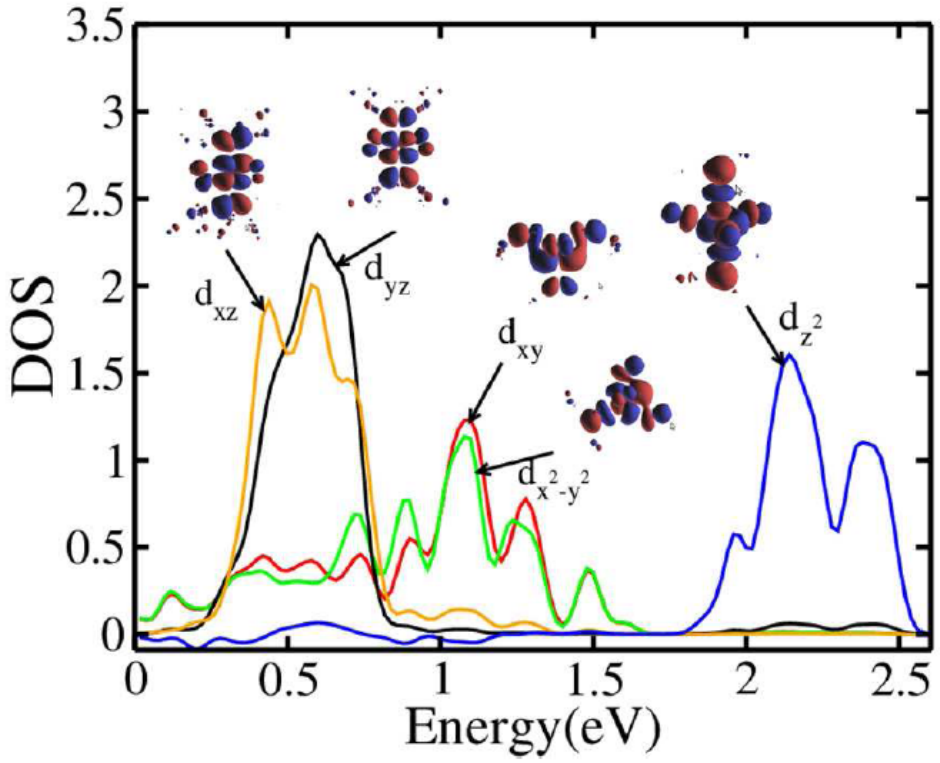

Figure 3.10 Projected density of states for conduction band of h-LuFeO3 with theoretical ground state structure (space group P63cm) and MLWFs (by WIEN2k software package[82,83]) with crystal field splitting states characters.

3.5 Structure characterization and Ferroelectricity

As depicted by Fig. 3.1(a), the local environment of Fe can be characterized as FeO5 trigonal-bipyramids, the tilted FeO5 trigonal-bipyramids generating two inequivalent sites of Lu atoms: 1/3 of Lu atoms are above the other 2/3 of them, corresponding to a $\sqrt{3}\times\sqrt{3}$ reconstruction in the a-b plane. The weak streaks at 1/3, 2/3 positions in the room-temperature Reflection High Energy Electron Diffraction (RHEED) pattern (Fig. 3.5(b)) are in fact consistent with this reconstruction. Figure 3.11 shows the image of high resolution TEM, demonstrating clear layered structure of the h-$LuFeO_3$ films. Fig. 3.11(b) is the scanning TEM image at room

temperature, viewed from [010] direction. The Bright lines correspond to the rows of Lu atoms, which are sandwiched between rows of Fe atoms. The z positions of the Lu rows show clear oscillation with period of three, while Fe rows are close to straight lines, consistent with the h-LuFeO3 structure in Fig. 3.1(a). The observation of this structure is a direct evidence of the non-central symmetry of the h-$LuFeO_3$ films, which is a precondition for ferroelectricity. Looking carefully at the oscillation pattern, one may notice that the oscillating pattern is slightly different from that derived from the bulk h-$LuFeO_3$ structure, which is depicted in Fig. 3.11(c). Rather it is more like the pattern displayed in Fig. 3.11(d). In order to elucidate the detail of the oscillation pattern, we quantified the position of Lu atoms by using Gaussian fit of the intensity profiles. We then calculated the z-position difference between the neighboring atoms, i.e. the position of the Lu atoms subtracted by the position of the Lu atoms on their immediate right. The resulting histogram is shown in Fig. 3.11(e). For the pattern in Fig. 3.11(c), one would expect three peaks with equal population: one at positive position, one at negative position and one at zero position, which is not observed in Fig. 3.11(e). Instead, there are only two peaks in the histogram. The positive (negative) peak represents a set of Lu atoms that are lower (higher) than their left neighbor. The fact that the center of the positive peak is about twice as much as the absolute center of the negative peak and the total counts is only about one half is in good agreement with the pattern in Fig. 3.11(d). This subtle distortion from the h-$LuFeO_3$ bulk structure may be related to the epitaxial strain. In fact, it was also observed in h-$LuFeO_3$ epitaxially embedded in $LuFe_2O_4$ matrix.

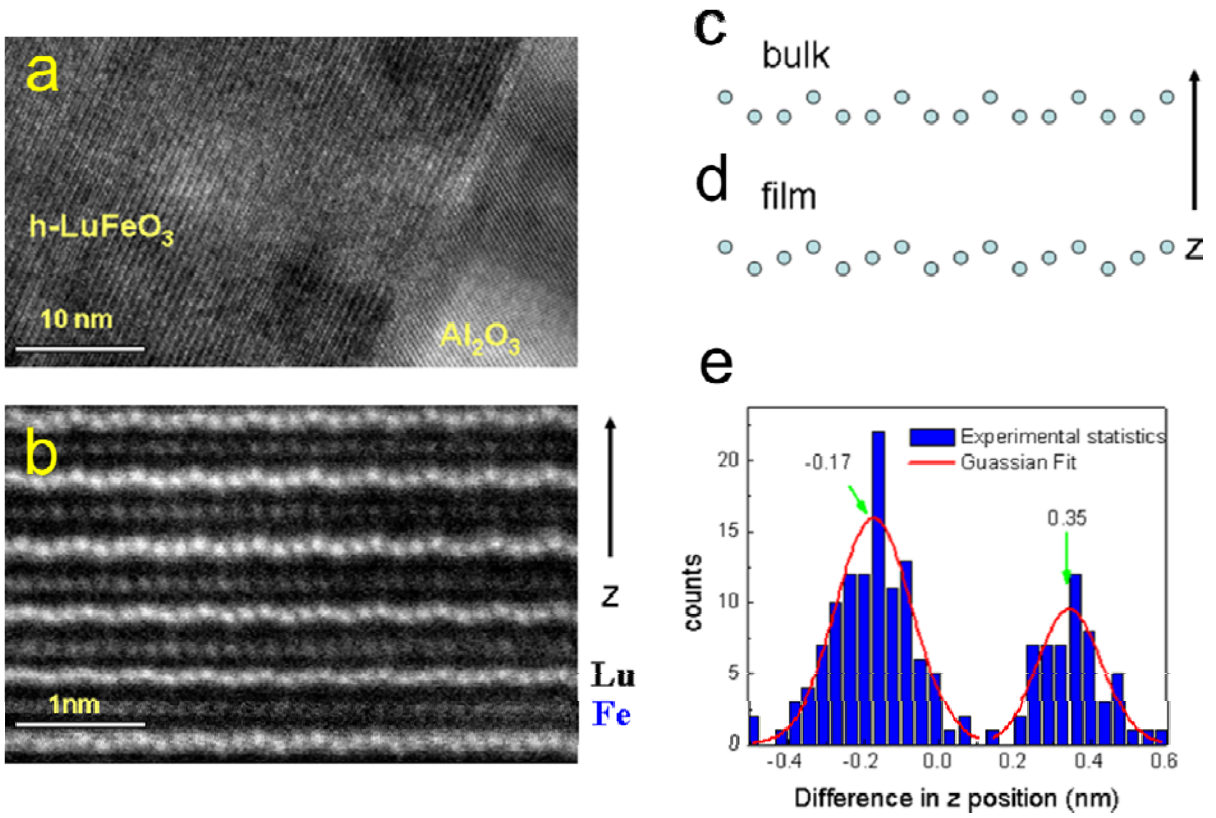

Figure 3.11 (a) High resolution TEM of an h-$LuFeO_3$ film showing clear layered structure. (b) A Scanning TEM image of the h-$LuFeO_3$ film showing positions of Lu atoms. (c) The displacement pattern of Lu atoms derived from the bulk h-$LuFeO_3$ structure. (d) The displacement pattern of Lu atoms proposed for the h-$LuFeO_3$ films. (e) The histogram of the z position difference between neighboring Lu atoms.

The isomorphic polar structure of the h-$LuFeO_3$ films and $RMnO_3$ and the similar structural transition suggests that ferroelectricity with the same mechanism may also exist in h-$LuFeO_3$. For the hexagonal $RMnO_3$, the ferroelectric transition temperature (T_{FE}) is several hundred Kelvin lower than the reported non-polar to polar structure transition temperature (T_{npt}). According to Landau's theory of structural phase transitions, any atomic displacements from the high symmetry phase to low symmetry phase could be transform as a linear combination of

irreducible representations. Table 3.3 show the possible phase transition from $P6_3/mmc$ to $P6_3cm$ in terms of irreducible representations.[8] Δ(X) means the distortions of atom X.

Table 3.3 The possible high-temperature phase transition $P6_3/mmc$ to $P6_3cm$ in terms of irreducible representations

Mode	Volume	SG	Type	$\vec{k}$
Γ_1^+	1	$P6_3/mmc$ (194) D_{6h}^4	Full symmetric	(0,0,0)
Γ_2^-	1	$P6_3mc$ (186) C_{6v}^4	Proper ferroelectric	(0,0,0)
K_1	3	$P6_3/mcm$ (193) D_{6h}^3	Non ferroic	(1/3,1/3,0)
K_3	3	$P6_3cm$ (185) C_{6v}^3	Improper ferroelectric	(1/3,1/3,0)

(1) Γ_1^+ is a one dimensional mode, it gives $P6_3/mmc$ to $P6_3/mmc$;

$\Delta(O(1)) = -\Delta(O(2)) = \lambda_1(O_{ap})\ \hat{C}$

(2) Γ_2^- is a one dimensional mode, it gives $P6_3/mmc$ to $P6_3mc$;

$\Delta(Mn) = \lambda_2(Mn)\ \hat{C}$

$\Delta(R(1)) = -\Delta(R(2)) = \lambda_2(R)\ \hat{C}$

$\Delta(O(1)) = \Delta(O(2)) = \lambda_2(O_{ap})\ \hat{C}$

$\Delta(O(3)) = \Delta(O(4)) = \lambda_2(O_{eq})\ \hat{C}$

(3) K_1 is a two dimensional mode, it gives $P6_3/mmc$ to $P6_3/mcm$;

$\Delta(Mn) = \lambda_3(Mn)\ \bar{A}$

$\Delta(O(1)) = \Delta(O(2)) = \lambda_2(O_{ap})\ \bar{A}$

(4) K_3 is a two dimensional mode, it gives $P6_3/mmc$ to $P6_3cm$;

$\Delta(R(1)) = -\Delta(R(2)) = \lambda_4(R)\ \hat{C}$

$\Delta(O(1)) = -\Delta(O(2)) = \lambda_2(O_{ap})\ \bar{A}$

$\Delta(O(3)) = -\Delta(O(4)) = \lambda_2(O_{eq})\ \hat{C}$

In the h-$RMnO_3$ system, it has been shown that the atomic displacement of h-$RMnO_3$ from the high temperature phase to low temperature phase can be decomposed by two irreducible representations K_3 and Γ_1. In the K_3 mode, the tilting of the MnO_5 bipyramids and corrugating of the R layers causes a tripling of the unit cell and form the$\sqrt{3}\times\sqrt{3}$ reconstruction in the a-b plane. High temperature (HT) symmetry $P6_3/mmc$ changes to the low temperature (LT) symmetry $P6_3cm$. This polar structure does not create ferroelectric moment at this moment. In the second mode $\Gamma 1$, the symmetry is still $P6_3cm$, the O_{ap}-Mn-O_{ap} axis in MnO_5 biphyramid move through z axis and generates a spontaneous polarization. At this stage, we attempt to find this non-polar to polar transition temperature (T_{npt}) and ferroelectric transition temperature (T_{FE}) of h-$LuFeO_3$.

Because the distortion from a non-polar symmetry $P6_3/mmc$ to polar symmetry $P6_3cm$ corresponds to an in-plane $\sqrt{3}\times\sqrt{3}$ reconstruction, which manifests itself as the extra peaks in the XRD. So XRD measurement was used to approach this reconstruction. We measuring the diffraction peaks near Q=(-126), (-1/3,2/3,2) and (-2/3,4/3,4) ($P6_3/mmc$ notation) at 300 K. As shown in Fig. 3.12(a), the presence of (-1/3,2/3,2) and (2/3,4/3,4) super lattice peaks suggests that the inversion symmetry was broken at room temperature. To study the structure change through the temperature, we focus on the diffraction peak (-1/3,2/3,2) and increase the

temperature from 298K to 1025K. As shown in Fig. 3.12(b), a decrease of intensity (-1/3,2/3,2) peak with increase temperature was observed. Because the limitation of the xrd measurement, the highest temperature it can reach is 1025 K , but the peak remained clearly visible at 1025K indicating T_{npt} >1025K.

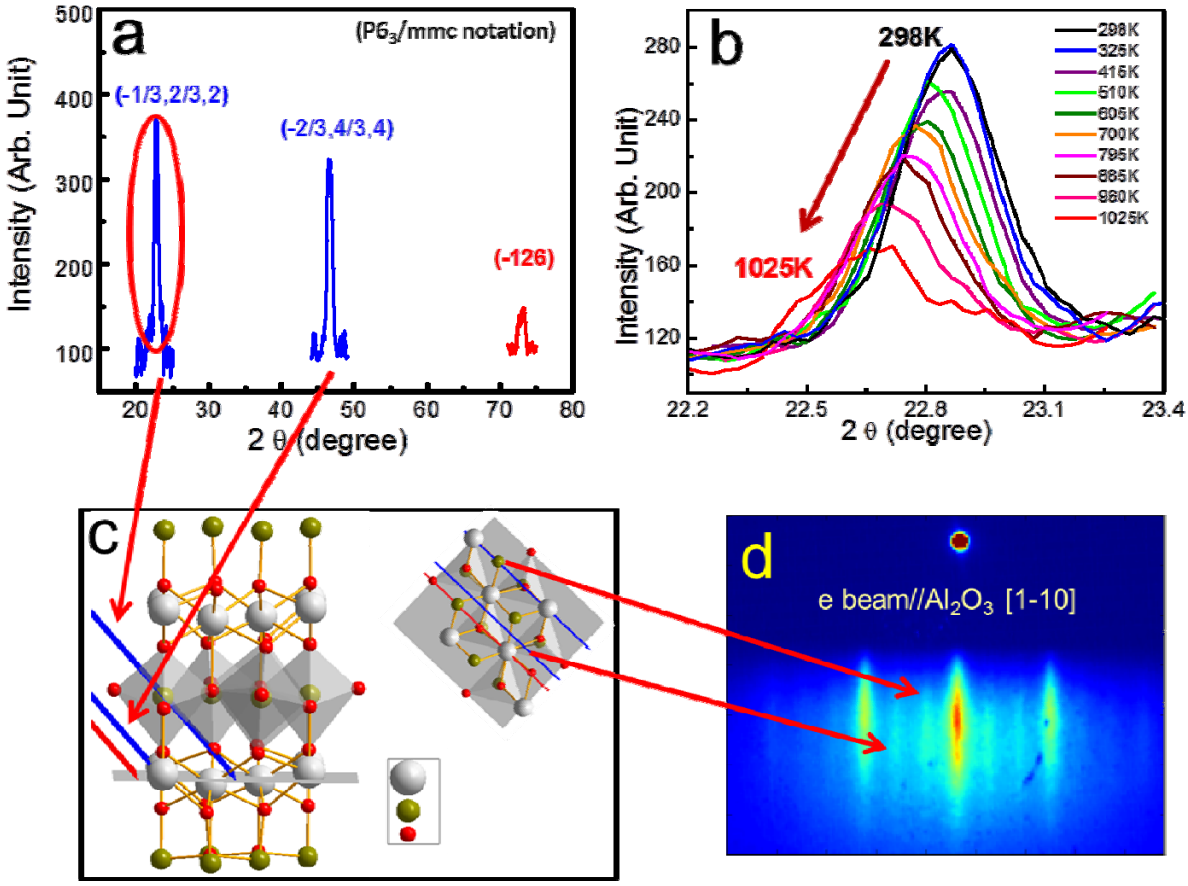

Figure 3.12 (a) θ-2θ scan of the h-$LuFeO_3$ super lattice peaks in the P63/mmc notation at room temperature.(b) Temperature dependence XRD measurement of the (-1/3,2/3,2) peak from 298K to 1025K. (c) The structure of h-$LuFeO_3$ viewed along the [0 0 1] direction and the trigonal-bipyramid local environment of Fe atoms in the middle layer is displayed, also the (-126), (-1/3,2/3,2) and (-2/3,4/3,4) planes are highlighted. Top view of the a-b planes are shown with the intersection line between (-126), (-1/3,2/3,2) and (-2/3,4/3,4) planes. (d) RHEED patterns of h-$LuFeO_3$ films with the electron beam // h-$LuFeO_3$ [1-10] direction at 300 K.

To prove the XRD measurement and figure out the T_{npt}, we use RHEED as another way to approach this structure change. From the Fig. 3.12(c), we can see that the atoms aligned vertically to intersection line between the (-1/3,2/3,2) and (2/3,4/3,4) planes with the a-b plane are exactly the atoms which show this in-plane $\sqrt{3}\times\sqrt{3}$ reconstruction and corresponding to the extra streaks in the RHEED pattern at the 1/3 and 2/3 position shown in Fig. 3.12(d). Using these weak streaks as an indicator of the lattice structure, we were able to track the structural changes with temperature. As shown in Fig. 3.13(b), (c), these reconstruction streaks are visible at 298 K but are absent at 1100 K. The intensity contrast between the reconstruction streaks and the main streaks are over plotted with the integrated intensity of (-1/3,2/3,2) peak from the XRD measurement in Fig. 3.12(b) as a function of temperature. Both XRD and RHEED measurement are consistent very well which shows that T_{npt} is around 1100 K.

To clarify whether the observed structure change from RHEED pattern originates from the thin film itself or a surface effect, we measured the RHEED pattern of the thin film after growth at room temperature with different angles between the electron beam and sample surface. The incident electron beam energy is 34 keV. According to electron beams mean free path, the penetration depth of a 34 keV electron beam is much more than 10 nm. Normally, a grazing incident angle (around 1°) between electron beam and sample surface is used to achieve the good surface sensitivity. However, larger angle can still probe the bulk properties. As shown in Fig. 3.14(a), when the angle between electron beam and sample is small (1.3°), no reconstruction streaks are observed, which means that there is no reconstruction on the surface. On the other hand, the RHEED pattern shows very clear reconstruction streaks (Fig. 3.14(b)) at bigger angle (3.4°), where the electron beam can go much deeper into the sample. This result is also confirmed by the Low energy electron diffraction (LEED) with the energy of 180eV. LEED only

probes the surface structure, because the penetration depth of low energy electron is only about 1-2nms. We see clear hexagonal structure without reconstruction in LEED pattern (Fig. 3.14(d)). Therefore, it is evident that the reconstruction originates from the thin film itself instead of the surface.

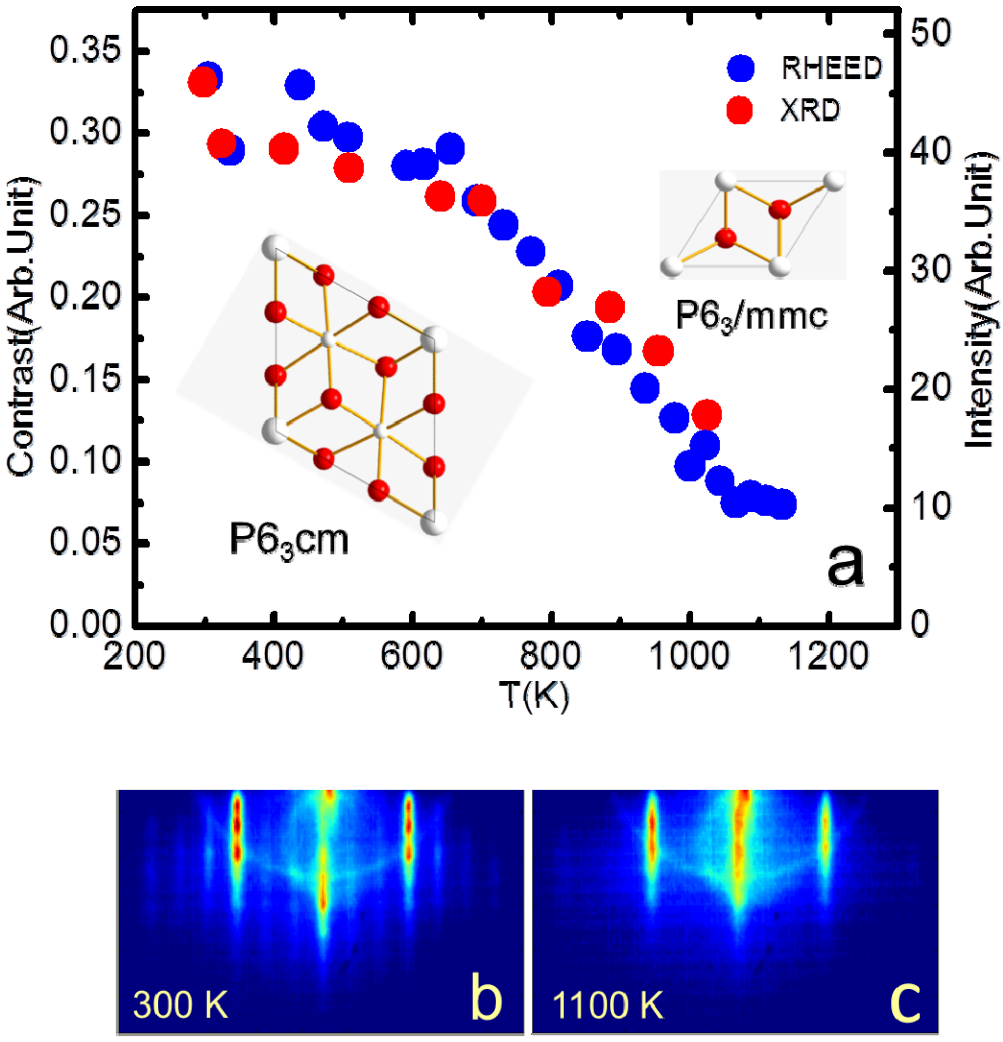

Figure 3.13 (a) Temperature dependence of the intensity contrast between the reconstruction streaks and the main streaks from the RHEED image(blue) are over plotted with the integrated intensity of (-1/3,2/3,2) peak from the XRD measurement (red). The structure models for low temperature symmetry and high temperature symmetry are shown as the insets. (b) and (c) are the RHEED pattern of an h-LuFeO3 films with the electron beam // Al_2O_3 [100] direction at 300 K and 1100 K respectively.

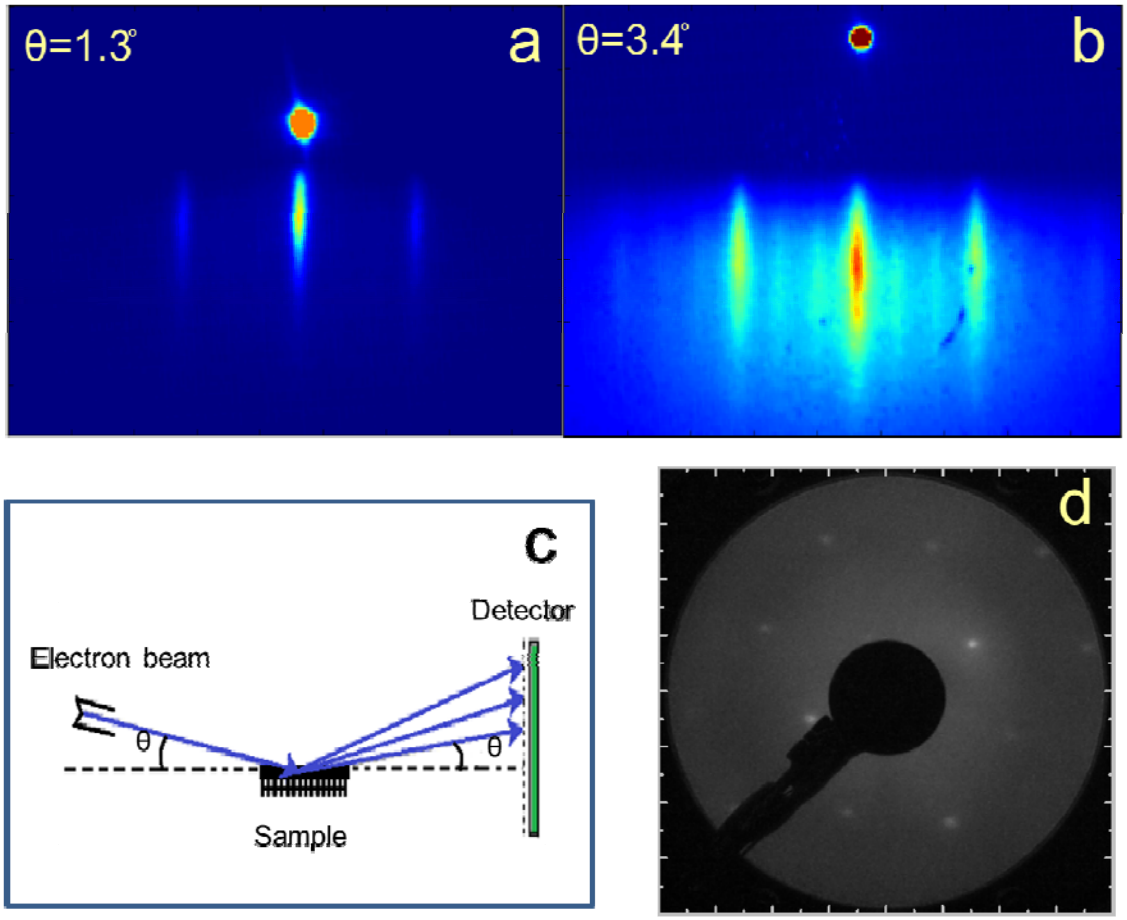

Figure 3.14 RHEED and LEED patterns of the h-$LuFeO_3$ films at 300K. The angle between electron beam and sample surface is 1.3 ℃(a) and 3.4 ℃(b) ; (c) Set up of the RHEED; (d) LEED pattern with the electron energy of 180eV.

Through the structure study, h-LuFeO3 shows the polar structure. To assess possible ferroelectricity in our h-$LuFeO_3$ films, we also studied the switchability of films on the Pt electrodes using PFM [84](The xrd scan of the h-$LuFeO_3$ film grown on 30 nm (111) Pt epitaxial on (0001) Al_2O_3 shown in Fig. 3.15(a)). Here we used Band Excitation Switching Spectroscopy with an ac imaging voltage of 2 V_{ac} and a maximum switching voltage of 12 V_{dc};[85] a metal coated tip (Nanosensors) is used. We measured three piezoresponse loops each on a 10 × 10 point grid in one 3 × 3 μm^2 area and extracted the average switching behavior as displayed in Fig. 3.15(b). The piezoelectric loops show square-shaped loops with switching voltages around 5 V and -7 V, which are indicative of ferroelectric switching.

To concluded, h-$LuFeO_3$ thin films have been shown to have polar structure and ferroelectric switching effect, indicating ferroelectricity.

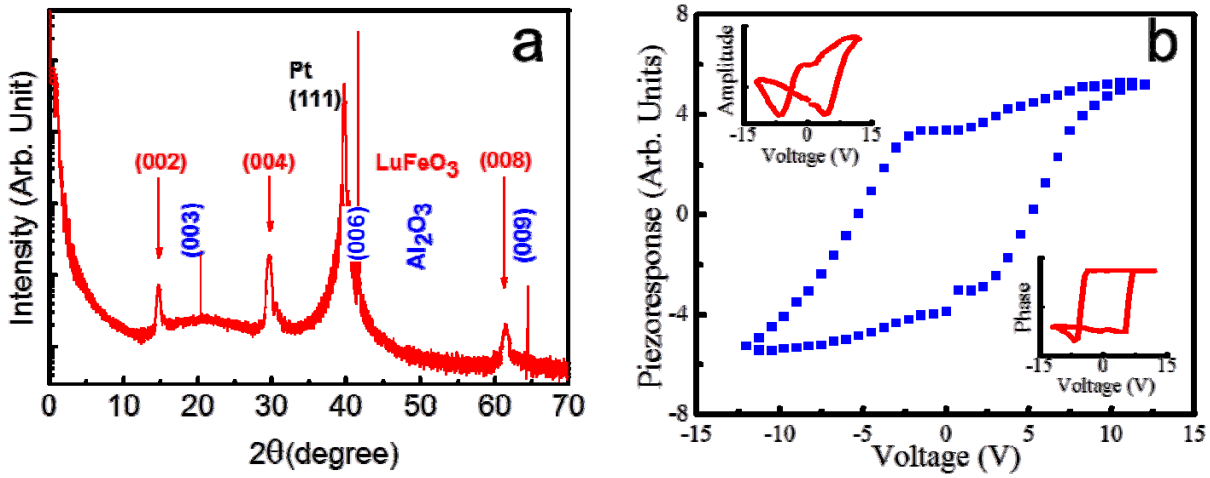

Figure 3.15 Ferroelectric switching effect of the h-$LuFeO_3$ films grown on 30 nm Pt epitaxial on Al_2O_3 substrate. (a) The θ-2θ scan of the h-$LuFeO_3$ film grown on 30 nm Pt epitaxial on Al_2O_3. (b) PFM response showing square-shaped hysteresis loop. The amplitude and phase of the PFM are shown in the insets.

3.6 Magnetic characterization

We now turn our attention to the magnetic properties of these films. Neutron diffraction experiments were carried out to study the magnetic order of h-$LuFeO_3$ thin films. The films were aligned in the (h 0 l) diffraction plane in a closed-cycle refrigerator. At low temperature, several Bragg peaks were clearly observed (Fig. 3.16). As shown in Fig. 3.16 (a) and (c), the (1 0 0) peak intensity drops as the temperature increases up to 130 K while for the (1 0 2) peak the transition occurs at approximately 440 K (Fig. 3.16 (b) and (d)). In contrast, the change of the diffraction peaks (3 0 0) and (0 0 4) with temperature is minimal between 4 K and 450 K (Fig 3.17(a) and (b)). In addition to neutron diffraction, measurements using a superconducting quantum interference device (SQUID) magnetometer revealed that the zero-field-cool (ZFC) magnetization and fieldcool (FC) magnetization split at 130 K under magnetic field along the c-axis, indicating the appearance of a ferromagnetic component of the magnetic moment along the c-axis (Fig. 3.18(a)).

Since h-LuFeO3 is similar in structure with $RMnO_3$ (space group $P6_3cm$) and their magnetic structures can be characterized with the same propagating vector K=0 (magnetic unit cell is the same as the chemical unit cell), we can analyze the magnetic structure of h-$LuFeO_3$ following the symmetry analysis in $RMnO_3$. In this case, the Bragg peaks (1 0 2) and (1 0 0) are in principle coming from a combination of nuclear and magnetic diffractions. However, our structure characterizations do not indicate any clear transition close to 440 K, which is consistent with the fact that in $RMnO_3$ the magnetic diffraction constitutes the majority of the intensity for (1 0 2) peak.[86] Therefore, the transition at 440 K corresponds to the appearance of a long range antiferromagnetic order. Taking T_N=440 K as the antiferromagnetic phase transition temperature,

one can fit between 200 K<T<440 K the peak intensity using $I=I_n+I_m(1-T/T_N)^{\alpha}$ where I_n and I_m are the nuclear and magnetic contributions of the intensity respectively and T is temperature. The result shows $\alpha=0.46$ +/- 0.08, falling well in the reported value range of $YMnO_3$.[87,88] In contrast, the fit for (1 0 0) peak intensity gives a much larger value $\alpha=0.69$ +/- 0.15. The development of ferromagnetic component below $T_R=130$ K suggest that the system displays a second magnetic phase with a ferromagnetic component at low temperature.

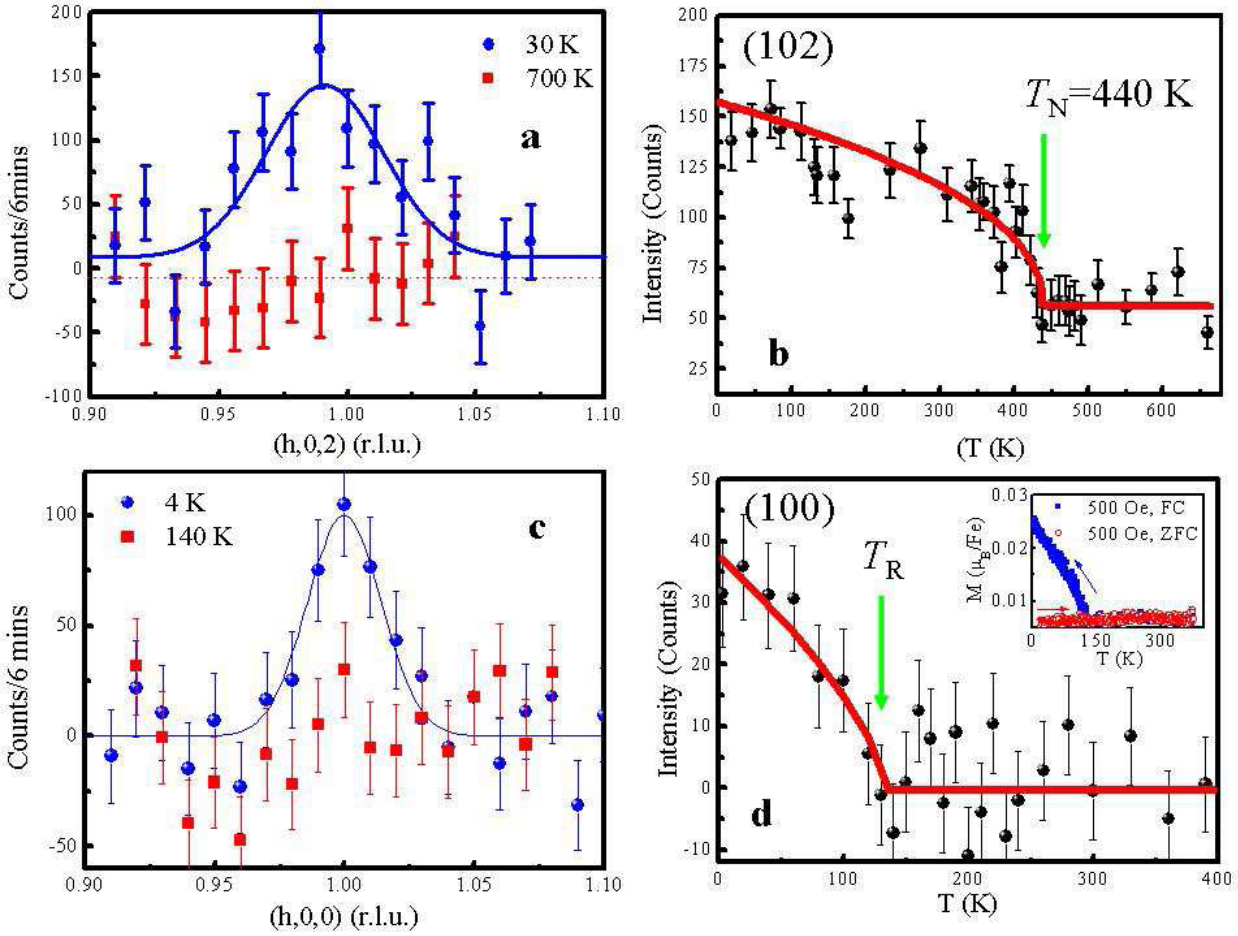

Figure 3.16 Magnetic Bragg peaks and the temperature dependence of their intensities from neutron diffraction. Diffraction intensity profile near the (1 0 2) (a), and (1 0 0) (c) magnetic Bragg points. The lines are the Gaussian fits. Temperature dependence of the intensity of the (1 0 2) (b) and (1 0 0) (d) magnetic Bragg peak. The curves in b and d are fits to the data points (see text). The inset of d shows the temperature dependence of magnetization in ZFC and FC processes with the magnetic field along the c-axis.

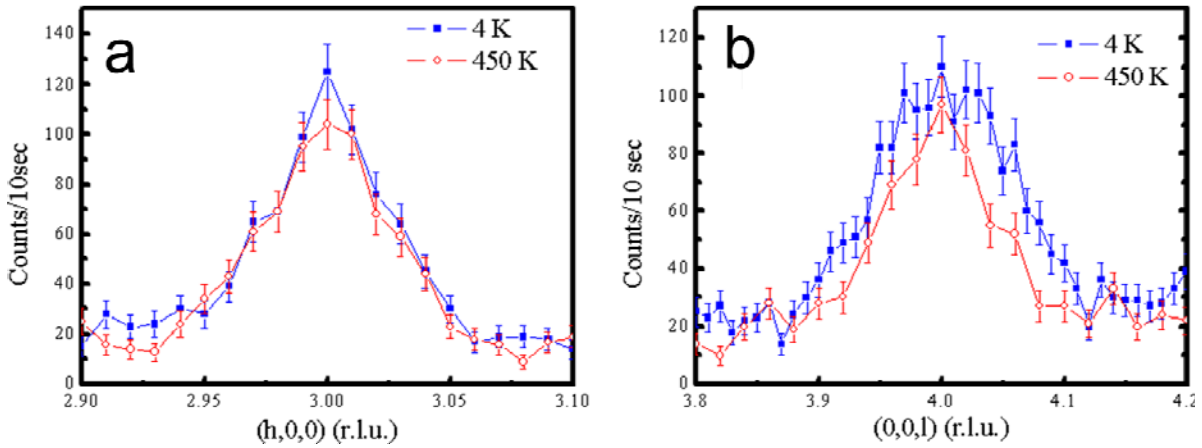

Figure 3.17 Intensity profiles of neutron diffraction near Bragg point (300) (a) and (004) (b).

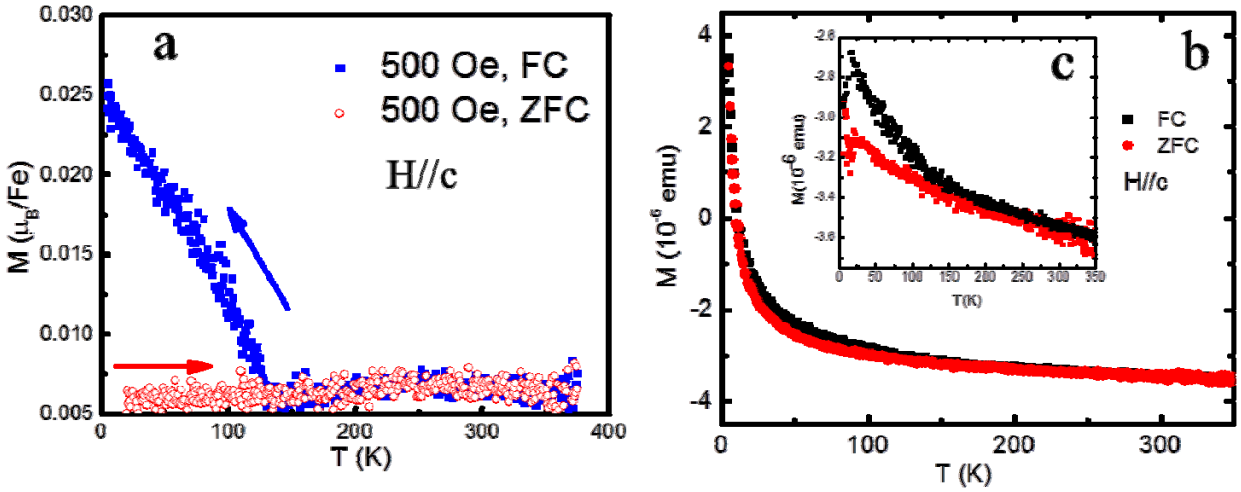

Figure 3.18 Temperature dependence of magnetization (*M-T*) of h-$LuFeO_3$ grown on Al2O3(0001) (a) and YSZ (111) substrates (b),(c) at field-cool (FC) and zero-field-cool (ZFC) conditions (*H*=500Oe). (b) Raw data whose paramagnetic background is so strong that the splitting between ZFC and FC data is not obvious. (c) Data after subtracting the paramagnetic background.

The XMLD measurements confirmed the spin reorientation at low temperature and suggest a magnetic ordering temperature much higher than that. Here the h-$LuFeO_3$ films are illuminated by a synchrotron x-ray polarized along *p* (in plane) and *s* direction, as shown in Fig. 3.19(a). The

photoluminescence and photoelectron signal was collected as a function of incident photon energy at a zero magnetic field. However, the photoelectron spectra are often distorted by the charging effect due to the insulating nature of the h-$LuFeO_3$ films. Therefore, only the photoluminescence data is discussed below. The XMLD signal is proportional to the excitation strength of an electron from deeper level to the valence level by a photon. It measures directly the orbital information of the valence electrons while the spin information is also included due to the spin-orbital coupling. Therefore, it is sensitive to the orientation of the spin (e.g. in-plane or out-of-plane) but no to the sign (e.g. up or down). The advantage of XMLD is that one can specifically examine the magnetic behavior of a certain element. Here we focus on the Fe-L_2 edge, i.e. only the spin orientations of Fe atoms are measured. As shown in Fig. 3.19(b) and (c), the XMLD spectra show an obvious difference for *s*-polarized and *p*-polarized incident photons, indicating a large orbital anisotropy of the Fe^{3+} for in-plane and out-of-plane. What's more interesting is the temperature dependence. As shown in Fig. 3.19(d), the contrast (defined as the integration of the difference spectra between the two polarization directions first increases when the temperature is lowered, but decreases quickly after the temperature is lower than 110 K. If there is no structural transition in the temperature range 50-300 K, the temperature dependence of the XMLD intensity represents the spin structure as a function of temperature. In general the spin order is strengthened at lower temperature, corresponding to the increase of the XMLD intensity. In addition, a spin reorientation toward out of plan tends to decrease XMLD intensity. The competition of the two effects could result in a peak at slight lower than the spin reorientation temperature. The spin reorientation is consistent with that observed from the SQUID data discussed above. Judging from the XMLD data, the magnetic ordering temperature

T_N is very unlikely to be the same as the spin reorientation temperature T_R because of the XMLD intensity keeps changing way above T_R.

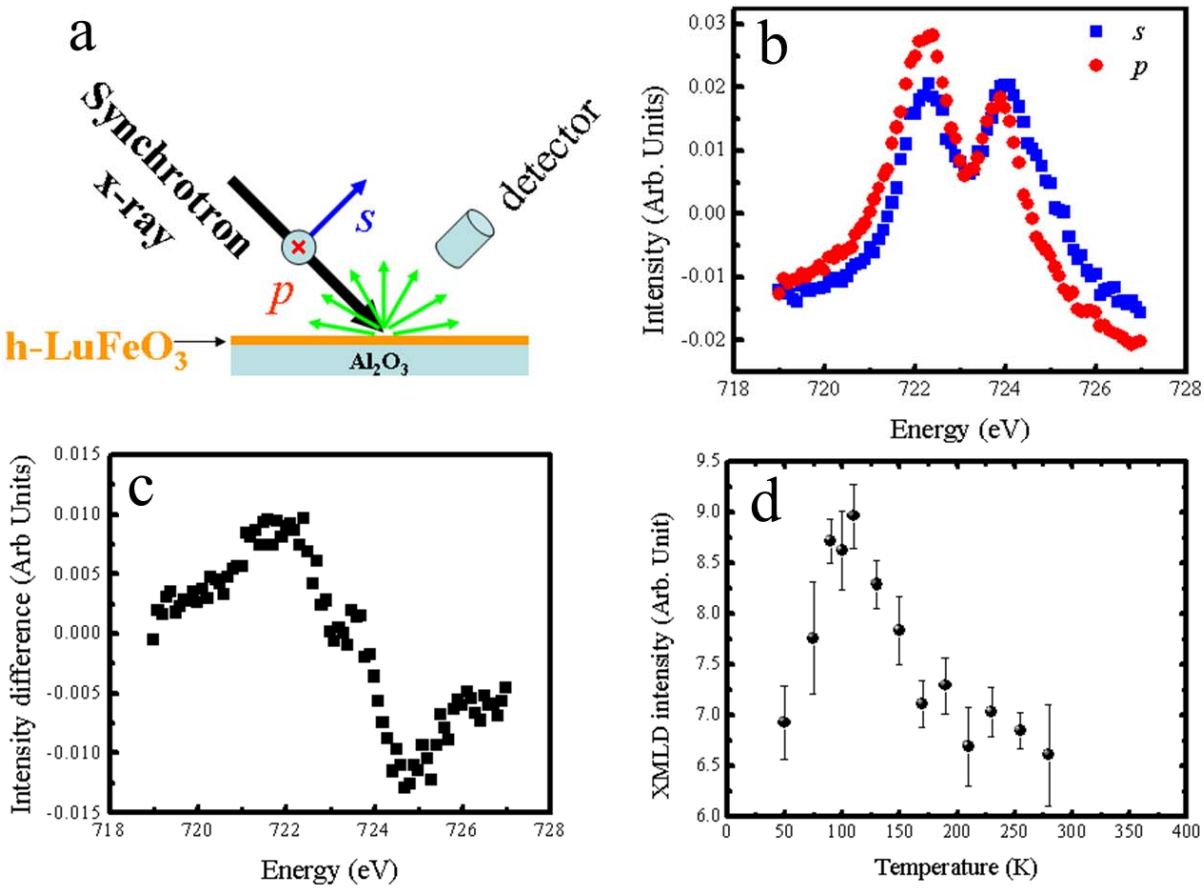

Figure 3.19 X-ray magnetic linear dichroism (XMLD) measurements. (a) Experimental setup for the XMLD measurements. (b) Profiles of the fluorescence intensity of the Fe-L_2 edge of for *s* and *p* polarized incident X-ray (after background subtraction) which shows significant anisotropy. (c) The difference between the two profiles in (b). (d) The XMLD contrast as a function of temperature at zero magnetic field.

We can derive the magnetic structure of h-$LuFeO_3$ films to a certain degree by taking both the neutron scattering data and the magnetization measurements into account. Since h-$LuFeO_3$ is similar in structure with $RMnO_3$ (R=Y, Sc, Ho-Lu) (space group $P6_3cm$) and their magnetic structures are characterized with same propagating vector K=0, we can try to analyze the magnetic structure of h-$LuFeO_3$ following the same practice of the symmetry analysis in $RMnO_3$.[89–92] Fig. 3.20 summarizes the possible magnetic structures with the propagating vector K=0 in a Hexagonal $LuFeO_3$. Here Γ_1, Γ_2, Γ_3 and Γ_4 are irreducible representations; and $\Gamma_5=\Gamma_1+\Gamma_2$, $\Gamma_6=\Gamma_3+\Gamma_4$. We notice that the ferromagnetic component along c-axis is only compatible with Γ_2 ($P6_3cm$ symmetry) and $\Gamma_1+\Gamma_2$ ($P6_3$ symmetry).[91] Because (1 0 0) magnetic peak is absent in Γ_2 and Γ_4,[93] it is evident that only $\Gamma_1+\Gamma_2$ can account for the data below T_{SR}. Since Γ_1 and Γ_3 will lead to substantial magnetic intensity near (1 0 0), they can be ruled out for the magnetic structures at temperatures $T_{SR}<T<T_N$, where (100) magnetic peak disappears. In addition, the presence of Γ_2 will generate ferromagnetic component along the c-axis, as it does for $T<T_{SR}$, since the corresponding spin interaction is not suppose to disappear at T_{SR}. Therefore, the only candidates is Γ_4 for the magnetic structures at temperatures $T_{SR}<T<T_N$.

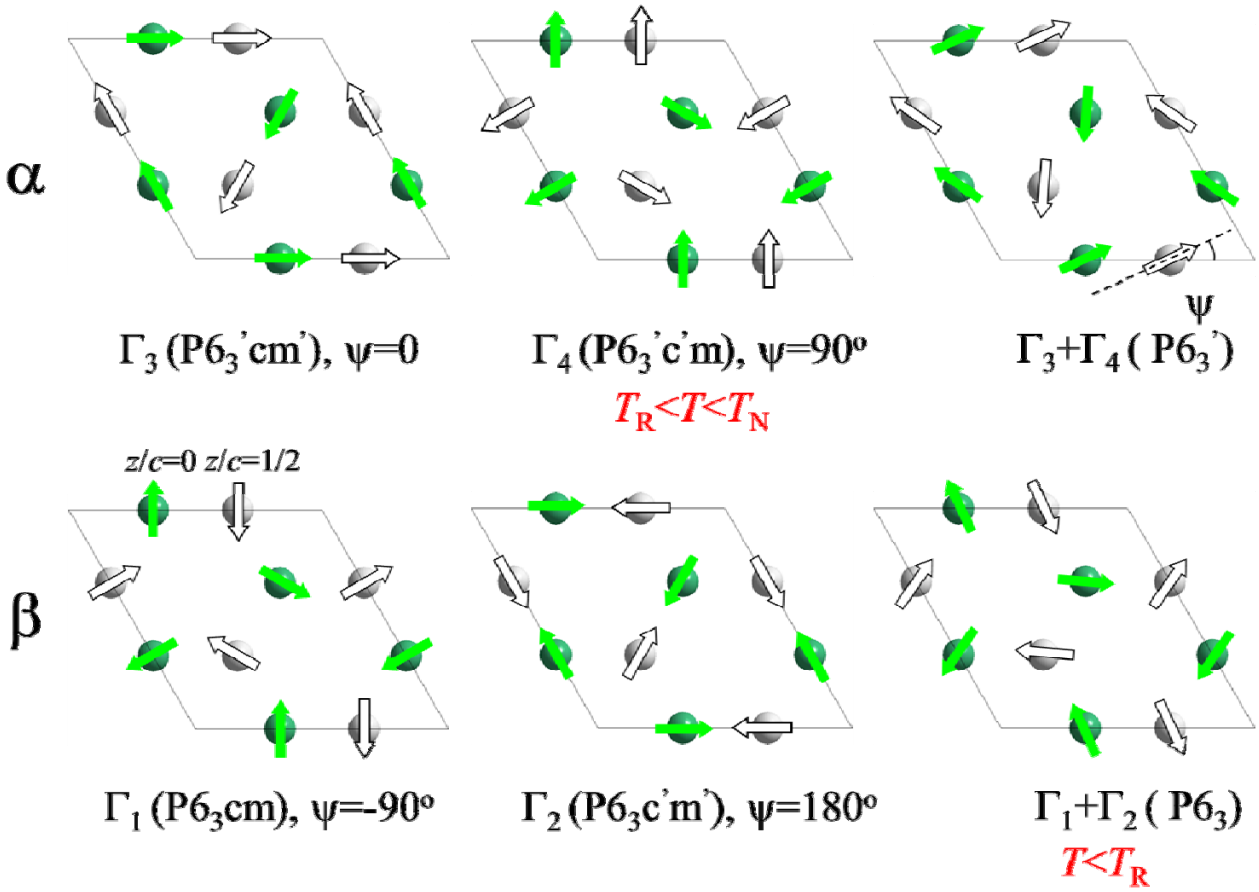

Figure 3.20 The possible magnetic structure of the Fe sites (irreproducible representations) in the $P6_3cm$ crystallographic symmetry and the assignments for h-$LuFeO_3$ according to the neutron scattering and magnetization measurements. The darker (lighter) balls represent Fe atoms at z/c=0 (z/c=0) and the arrows indicate the magnetic moment direction. Γ_1 (Γ_3) and Γ_2 (Γ_4) are related by the in-plane rotation angle ψ. The Γ_1 (Γ_2) and Γ_3 (Γ_4) are a homometric pair. $P6_3'$ ($P6_3$) is a superposition of Γ_3 and Γ_4 (Γ_1 and Γ_2). The magnetic structure of h-$LuFeO_3$ takes the form $P6_3$ at $T<T_R$ and Γ_4 at $T_R<T<T_N$.

We propose that the microscopic mechanism for the ferromagnetic moment is Dzialoshinskii-Moriya (DM)[94,95] interaction in which the effective Hamiltonian is $H_{DM} = -\sum_{i,j} \vec{D}_{ij} \bullet (\vec{S}_i \times \vec{S}_j)$, where $\vec{S}_i$ is the spin on site i, and $\vec{D}_{ij}$ is the interaction coefficient. Here the spin canting toward c-axis allows a slight reduction of the spin-spin angles from 120°,

gaining energy according to the DM interaction, while keeping the in-plane projections of spin-spin angles 120^{o}. Note that the DM interaction was first proposed to explain the weak ferromagnetism in α-Fe_2O_3, which disappears below approximately 260 K due to spin reorientation.[94–96] This DM interaction is also cited as the origin of weak ferromagnetism in orthoferrites and $ScMnO_3$. [62,91] The contributions from Fe and Mn to the net magnetic moments in those materials are all in the range of 0.01-0.1μ_B/formula unit. [62,91] We note this type of spin reorientation was also proposed previously to explain the magnetization of h-$RFeO_3$ (R: Lu, Er-Tb) films grown on (1 1 1) YSZ using metal organic chemical vapor deposition (MOCVD). [63,97]

What distinguishes our results from these previous reports is the clear observation of room-temperature antiferromagnetic order, which is difficult to detect using magnetization measurements alone, especially with the strong paramagnetic background from the YSZ substrate. [63,97] We also did the SQUID measurement of the temperature dependence of magnetization (*M*-*T*) of h-$LuFeO_3$ grown on yttrium stabilized zirconium oxide (YSZ) substrates at field-cool (FC) and zero-field-cool (ZFC) conditions (*H*=500Oe). Fig. 3.18 (b) shows the raw data whose paramagnetic background is so strong that the splitting between ZFC and FC data is not obvious. After subtracting the paramagnetic background assuming the Curie's law: $M=CH/T$, the ZFC and FC data split at around 130 K (Fig. 3.18(c)), consistent with that of sample grown on Al_2O_3. Clearly the background subtraction causes artificial drops of magnetization at $T<20$ K. Therefore, further quantitative analysis on this sample may not be reliable. (Note that the diamagnetic background from the substrate which is temperature independent is not subtracted here, which is why the magnetization is negative. The magnetization data of h-$LuFeO_3$ on Al_2O_3 substrates shown in the paper is without paramagnetic background subtraction because the paramagnetic signal from the substrates is minimal.) Interestingly, previously studied

orthoferrites show weak ferromagnetism all above 600 K, [98] but the magnetic ordering temperature of h-$RFeO_3$ is expected to be lower due to the frustration created by the triangular spin lattice.[98–102] On the other hand, the magnetic ordering temperature of the geometrically frustrate lattices also depend strongly on anisotropy.[101,102] Therefore, the future investigation on the interplay between exchange interaction, frustration and anisotropy of h-$RFeO_3$ will be very interesting.

3.7 Conclusions

The difficulty in finding single phase materials that exhibit both ferroelectric and magnetic order at room temperature has puzzled researchers because there are no physical principles prohibiting their existence. The observation of coexisting ferroelectricity and antiferromagnetism in single phase h-$LuFeO_3$ demonstrates another good example besides $BiFeO_3$. In addition, the high magnetic ordering temperature enables the application potential such as electric field control on magnetic phase that is unfortunately less practical in $RMnO_3$ due to the low T_N. Therefore, the combined room temperature ferroelectric and magnetic order make h-$LuFeO_3$ a material not only promising for technological applications but more importantly, extremely intriguing for fundamental research.

Chapter 4:

Surface Science Techniques

4.1 Pulsed Laser Deposition (PLD)[103]

PLD (Pulsed Laser Deposition) is an ideal technique for thin film deposition. The basic setup of our PLD system is shown in Figure (4.1). A high power pulsed laser beam is focused on a desired target in a UHV chamber. The ejected materials, which contain energetic electrons, ions, molecules and atoms, are directed onto a substrate facing the target. Those atoms are experienced very complex processes and deposited on the surface of the substrate and form a thin film. Once the laser ablation generates a large atomic flux corresponding to peak arrival rate of $10e^{18}$ to$10e^{19}$ atoms/cm^2s, these incoming atoms are deposited on the surface and become adatoms which diffuse on the substrate's surface. Some coalesce and become nuclei and some attach to the existing nuclei and contribute to the step advance. After a certain time t, if an adatom doesn't attach to the existing step, it will be re-evaporating out of the substrate's surface. A relatively longer time follows with small arrival rate after the pulse of high instantaneous atoms' arrival. During this time, the background gas contributes mostly to the new adatoms. The small nuclei forms in the previous step may become unstable and decay into adatoms. The laser-solid interaction and the process of the deposition are extremely complex. We will use a simple thermal dynamic model to describe this process in chapter 2.

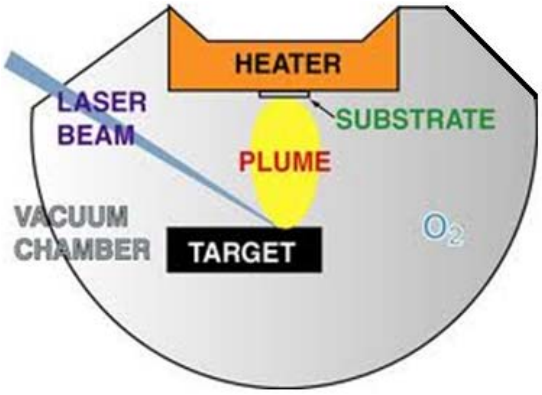

Figure 4.1 The basic setup of PLD system

4.2. Reflection High Energy Electron Diffraction (RHEED)

RHEED is a technique to characterize the surface of crystalline materials. The setup is shown in Figure (4.2): an electron gun generates a beam of electrons which strikes on the sample surface with a very small angle. The electrons diffracted from the sample surface will be collected by the detector. In my experiment, I used RHEED technique to characterize the crystallography of the sample and monitor the growth of the thin films. The incident electrons which have the wave vector k_i (which is the reciprocal of the wavelength of the incident electrons) will interact with the sample and the diffracted electrons with the wave vector k_f will constructively interfere at specific angles. Because the process is elastic scattering, so we have $|k_i|=|k_f|$. Take $|k_i|$ as the radius of the Ewald's sphere, k_f which corresponds to an allowed direction condition will also fall on the Ewald's sphere (Fig. 4.3). Based on these, we can calculate the epitaxial relation between the substrate and the film. We can also use RHEED to monitor the film's layer by layer growth and surface quality. RHEED is very sensitive to the sample's surface, with a glazing angle, only the first several layers of the atoms at the film surface contribute to the RHEED

pattern. So the intensity of individual spots on RHEED pattern can show single monolayer's growth process. Figure (4.4) shows the relation between the RHEED pattern intensity's periodic fluctuation and a single monolayer growth. Each full period represents formation of a single atomic layer. The prefect full filled layer corresponds to the highest RHEED intensity. The rougher of the surface, the less intense of the RHEED pattern we observe. The intensity is weakest on a half-filled layer. Once one layer growth is finished, the intensity recovers.

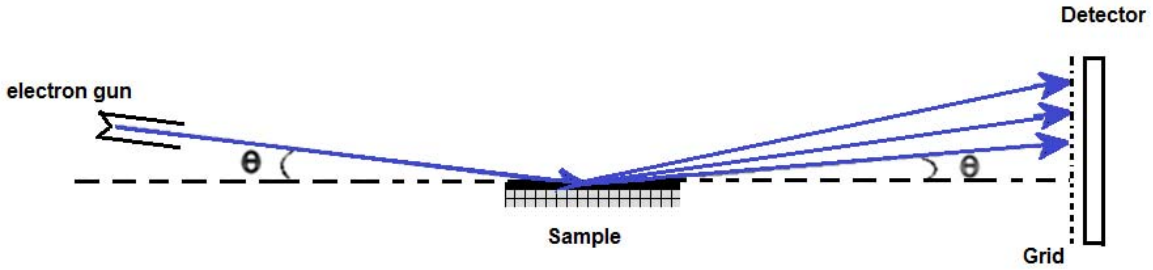

Figure 4.2 Basic setup of RHEED system

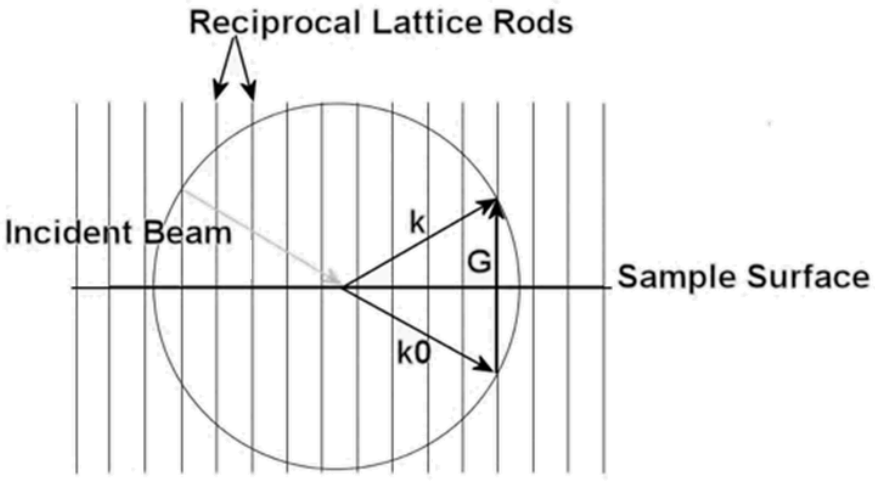

Figure 4.3 Ewald sphere show the interference relation in a diffraction experiment

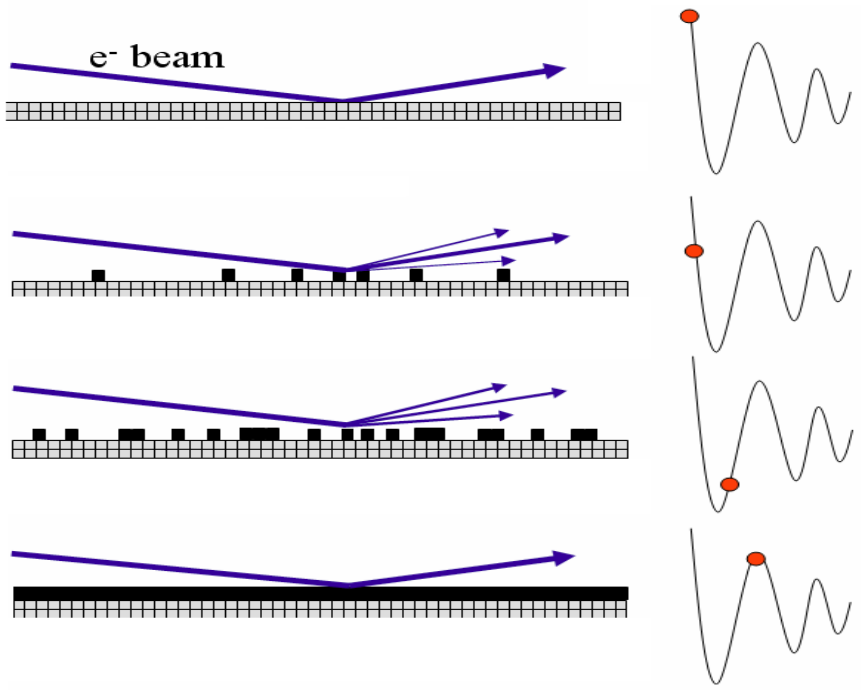

Figure 4.4 Relation between the RHEED pattern intensity's periodic fluctuation and a single monolayer growth

4.3 Low Energy Electron Diffraction (LEED)[104]

Similar to the RHEED, LEED is another tool we use to study the sample's surface structure. When monoenergetic electrons (10-200eV) are directed to the sample surface, electrons diffracted from the surface will be gathered on a phosphor screen which biased at a large positive potential on the order of several kilovolts. Only those scatted electrons which have the same energy as the incident electrons will passing through a repeller grid, accelerated and finally strike on the screen with a high energy. The crystal having long range order will show a diffraction pattern. From the diffraction pattern we will be able to determine the symmetry and size of the surface unit cell. Intensities of the diffraction spots provide the information of the amplitude of surface atom vibrations.

4.4 X-Ray Diffraction (XRD)

X-ray diffraction is an extremely useful tool for determining the crystallographic structure, chemical composition, and physical properties of thin films. When a monochromatic X-ray beam with wavelength λ is projected onto a crystalline material at an angle theta (Fig. 4.6), diffraction occurs only when the Bragg's law conditions are satisfied as shown is the Fig.4.5. Bragg's law is defined as $2d \sin(\theta) = n\lambda$ where d is the inter-planar distance, θ is the angle between the incident beam and the scattering plane, n is an order determined integer, and λ is the wavelength of the incident photon. By varying the angle theta, it will produce a pattern conclude all phases. There are several different kinds of XRD measurements to characterize the film sample. X-rays theta-2theta scan is used to probe crystalline planes in a film parallel to the substrate's surface. X-ray texture measurements is often plotted in polar coordinates, it measures at a fixed scattering angle with a series of φ, ω scan at different tilt ψ angles. We can also do the φ scan at both fixed scattering angle and tilt ψ angles on substrate and thin film to testify the epitaxial relationship between substrate and the film. All the real crystals will have some imperfection in it which is known as mosaic structure. So the whole film will broke up into some small blocks, those blocks are slightly disoriented one from another. Suppose the disorientation angle is Δ, then the diffraction peaks of a single crystal are not exactly at the angle of θ but at all angles between θ-Δ and θ+Δ. The Rocking curve measurement is a way to characterize the quality of the single crystal. The better quality film will have smaller number of the full width of half maximal (FWHM) of the rocking curve. The influence of those defects and mosaic are difficult to be observed and separated from other features from the single scans. Reciprocal space maps can be collected, which provides more information about the defects.

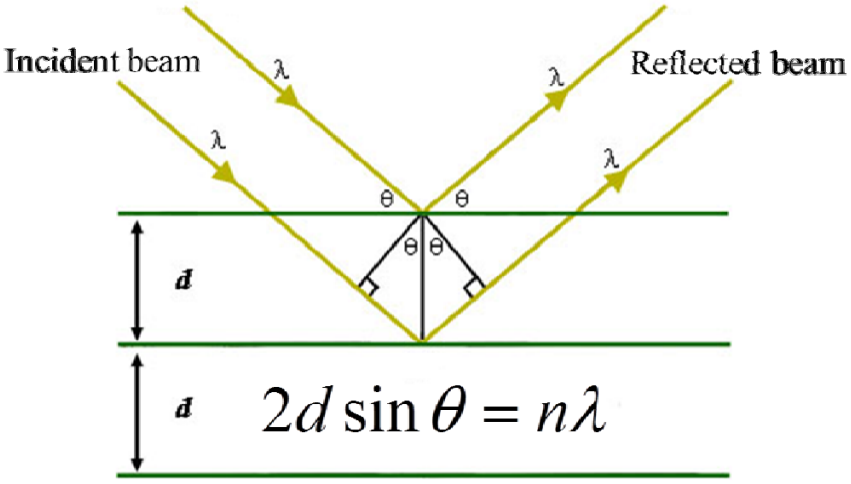

Figure 4.5 Bragg's law

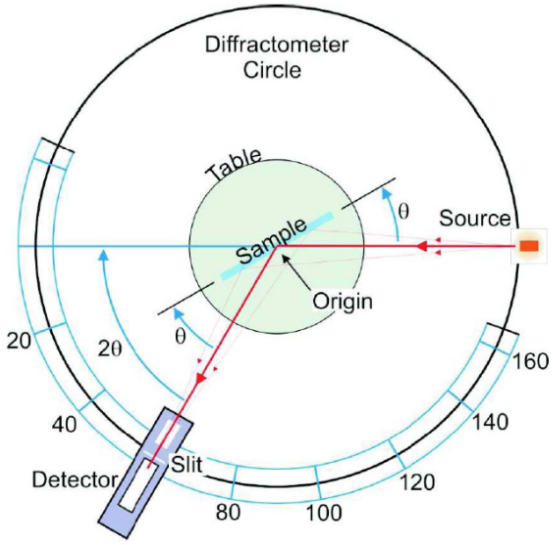

Figure 4.6 XRD basic set up

4.5 Transmission Electron Microscopy (TEM)

Transmission electron microscopy (TEM) is a vital tool to probe the atomic structure of crystal in which a focused electron beam is transmitted through an ultra-thin sample. The electrons go through the sample, interact with the sample and finally are projected onto a screen. This technique allows us to study the fine details of the structure of the sample. For example, orientation of the film, misfits, stacking faults and twinning in the sample.

4.6 Superconducting Quantum Interference Device (SQUID) Magnetometer

SQUID magnetometer is an extremely sensitive instrument used to measure extremely weak magnetic field, which makes it the ideal for studies thin film sample because of the small volume of thin film. The Quantum Design SQUID which consists of two superconductors separated by thin insulating layers to form two parallel Josephson junctions. Up to 7T magnetic fields can be applied in our SQUID with the temperature range from 4K to 400K, and has a sensitivity of 2*10e-8 emu. We also used the high temperature SQUID with an external furnace in the setup. The high T SQUID has a stable temperature range from room-T to 800 K.

4.7. Atomic Force Microscopy (AFM) and Piezo Force Microscopy (PFM)

The atomic force microscope is a high resolution type of scanning probe with a resolution on the scale of nanometers. Unlike the STM (scanning tunneling microscopy), which can only image

conducting and semiconducting surface, Atomic Force Microscopy can image almost all kinds of surface such as insulator, polymers and biological samples. A cantilever with a probe tip radius of curvature of several nanometers can be used to see the surface when brought into very close to a sample surface. The force between the tip and the sample is not measured directly, but calculated by measuring the deflection of the cantilever which is measured using a laser spot. The laser spot is reflected from the tip into an array of photodiodes. This force is calculated by treating the cantilever as a spring, obeys the Hooke's law F=-kz, where F is the force, k is the spring constant, z is the tip deflection, which is shown as the position change of a laser beam that reflects off the tip on the cantilever. Figure (4.7) shows the relation between the force and the probe distance from sample. AFM is very useful because the tip can interact with the surface through many different forces, such as Van der Waals force, magnetic force, chemical bonding force and electrostatic forces. Here, we mainly introduce two kinds of operation modes: contact mode and tapping mode. For the contact mode, we keep the force between the tip and the surface as a constant during the scanning by maintaining a constant deflection. This means the tip will keep a constant height above the surface and the overall force is repulsive. For the tapping mode, the cantilever is oscillated near its resonance frequency, and the tip is close to the sample surface with the amplitude around 100nm to 5um. During the scan, the oscillating tip moves toward the surface until it taps the surface. The cantilever intermittently contacts the surface. There is an electronic servo used to adjust the height between the cantilever and the sample to maintain constant oscillation amplitude. When the tip scans over a bump, the amplitude of oscillation decreases; when it passes over a depression, the oscillation amplitude increases. Once the amplitude changes, the electronic servo will give a feedback signal, and then adjust the tip height to maintain the constant amplitude.

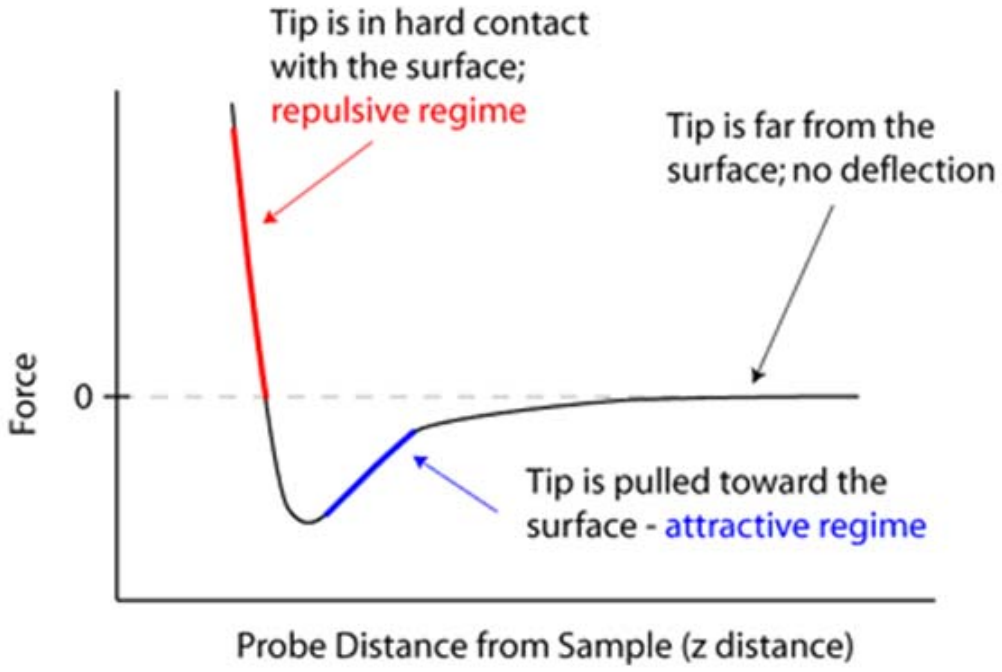

Figure 4.7 Relation between the force and the probe distance from sample

Piezoelectric force microscopy is a variant of Atomic force microscopy that can be used to study the piezoelectric response of materials under applied voltage. Since all ferroelectrics are also piezoelectric, we use PFM image and P-E loop to study the piezoelectric response of our samples. In our experiment setup, a conductive AFM tip is brought into contact with a ferroelectric surface or piezoelectric materials and an AC modulation is applied with an optional DC offset bias to the tip. This bias will establish an external electric field within the sample. Due to the inversed piezoelectric effect, an applied electric field can produce a mechanical strain and the sample surface will locally expand or contract. Figure (4.8) shows the schematic diagram of the PFM. Suppose we have out-of-plane electric polarization, when the applied electric field is

parallel to the electric polarization, the electrical domain would experience a vertical expansion; when the applied electric field is anti-parallel to the electric polarization, the electric domain would experience a vertical contraction. The domain size changes will directly result in a decrease or increase of the cantilever deflection. The AFM tapping mode is used to probe sample's mechanical response. The image shows contrast which corresponds to the vertical movement of the AFM tip.

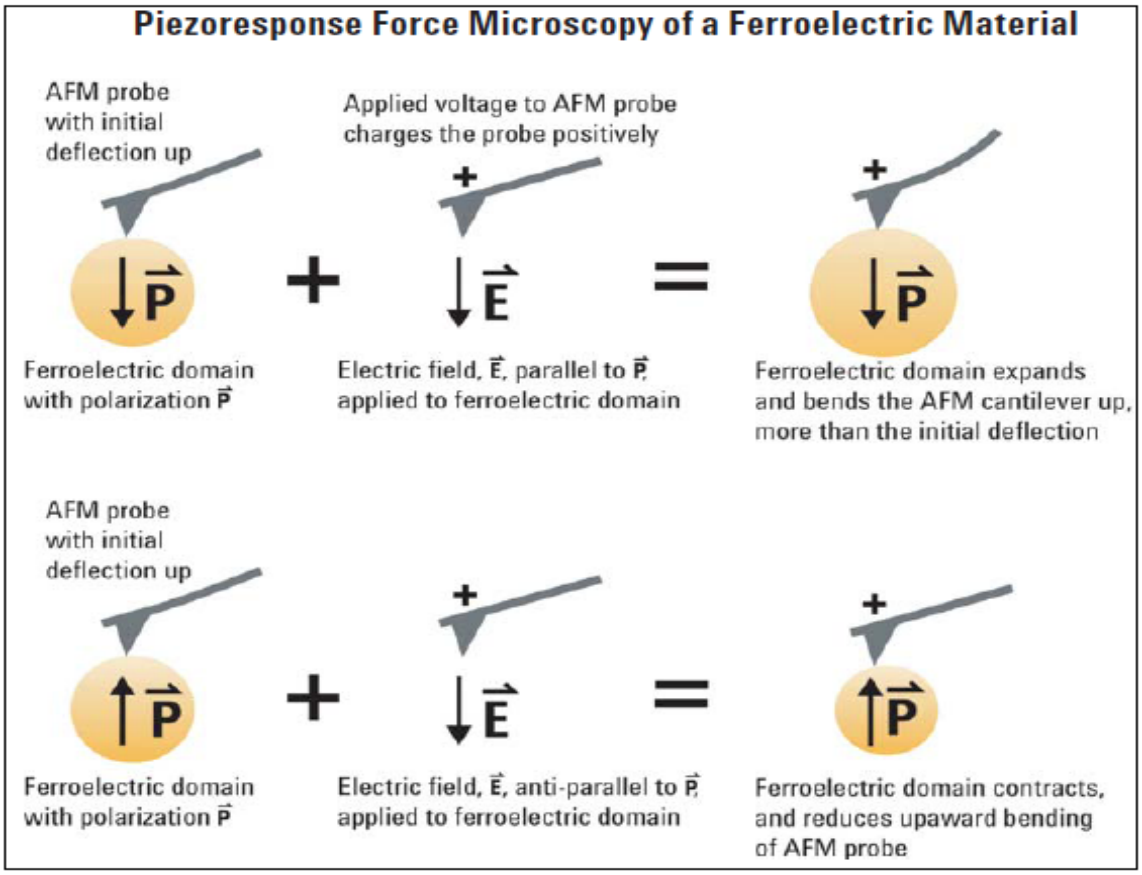

Figure 4.8 How to use the PFM to study the ferroelectric materials

4.8 X-Ray magnetic Circular Dichroism (XMCD) and X-Ray Magnetic Linear Dichroism (XMLD)[105]

I. XMCD

XMCD spectroscopy is usually used to study the materials which have ferromagnetic properties. During the measurement, either right or left circularly polarized photons will be provided, these two kinds of polarized photons have different absorption process between the spin-up or spin-down electrons, so it is spin dependent. The polarized photons transfer the angular momentum to the excited photoelectron, during this process; right circular photons transfer the opposite momentum as left circular photons. Since L3 and L2 edge have opposite spin orbital coupling, the polarization will be opposite at these two edges. As shown in the Figure 4.9.

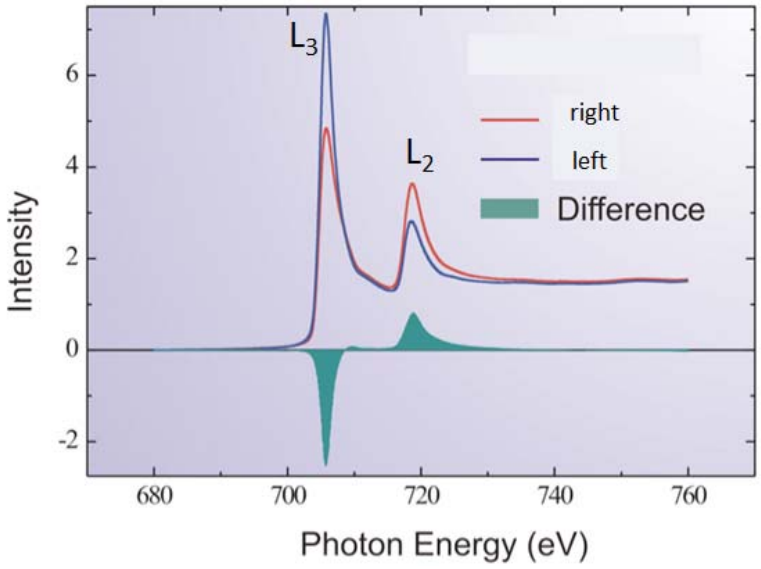

Figure 4.9 XMCD spectrum of Fe

II. XMLD

X-ray magnetic linear dichroism is to use the linearly polarized x-ray to study the magnetic properties. It can determine the orientation of the magnetic axis. The XMLD signal is proportional to the excitation strength of an electron from deeper level to the valence level by a photon. It measures directly the orbital information of the valence electrons while the spin information is also included due to the spin-orbital coupling. Therefore, it is sensitive to the orientation of the spin (e.g. in-plane or out-of-plane) but no to the sign (e.g. up or down). The orbital anisotropy of the detected atoms will lead to an asymmetry of the X-ray absorption signal. This effect is very easy to observe at the multiplet splitting, as shown in the Figure 4.10.

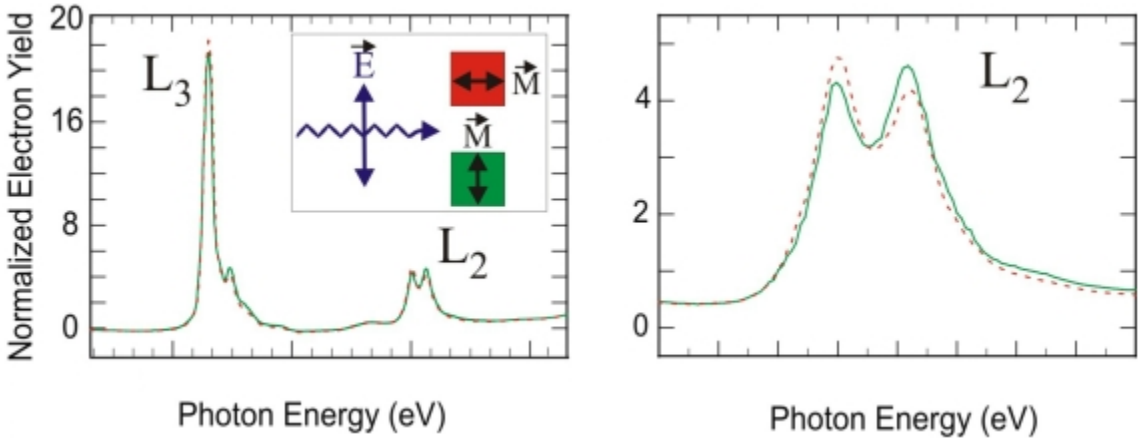

Figure 4.10 XMLD spectrum of Fe

4.9 Neutron scattering

Neutron scattering is a powerful tool to study the magnetic structure and spin excitations of condensed matter system because neutrons have magnetic moments which can interact with the magnetic field in the sample. In neutron scattering experiment, the sample will be put into the neutron beam and the scattered neutron intensity as a function of scattering angle and neutron energy will be detected. The scattering process is ruled by the laws of momentum and energy conservation:

$$\vec{Q} = \vec{k}_f - \vec{k}_i$$

$$\left|\vec{Q}\right| = k_f^2 + k_i^2 - 2k_i k_f \cos\theta_s$$

$$\hbar\omega = E_i - E_f = \frac{\hbar^2}{2m_n}(k_f^2 - k_i^2)$$

In a neutron diffraction (elastic scattering) experiment, the energy transfer is fixed at ($\hbar\omega$=0). The sample can be examined to obtain a diffraction pattern that provides information of the magnetic and nuclear structure of the material.

LIST OF REFERENCES

1. Curie, P. No Title. *J. Physique* **3**, 393 (1894).

2. *L. D. Landau and E. M. Lifshitz. Electrodynamics of continuous media. Pergamon Press, Oxford, New York, 1960.*

3. Fiebig, M. Revival of the magnetoelectric effect. *Journal of Physics D: Applied Physics* **38**, R123–R152 (2005).

4. Spaldin, N. A. & Fiebig, M. The Renaissance of Magnetoelectric Multiferroics. *Science* **871**, (2005).

5. Schmid, H. Introduction to the proceedings of the 2nd international conference on magnetoelectric interaction phenomena in crystals, MEIPIC-2. *Ferroelectrics* **161.**, 1—28 (1994).

6. Rivera, J.-P. On definition, units, measurements, tensor forms of the linear Cr-Cl, magnetoelectric effect and on a new dynamic method applied to boracite. *Ferroelectrics* **161**, 165—180 (1994).

7. Eerenstein, W., Mathur, N. D. & Scott, J. F. Multiferroic and magnetoelectric materials. *Nature* **442**, 759–65 (2006).

8. Lonkai, T. *et al.* Development of the high-temperature phase of hexagonal manganites. *Physical Review B* **69**, 134108 (2004).

9. Lee, S. *et al.* Giant magneto-elastic coupling in multiferroic hexagonal manganites. *Nature* **451**, 805–8 (2008).

10. Iida, H. *et al.* Ferroelectricity and Ferrimagnetism of Hexagonal YbFeO$_{3}$ Thin Films. *Journal of the Physical Society of Japan* **81**, 024719 (2012).

11. van den Brink, J. & Khomskii, D. I. Multiferroicity due to charge ordering. *Journal of Physics: Condensed Matter* **20**, 434217 (2008).

12. N. Ikeda, H. Ohsumi, K. Ohwada, K. Ishii, T. Inami, K. Kakurai, Y. Murakami, K. Yoshii, S. Mori, Y. Horibe, and H. K. No Title. *Nature* **436**, 1136 (2005).

13. M. A. Subramanian, T. He, J. Z. Chen, N. S. Rogado, T. G. Calvarese, and A. W. S. No Title. *Advanced Materials* **18**, 1737 (2006).

14. Subramanian, M. A. *et al.* Giant Room–Temperature Magnetodielectric Response in the Electronic Ferroelectric LuFe2O4. *Advanced Materials* **18**, 1737–1739 (2006).

15. Kenzelmann, M. *et al.* Magnetic Inversion Symmetry Breaking and Ferroelectricity in TbMnO3. *Physical Review Letters* **95**, 087206 (2005).

16. Mostovoy, M. Ferroelectricity in Spiral Magnets. *Physical Review Letters* **96**, 067601 (2006).

17. Kimura, T. *et al.* Magnetic control of ferroelectric polarization. *Nature* **426**, 55–8 (2003).

18. Choi, Y. *et al.* Ferroelectricity in an Ising Chain Magnet. *Physical Review Letters* **100**, 047601 (2008).

19. J Li, J Wang, M Wuttig, R Ramesh, N Wang, B. R. & A P Pyatakov, A K Zvezdin, D. V. No Title. *Appl. Phys. Lett.* **84**, 5261 (2004).

20. M S Kartavtseva, O Yu Gorbenko, A R Kaul, T. V. M. & S A Savinov, O. A. A. No Title. *J. Mater. Res.* **22)**, 2063 (2007).

21. Neaton, J. B., Ederer, C., Waghmare, U. V., Spaldin, N. A. & Rabe, K. M. First-principles study of spontaneous polarization in multiferroic BiFeO3. .*Phys. Rev. B* **71**, 014113 (2005).

22. Ederer, C. & Spaldin, N. A. Weak ferromagnetism and magnetoelectric coupling in bismuth ferrite. *Phys. Rev. B* **71**, 060401 (2005).

23. J Wang, JB Neaton, H Zheng, V. N. Epitaxial BiFeO3 multiferroic thin fi lm heterostructures. *Science* **299**, 1719 (2003).

24. Vijaya Kumar, M. S., Nagashio, K., Hibiya, T. & Kuribayashi, K. Formation of Hexagonal Metastable Phases from an Undercooled LuFeO 3 Melt in an Atmosphere with Low Oxygen Partial Pressure. *Journal of the American Ceramic Society* **91**, 806–812 (2008).

25. Wang, J. *et al.* Epitaxial BiFeO3 Multiferroic Thin Film Heterostructures . *Science* **299** , 1719–1722 (2003).

26. Hur, N. *et al.* Electric polarization reversal and memory in a multiferroic material induced by magnetic fields. *Nature* **429**, 392–395 (2004).

27. Ikeda, N. *et al.* Ferroelectricity from iron valence ordering in the charge-frustrated system LuFe2O4. *Nature* **436**, 1136–1138 (2005).

28. Xu, X. *et al.* High Tunability of the Surface-Enhanced Raman Scattering Response with a Metal−Multiferroic Composite. *Nano Letters* **11**, 1265–1269 (2011).

29. Liu, J., Wang, Y. & Dai, J. Y. Structural and dielectric properties of LuFe2O4 thin films grown by pulsed-laser deposition. *Thin Solid Films* **518**, 6909–6914 (2010).

30. Jason Rejman, Tara Dhakal, Pritish Mukherjee, H. S. and S. W. Pulsed Laser Deposition as a Novel Growth Technique of Multiferroic LuFe2O4 Thin Films. *MRS Proceedings* **1199**, F03–22 (2009).

31. M.S. Vijaya Kumar, K. K. and K. K. Formation of LuFe2O4 phase from an undercooled LuFeO3 melt in reduced oxygen partial pressure. *Journal of Materials Research* **23**, 2996 (2008).

32. Sekine, T. & Katsura, T. Phase equilibria in the system Fe□Fe2O3□Lu2O3 at 1200°C. *Journal of Solid State Chemistry* **17**, 49–54 (1976).

33. Katsura, T., Sekine, T., Kitayama, K., Sugihara, T. & Kimizuka, N. Thermodynamic properties of Fe-lathanoid-O compounds at high temperatures. *Journal of Solid State Chemistry* **23**, 43–57 (1978).

34. Kimizuka, N., Yamamoto, A., Ohashi, H., Sugihara, T. & Sekine, T. The stability of the phases in the Ln2O3□FeO□Fe2O3 systems which are stable at elevated temperatures (Ln: Lanthanide elements and Y). *Journal of Solid State Chemistry* **49**, 65–76 (1983).

35. The peak at 30.27 degree in Fig. 2.2(c) is assigned as h(004) based on its proximity to the calculated peak position of h(004) (30.52 degree) and the fact that TEM results are consistent with coexistence of h-LuFeO3 and LuFe2O4.

36. *The population of the LuFeO3 can be reduced by lowering the O2 pressure, which however increases the amount of Fe3O4.*

37. Hazen, R. M. Effects of temperature and pressure on the cell dimension and X-ray temperature factors of periclase. *American Mineralogist* **61**, 266–271 (1976).

38. Isobe, M., Kimizuka, N., Iida, J. & Takekawa, S. STRUCTURES OF LUFECOO4 AND LUFE2O4. *ACTA CRYSTALLOGRAPHICA SECTION C-CRYSTAL STRUCTURE COMMUNICATIONS* **46**, 1917–1918 (1990).

39. Magome, E., Moriyoshi, C., Kuroiwa, Y., Masuno, A. & Inoue, H. Noncentrosymmetric Structure of LuFeO(3) in Metastable State. *Japanese Journal of Applied Physics* **49**, 09ME06 (2010).

40. Maezio, M., Remeika, J. P. & Dernier, P. D. CRYSTAL CHEMISTRY OF RARE EARTH ORTHOFERRITES. *ACTA CRYSTALLOGRAPHICA SECTION B-STRUCTURAL CRYSTALLOGRAPHY AND CRYSTAL CHEMISTRY* **B 26**, 2008–& (1970).

41. Wechsler, B. A., Lindsley, D. H. & Prewitt, C. T. CRYSTAL-STRUCTURE AND CATION DISTRIBUTION IN TITANOMAGNETITES (FE3-XTIXO4). *AMERICAN MINERALOGIST* **69**, 754–770 (1984).

42. Marsella, L. & Fiorentini, V. Structure and stability of rare-earth and transition-metal oxides. *PHYSICAL REVIEW B* **69**, 172103 (2004).

43. At 12 K, the remanence is 7.5 emu cm-3 and the coercive field is approximately 300 Oe. This can be attributed to the existence of a trace amount of Fe_3O_4 islands because their temperature dependences are very similar to those of the samples with larger Fe.

44. Iida, Junji; Nakagawa, Yasuaki; Takekawa, Shunji; Kimizuka, N. High Field Magnetization of Single Crystal LuFe2O4. *Journal of the Physical Society of Japan* **56**, 3746 (1987).

45. Bean, C. P. & Livingston, J. D. Superparamagnetism. *Journal of Applied Physics* **30**, S120–S129 (1959).

46. Xu, X., Yin, S., Moro, R. & de Heer, W. A. Distribution of magnetization of a cold ferromagnetic cluster beam. *PHYSICAL REVIEW B* **78**, 054430 (2008).

47. Here the field should be high enough to saturate the impurity moment but low enough to have linear relation between magnetization and magnetic field.

48. Markov, I. V. *Crystal growth for beginners : fundamentals of nucleation, crystal growth, and epitaxy*. (1995).

49. Katsura, T., Sekine, T., Kitayama, K., Sugihara, T. & Kimizuka, N. THERMODYNAMIC PROPERTIES OF FE-LANTHANOID-O COMPOUNDS AT HIGH-TEMPERATURES. *Journal of Solid State Chemistry* **23**, 43–57 (1978).

50. Greedon, J. E. *Magnetic oxides*. (John Wiley & Sons: New York, 1994).

51. Wu, W. *et al.* Formation of Pancakelike Ising Domains and Giant Magnetic Coercivity in Ferrimagnetic LuFe_{2}O_{4}. *Physical Review Letters* **101**, 137203 (2008).

52. Ko, K.-T. *et al.* Electronic Origin of Giant Magnetic Anisotropy in Multiferroic LuFe_{2}O_{4}. *Physical Review Letters* **103**, 207202 (2009).

53. Wang, F., Kim, J., Kim, Y.-J. & Gu, G. D. Spin-glass behavior in LuFe_{2}O_{4+δ}. *Physical Review B* **80**, 24419 (2009).

54. Phan, M. H. *et al.* Magnetism and cluster glass dynamics in geometrically frustrated LuFe[sub 2]O[sub 4]. *Journal of Applied Physics* **105**, 07E308–3 (2009).

55. Park, S. *et al.* Pancakelike Ising domains and charge-ordered superlattice domains in LuFe_{2}O_{4}. *Physical Review B* **79**, 180401 (2009).

56. Li, Y. B. Q. and H. X. Y. and Y. Z. and H. F. T. and C. M. and Y. G. Z. and R. I. W. and J. Q. The effect of Mg doping on the structural and physical properties of LuFe 2 O 4 and Lu 2 Fe 3 O 7. *Journal of Physics: Condensed Matter* **21**, 15401 (2009).

57. Yang, H. *et al.* Electronic ferroelectricity, charge ordering and structural phase transitions in LuFe2O4(LuFeO3)n (n = 0 and 1). *physica status solidi (b)* **247**, 870–876 (2010).

58. Akbashev, A. R., Semisalova, A. S., Perov, N. S. & Kaul, A. R. Weak ferromagnetism in hexagonal orthoferrites RFeO[sub 3] (R = Lu, Er-Tb). *Applied Physics Letters* **99**, 122502–122503 (2011).

59. Khomskii, D. Classifying multiferroics: Mechanisms and effects. *Physics* **2**, (2009).

60. The Mendeley Support Team Getting Started with Mendeley. *Mendeley Desktop* 1–16 (2011).at <http://www.mendeley.com>

61. Thomas, R., Scott, J. F., Bose, D. N. & Katiyar, R. S. Multiferroic thin-film integration onto semiconductor devices. *Journal of Physics-Condensed Matter* **22**, 423201 (2010).

62. Treves, D. Studies on Orthoferrites at the Weizmann Institute of Science. *Journal of Applied Physics* **36**, 1033–1039 (1965).

63. Bossak, A. A. *et al.* XRD and HREM studies of epitaxially stabilized hexagonal orthoferrites RFeO3 (R = Eu-Lu). *Chemistry of Materials* **16**, 1751–1755 (2004).

64. Van Aken, B. B., Palstra, T. T. M., Filippetti, A. & Spaldin, N. A. The origin of ferroelectricity in magnetoelectric YMnO3. *Nat Mater* **3**, 164–170 (2004).

65. Fennie, C. J. & Rabe, K. M. Ferroelectric transition in YMnO_{3} from first principles. *Physical Review B* **72**, 100103 (2005).

66. Uesu, Y. *et al.* Multi-ferroicity of thin-film-stabilized hexagonal YbFeO3. *2010 IEEE International Symposium on the Applications of Ferroelectrics (ISAF),* 1 (2010).doi:10.1109/ISAF.2010.5712256

67. Iida, H., Koizumi, T. & Uesu, Y. Physical properties of new multiferroic hexagonal YbFeO3 thin film. *Phase Transitions* **84**, 747–752 (2011).

68. Xu, X. S. *et al.* Optical properties and magnetochromism in multiferroic BiFeO_{3}. *Physical Review B* **79**, 134425 (2009).

69. J. Stohr, H. C. & S. *Magnetism from fundamentals to nanoscale dynamics*. (Springer: Berlin, 2006).

70. van der Laan, G., Zaanen, J., Sawatzky, G. A., Karnatak, R. & Esteva, J.-M. Comparison of x-ray absorption with x-ray photoemission of nickel dihalides and NiO. *Physical Review B* **33**, 4253–4263 (1986).

71. Wadati, H. *et al.* Hole-doping-induced changes in the electronic structure of La_{1−x}Sr_{x}FeO_{3}: Soft x-ray photoemission and absorption study of epitaxial thin films. *Physical Review B* **71**, 35108 (2005).

72. Cotton, F. A. *Chemical applications of group theory*. (Wiley: New York, 1990).

73. Cho, D.-Y. *et al.* Ferroelectricity Driven by Y d^{0}-ness with Rehybridization in YMnO_{3}. *Physical Review Letters* **98**, 217601 (2007).

74. Pavlov, V. V. *et al.* Optical properties and electronic structure of multiferroic hexagonal orthoferrites RFeO[sub 3] (R = Ho, Er, Lu). *Journal of Applied Physics* **111**, 56103–56105 (2012).

75. Kresse, G. & Furthmüller, J. Efficient iterative schemes for ab initio total-energy calculations using a plane-wave basis set. *Physical Review B* **54**, 11169–11186 (1996).

76. A 500 eV planewave cutoff and 6×6×3 k points mesh are used.

77. Perdew, J. P. *et al.* Restoring the Density-Gradient Expansion for Exchange in Solids and Surfaces. *Physical Review Letters* **100**, 136406 (2008).

78. Marzari, N. & Vanderbilt, D. Maximally localized generalized Wannier functions for composite energy bands. *Physical Review B* **56**, 12847–12865 (1997).

79. Onida, G., Reining, L. & Rubio, A. Electronic excitations: density-functional versus many-body Green's-function approaches. *Reviews of Modern Physics* **74**, 601–659 (2002).

80. Chen, W., Wu, X. & Car, R. X-Ray Absorption Signatures of the Molecular Environment in Water and Ice. *Physical Review Letters* **105**, 17802 (2010).

81. Xiang, H. J. & Whangbo, M.-H. Charge Order and the Origin of Giant Magnetocapacitance in LuFe_{2}O_{4}. *Physical Review Letters* **98**, 246403 (2007).

82. Blaha, P. *An Augmented Plane Wave + Local Orbitals Program for Calculating Crystal Properties*. (Tech. Universitat Wien: Austria, 2001).

83. The energy threshold separating the localized and nonlocalized electronic states is chosen to be -7Ry. The muffintin radii are 2.35 Bohr for Lu, 1.98 Bohr for Fe, and 1.65 Bohr for O. The criterion for the number of plane waves is chosen to be Rmin MT*Kma.

84. Lines, M. E. & Glass, A. M. *Principles and applications of ferroelectrics and related materials*. (Clarendon Press: Oxford [Eng.], 1977).

85. Jesse, S., Maksymovych, P. & Kalinin, S. V. Rapid multidimensional data acquisition in scanning probe microscopy applied to local polarization dynamics and voltage dependent contact mechanics. *Applied Physics Letters* **93**, 112903 (2008).

86. Muñoz, A. *et al.* Magnetic structure of hexagonal RMnO_{3} (R=Y, Sc): Thermal evolution from neutron powder diffraction data. *Physical Review B* **62**, 9498–9510 (2000).

87. Chatterji, T., Ghosh, S., Singh, A., Regnault, L. P. & Rheinstädter, M. Spin dynamics of YMnO_{3} studied via inelastic neutron scattering and the anisotropic Hubbard model. *Physical Review B* **76**, 144406 (2007).

88. Roessli, B., Gvasaliya, S. N., Pomjakushina, E. & Conder, K. Spin Fluctuations in the Stacked-Triangular Antiferromagnet YMnO3. *JETP Letters* **81**, 287–291 (2005).

89. Bertaut, E. F. & Mercier, M. Structure magnetique de MnYO3. *Physics Letters* **5**, 27–29 (1963).

90. Bertaut, E. F. Representation analysis of magnetic structures. *Acta Crystallographica Section A-Crystal Physics Diffraction Theoretical and General Crystallography* **A 24**, 217–& (1968).

91. Munoz, A. *et al.* Magnetic structure of hexagonal RMnO_{3} (R=Y, Sc): Thermal evolution from neutron powder diffraction data. *Physical Review B* **62**, 9498–9510 (2000).

92. Brown, P. J. & T Chatterji Neutron diffraction and polarimetric study of the magnetic and crystal structures of HoMnO 3 and YMnO 3. *Journal of Physics: Condensed Matter* **18**, 10085 (2006).

93. Helton, J. S., Singh, D. K., Nair, H. S. & Elizabeth, S. Magnetic order of the hexagonal rare-earth manganite Dy_{0.5}Y_{0.5}MnO_{3}. *Physical Review B* **84**, 64434 (2011).

94. Dzyaloshinsky, I. A Thermodynamic Theory of Weak Ferromagnetism of Antiferromagnetics. *Journal of Physics and chemistry of solids* **4**, 241–255 (1958).

95. Moriya, T. Anisotropic superexchange interaction and weak ferromagnetism. *Physical Review* **120**, 91–98 (1960).

96. Morin, F. J. Magnetic Susceptibility of αFe_{2}O_{3} and αFe_{2}O_{3} with Added Titanium. *Physical Review* **78**, 819–820 (1950).

97. Akbashev, A. R. Weak ferromagnetism in hexagonal orthoferrites RFeO3 (R=Lu, Er-Tb). *Appl. Phys. Lett.* **99**, 122502 (2011).

98. Cheremisinoff, N. P. *Handbook of ceramics and composites*. (M. Dekker: New York, 1990).

99. Klimin, S. A. *et al.* Structural phase transition in the two-dimensional triangular lattice antiferromagnet RbFe(MoO_{4})_{2}. *Physical Review B* **68**, 174408 (2003).

100. Mitsuda, S., Mase, M., Uno, T., Kitazawa, H. & Katori, H. H-T Magnetic Phase Diagram of a Frustrated Triangular Lattice Antiferromagnet CuFeO(2). *Journal of the Physical Society of Japan* **69**, 33 LP – 36

101. Plumer, S. G. C. and M. L. A model of magnetic order in hexagonal HoMnO 3. *Journal of Physics: Condensed Matter* **22**, 162201 (2010).

102. Ramirez, A. P. Strongly Geometrically Frustrated Magnets. *Annual Review of Materials Science* **24**, 453–480 (1994).

103. Chrisey, Douglas B. ; Hubler, C. K. *Paused laser deposition of thin film*.

104. Hove, M.A.Van; Weinberg, W.H.; Chan, C. M. *Low energy electron diffraction*. (1986).

105. Magnetic Dichroism Spectroscopy and Microscopy. http://www–ssrl.slac.stanford.edu/stohr/xmcd.htm

VITA

Wenbin Wang was born on July 6, 1983 in Lanzhou, Gansu Province, China. She graduated from the High School Attached to Northwest Normal University. She received a Bachelor of Science degree in Physics from Lanzhou University in July, 2006. After that, she spent two more years as a graduate student at Physics department of Lanzhou University. In 2008, she came to U.S. and attended the graduate program in physics at the University of Tennessee. One year later, she joined the Thin Films and Nanostructures group at Oak Ridge National Lab. She expects to receive her Doctorate of Philosophy degree in physics in December of 2012.